University of Pécs

Excitations of Quasi-Two-Dimensional Electron Systems in Magnetic Field

Judit Sári

PhD Thesis

Supervisor

Csaba Tőke

Institute of Physics

2015

Contents

1 Introduction **1**

1.1 Overview 1

1.2 Outline of Thesis 3

2 Quasi-Two-Dimensional Material Systems **5**

2.1 Landau Level Spectrum of Conventional Two-Dimensional Electron Gas 6

2.2 Monolayer Graphene 7

2.2.1 Graphene as a Single-Layer of Graphite - Preparation Methods . 7

2.2.2 Elementary Properties in Zero Magnetic Field 8

2.2.3 Graphene in a Perpendicular Magnetic Field 11

2.2.4 Relativistic Properties of Massless Fermions in Graphene 13

2.3 Bilayer Graphene 17

2.4 Organic Quasi-Two-Dimensional Materials - the α-(BEDT-TTF)$_2$I$_3$ . . 25

2.4.1 Material Properties and Zero-Gap State in α-(BEDT-TTF)$_2$I$_3$. 25

2.4.2 Tight-Binding Description of the Conical Bands 27

2.4.3 Relativistic Covariance in α-(BEDT-TTF)$_2$I$_3$ 30

2.4.4 Massless Fermions in Related Zero-Gap Organic Compounds . . 32

3 Magneto-Optical Properties within the Single-Particle Picture **34**

3.1 Introduction 34

3.2 Derivation of the Dimensionless Absorption Coefficient 35

3.3 Results and Discussion 38

3.3.1 The Dimensionless Matrix Element 38

3.3.2 The Absorption Coefficient 42

3.4 Concluding Remarks and Future Perspectives 46

4 Magnetoplasmons - Density Oscillations in a Magnetic Field 49

4.1 Introduction 49

4.1.1 General Formalism of the Density-Density Response Function . 49

4.1.2 Magnetoplasmons in Two-Dimensional Systems 51

4.2 Magnetoplasmons in α-(BEDT-TTF)$_2$I$_3$: the Continuum Model 56

4.2.1 The Particle-Hole Excitation Spectrum at $B = 0$T Field 56

4.2.2 Approximations and Methods 59

4.2.3 Interaction Strength 64

4.3 Results and Discussion 65

4.3.1 Response of the Massless Carriers 66

4.3.2 Response within the Three-Valley Model 73

4.3.3 Static Screening 77

4.4 Conclusion 78

5 Magnetoexcitons - Bound Particle-Hole Pairs in a Magnetic Field 80

5.1 Introduction 80

5.2 The Central Landau Band in Bilayer Graphene 82

5.3 Kohn's Theorem and Interaction Strength 84

5.4 Magnetoexcitons 87

5.5 Results and Discussion 91

5.5.1 Integer Quantum Hall States 91

5.5.2 Quantum Hall Ferromagnetic States 95

5.6 Conclusion 105

New Scientific Results 108

List of publications 110

Összefoglalás 111

Bevezetés 111

Áttekintés, az értekezés felépítése 112

Tézispontok 113

List of Symbols, Abbreviations and Conventions **116**

Acknowledgements **118**

A Monolayer Graphene in a Perpendicular Magnetic Field **120**

B Eigenfunctions of α-(BEDT-TTF)$_2$I$_3$ **123**

C Dimensionless Matrix Elements **125**

D Derivation of the Bare Polarization Function for Massive Carriers **127**

D.1 Derivation of the Time-Ordered Green's Function 127

D.2 Bare Polarization Function for the Two-Dimensional Electron Gas . . . 129

E The Computation of Form Factors **133**

E.1 Form Factor for Conventional Two-Dimensional Electron Gas 133

E.2 Form Factor for the Weyl System 134

Bibliography **137**

Chapter 1

Introduction

1.1 Overview

Though quasi-two-dimensional systems had always been in the core of scientific interest, the first isolation of graphene, a two-dimensional carbon allotrope, in 2005 (see Refs. [122] and [183]) gave new impetus to the research of two-dimensional (2D) materials.[1] The peculiarity of graphene is rooted in its 2D nature, and manifests itself in extraordinary properties such as the conical band structure at low energies, or the anomalous quantum Hall effect (QHE). The conical valleys, commonly referred to as Dirac cones, are described by the Dirac equation of massless particles, albeit with a much lower velocity v_F instead of the speed of light c. This makes graphene the first 2D condensed matter system that hosts massless, charged fermions. The versatile material properties of graphene open the possibility for applications ranging from chemical sensors to transistors, see Ref. [50].

The boost in graphene's research is primarily engined by the fascination that the truly 2D nature of the material envoked, leading to the isolation and investigation of a plethora of other 2D materials as a direct consequence. A notable class is the transition metal dichalcogenides, which are layered crystals offering themselves to exfoliation techniques. Prominant examples include MoS_2, $MoSe_2$, WS_2 or WSe_2, for details see

[1] Several reviews demonstrate the tremendous research interest in graphene: Castro Neto *et al.* in [27] review the electronic properties of monolayer and bilayer graphene, Kotov *et al.* in [86] focus on electron-electron interaction in graphene, Goerbig in [54] reviews the properties in magnetic field, Peres in [131] and Das Sarma *et al.* in [35] deal with transport phenomena, while in their recent review [11] Basov *et al.* concentrate on graphene spectroscopy.

Ref. [85] or the review article [171]. Another noteworthy material besides the transition metal dichalcogenides is the hexagonal boron-nitride (hBN), few layer samples are readily made by chemical vapour deposition, see Ref. [165]. Likewise, some metallic 2D structures have also been recently fabricated, e.g. single-layer rhodium, see Ref. [38], or ultrathin palladium nanosheets, see [177]. We also mention germanene, silicon carbide, silicene, the latter being the focus of Ref. [138]. In their comprehensive review [106], Miró *et al.* present a panoramic view of the properties of currently investigated 2D materials. Looking at the above list, it is clear that in spite of their common 2D nature these materials vary considerably as far as their electrical properties or band structure are concerned. Some of them host Dirac electrons, others are usual semiconductors or insulators, see Ref. [170]. Undeniably, such a versatility may lead to the discovery of novel physical phenomena and open the possibility of several cutting-edge applications.

Besides, the interest in graphene is also inspired by the presence of Dirac electrons, which induced a quest for other Dirac systems. A prominent class of three-dimensional (3D) materials that host Dirac electrons on their surface states is topological insulators, which have naturally become the focus of intense research in the last decade, see review article [61]. In addition, in some layered organic compounds, including α-(BEDT-TTF)$_2$I$_3$, the low-energy band structure is described by conical valleys. These 3D crystals have strong 2D nature and massless fermions usually appear under high pressure or strain, see Refs. [118], [160] and [161], and also discussion in Sec. 2.4.4.

However impressive the above list of 2D materials or 3D crystals with Dirac cones may be, we should notice that the research of these materials is still intense with several open questions to be answered. Undoubtedly, graphene is the best known among them, though our understanding is not complete in this case either, see the list of debated or open questions in [86]. The same is particularly true for the other materials. In some cases even basic material properties, such as the low-energy band structure of α-(BEDT-TTF)$_2$I$_3$, is a debated issue, see [3], [111]. For these reasons we believe that the theoretical investigation of the elementary properties and many-body effects of these quasi-2D materials is a timely issue and reckons on general interest.

1.2 Outline of Thesis

In the present thesis we will examine single-particle and collective excitations of quasi-2D materials including monolayer and bilayer graphene and layered organic crystal α-(BEDT-TTF)$_2$I$_3$ (aI3). Our investigations will exclusively focus on properties in a strong magnetic field, either in the integer quantum Hall (IQH) regime, or in a magnetic field where quantum Hall ferromagnetic (QHF) states appear.

In Chap. 2 we present the materials we are dealing with in the present thesis. We focus on basic material properties and the low-energy band structure of each material, and derive the Landau level (LL) spectrum and orbitals necessary for further calculations. We also give a short outlook on experiments in each case to give a general context for our theoretical investigations. Besides reviewing the literature, however, we demonstrate how the relativistic covariance of the underlying Dirac equation of massless fermions in aI3 can be used to deduce its LL spectrum. Our contribution is to draw a parallel between aI3 in a magnetic field and graphene in a crossed magnetic and electric fields, emphasizing the same role that the tilt of the cones and the electric field play in each system respectively.

Chap. 3 is devoted to the magneto-optical properties calculated in a single-particle picture for aI3 in a magnetic and for graphene in a magnetic and an in-plane electric fields. In both cases the rotational symmetry is broken either by an in-plane electric field or the tilt of the Dirac cones. The reduced symmetry in such systems makes the allowed dipolar optical transitions evolve into a fan of interband transitions. We analyze the emerging optical properties, and predict that the infrared absorption spectra yield quantitative information on the tilted Dirac cone structure in aI3.

In Chap. 4 we study the collective modes of the low-energy continuum model of aI3 with tilted anisotropic Dirac cones. We show that the tilt of the cones causes a unique intervalley damping effect: the upper-hybrid mode of one cone is damped by the particle-hole continuum of the other cone in generic directions. Furthermore, as some experimental findings and *ab initio* calculations indicate that besides the massless carriers massive ones are also present in aI3, we extend our analysis of the collective modes to incorporate both carrier types. Notably, we analyze how the presence of

massive carriers affects the total response, and demonstrate how doping can tune aI3 between regimes of isotropic and anisotropic screening.

In the last chapter we analyze bilayer graphene in strong magnetic fields, when either IQH states or QHF states appear. Though in the former case a standard Landau quantization serves an excellent explanation for the appearance of plateaus, in the latter case they arise due to interactions. Nevertheless, the low-energy excitations in both cases are magnetoexcitons, whose dispersion relation depends on single- and many-body effects in a complicated manner. We find that the mixing of different LL transitions not only renormalizes the magnetoexciton modes, but essentially changes their spectra and orbital character at finite wavelength. We conclude by mentioning some experimental possibilities, e.g. inelastic light scattering experiments, through which our predictions can be probed.

Chapter 2

Quasi-Two-Dimensional Material Systems

This introductory chapter is devoted to those quasi-2D electron systems that are the subject matter of the present thesis. Our aim is to review the general properties of these systems, even though we shall limit ourselves to those features only that are essential for further analysis. We start our discussion with a short and up-to-the-point section on the conventional two-dimensional electron gas (2DEG). We introduce our basic notation and derive the Landau spectrum and the corresponding eigenfunctions. Afterwards, we turn our attention to monolayer and bilayer graphene. We review the basic electronic properties and the most noteworthy experimental connections, but here again much of the emphasis is given to the derivation of the eigenstates and eigenfunctions in a perpendicular magnetic field, which we will rely on in later chapters. Finally, we introduce the layered organic conductor aI3 and provide a basic description of its high pressure phase that hosts massless Dirac fermions. We conclude the chapter with an overview of related organic compounds.

2.1 Landau Level Spectrum of Conventional Two-Dimensional Electron Gas

Today conventional 2DEG is routinely realized in, among other systems, the semiconductor - oxide interface of MOSFETs (metal-oxide-semiconductor field-effect transistor) or the inversion layer of GaAs-$Al_xGa_{1-x}As$ heterostructures and quantum wells. The properties of such an electron system is described in detail from various aspects in e.g. [4], [52], [151]. Here we restrict our attention to the single-particle eigenstates and eigenfunctions in a perpendicular magnetic field $\mathbf{B} = (0, 0, B)$. The corresponding Hamiltonian reads

$$\hat{H}_{\mathrm{Q}} = \frac{(\hbar\mathbf{q} + e\mathbf{A})^2}{2m_Q}, \tag{2.1}$$

where subscript Q refers to the word *quadratic*, $\mathbf{A}$ is the vector potential, m_Q is the mass of the particle, $\mathbf{q} = -i\nabla$, $\hbar$ is the reduced Planck constant and $e > 0$ is the elementary charge. The LL spectrum is given by

$$\epsilon_n^{\mathrm{Q}} = \hbar\omega_c \left(n + \frac{1}{2}\right), \tag{2.2}$$

where $\omega_c = eB/m_Q$ is the appropriate cyclotron frequency and $n \geq 0$ is an integer. Note that ϵ_n^{Q} is a linear function of both the LL index n and the magnetic field B. The

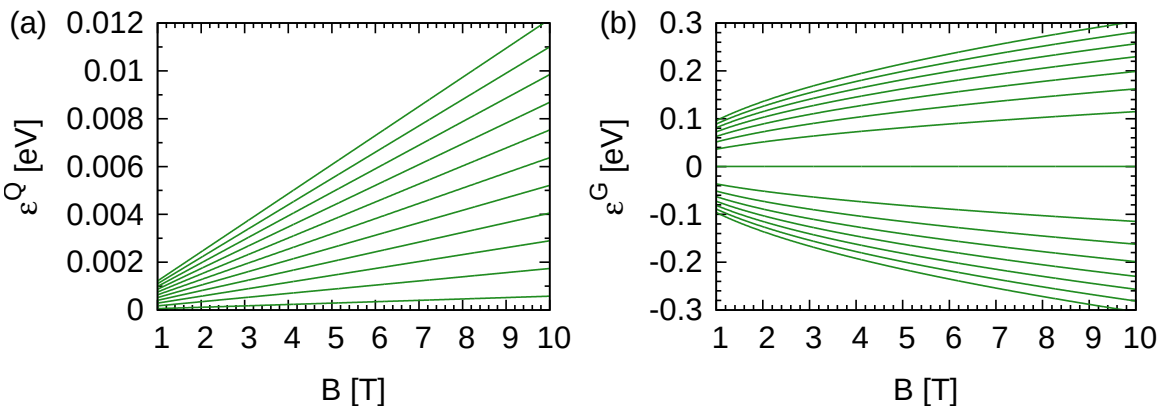

Figure 2.1: Lowest few LLs as a function of the magnetic field. Panel (a): 2DEG with $m_Q = m_0$, where m_0 stands for the electron rest mass. Here we use Eq. 2.2. Panel (b): LL spectrum of graphene using Eq. 2.10; the Fermi velocity is taken to be $v_F = 10^6$m/s.

lowest few LLs are depicted in Fig. 2.1(a) as a function of the magnetic field. Here and hereafter we use Landau gauge. With our particular gauge choice the vector potential is $\mathbf{A} = (-yB, 0, 0)$, then the eigenstates are given in terms of the harmonic oscillator eigenfunctions $\phi_n(y)$ introduced in Eq. A.5 and indexed with the quantum numbers n and k, as follows:

$$\phi_{n,k}(\mathbf{r}) = \frac{e^{ikx}}{\sqrt{2\pi}}\phi_n(y - l^2k) \equiv \frac{e^{ikx}}{\sqrt{2\pi}}\frac{1}{\sqrt{\sqrt{\pi}2^n n! l}}H_n(\frac{y}{l} - lk)e^{-(\frac{y}{l}-lk)^2/2}. \tag{2.3}$$

Here $l = \sqrt{\hbar/eB}$ is the magnetic length and $H_n(x)$ is the Hermite polynomial.

2.2 Monolayer Graphene

2.2.1 Graphene as a Single-Layer of Graphite - Preparation Methods

To start our discussion on single-layer graphene we first review the different methods of its preparation, with the intention to provide a general background for further discussion.

Graphite, a 3D allotrope of carbon, is made up of 2D graphene layers, which are coupled together by van der Waals forces, thus graphite offers itself for mechanical exfoliation. Indeed, the earliest method of producing monolayer graphene is the mechanical exfoliation of graphite or the so called *Scotch Tape Method*, during which monolayer or multilayer samples are exfoliated from a graphite crystal by a simple adhesive tape, see Refs. [122] and [183]. Mechanical exfoliation provided the highest-mobility samples so far, these monolayer flakes can be put on a substrate or can be suspended, though their size is not controllable.

Graphene can also be epitaxially grown on SiC or on hBN, though the graphene flakes produced with this method usually suffer from the effect of the surface. Another preparation method is chemical vapor deposition, which enabled us to produce extremely large samples, even up to width of 30 inches, see [7]. Chemical vapor deposition makes us capable of producing high-quality samples, which leads to immediate

applications, e.g. fabricating transparent electrodes. Various other, mainly chemical, methods are also available to produce graphene in a usually simple setup, however, the quality of the samples may largely depend on the preparation method itself. These methods include electrochemical exfoliation or graphene prepared in a liquid phase, for details see [94], [128] and [155]. A detailed summary of the preparation methods is given in [11].

2.2.2 Elementary Properties in Zero Magnetic Field

In graphene the carbon atoms are arranged in a hexagonal structure. This structure requires sp^2 hybridization of the 2s and 2p orbitals, leaving a single, unhybridized $2p_z$ orbital that is perpendicular to graphene's plane and provides an electron to participate in electrical conductivity.

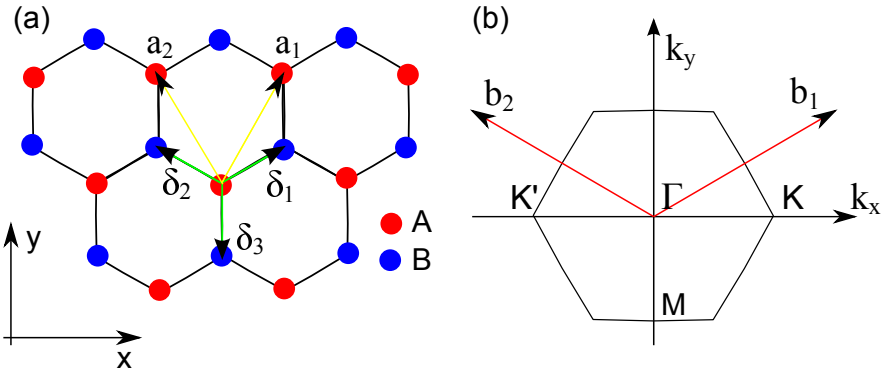

Figure 2.2: Panel (a): The honeycomb lattice of graphene. The two inequivalent atoms A and B of the primitive cell, the lattice vectors $\mathbf{a}_1 = (a\sqrt{3}/2, 3a/2)$ and $\mathbf{a}_2 = (-a\sqrt{3}/2, 3a/2)$, and the vectors connecting the nearest neighbour atoms $\delta_1 = (a\sqrt{3}/2, a/2)$, $\delta_2 = (-a\sqrt{3}/2, a/2)$, $\delta_3 = (0, -a)$ are also depicted. Panel (b): The first Brillouin zone of graphene with the reciprocal lattice vectors $\mathbf{b}_1 = (2\pi/a\sqrt{3}, 2\pi/3a)$, $\mathbf{b}_2 = (-2\pi/a\sqrt{3}, 2\pi/3a)$ and high-symmetry points, including K=$(4\pi/3\sqrt{3}a, 0)$ and K'=$(-4\pi/3\sqrt{3}a, 0)$.

Fig. 2.2(a) shows the honeycomb structure of graphene. Its lattice is a triangular lattice with a primitive cell containing two atoms denoted as A and B. Both the A and the B atoms respectively build up a triangular lattice, referred to as sublattices. The nearest neighbour atoms are connected by vectors δ_i with $i = 1, 2, 3$, while the lattice vectors $\mathbf{a}_1$ and $\mathbf{a}_2$ connect two A or two B atoms. a denotes the carbon-carbon

distance, which is $a \approx 1.42$ Å. The corresponding Brillouin zone is also a hexagon, with two inequivalent corner points traditionally denoted as K and K', see Fig. 2.2(b).

The simplest, but most frequently used band structure model of graphene is the tight-binding model, first derived by Wallace in 1947 in Ref. [168]. Note that Ref. [12] gives a detailed analysis of the topic. In second quantized formalism the tight-binding Hamiltonian reads as

$$\hat{H}_{\mathrm{G}} = -t \sum_{<i,j>,\sigma} [a^{\dagger}_{\sigma,i} b_{\sigma,j} + h.c.] - t' \sum_{\ll i,j \gg,\sigma} [a^{\dagger}_{\sigma,i} a_{\sigma,j} + b^{\dagger}_{\sigma,i} b_{\sigma,j} + h.c.]. \tag{2.4}$$

$a_{\sigma,j}$ ($b_{\sigma,j}$) are annihilation operators that annihilates an electron with σ spin at site $\mathbf{R}_j$ of sublattice A (B). $< i, j >$ ($\ll i, j \gg$) denotes a summation through the (next-)nearest neighbours, $h.c.$ denotes Hermitian conjugation. The value of the nearest neighbour hopping amplitude $t \approx 2.8$eV, while the next-nearest neighbour hopping amplitude is estimated to be $t' \approx 0.1$eV, see [27]. Neglecting the next-nearest neighbour hopping as

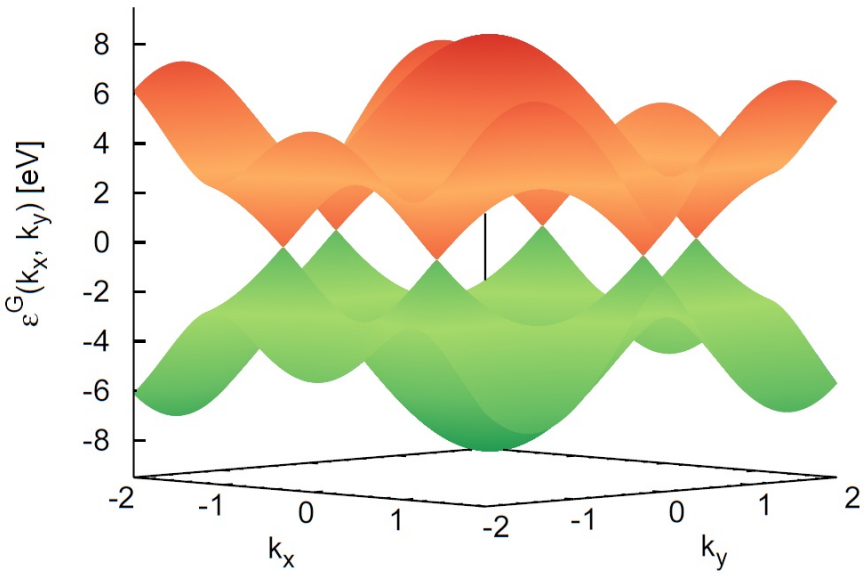

Figure 2.3: The dispersion relation of graphene according to Eq. 2.5. The $\mathbf{k}$ is measured in the units of 10^{10} 1/m.

a first approximation, the energy spectrum in the wave vector space is

$$\epsilon^{\mathrm{G}}(\mathbf{k}) = \pm t \sqrt{3 + 2\cos(\sqrt{3}k_x a) + 4\cos(\sqrt{3}k_x a/2)\cos(3k_y a/2)}. \tag{2.5}$$

The $\pm$ sign denotes the conduction and the valence bands, respectively. $\mathbf{k}$ is measured from the Γ point of the first Brillouin zone, as shown in Fig. 2.2(b). These bands touch each other at the corner points of the Brillouin zone, and when graphene is neutral the contact points coincide with the Fermi energy. The dispersion relation starts out linearly from these points, see Fig. 2.3. By including the next-nearest neighbour hopping term, the conduction and the valence band become asymmetric, but the low-energy spectrum does not change considerably. As we are interested in the low-energy regime, we only retain terms with t in the following.

One can achieve further simplification by expanding the Fourier transformed tight-binding Hamiltonian around both K and K', as was done by Semenoff in Ref. [145]. We recover the famous Hamiltonian

$$\hat{H}_{\mathrm{G}}^{\xi} = \hbar v_F[\xi q_x \sigma_x + q_y \sigma_y], \tag{2.6}$$

where $v_F \approx 10^6$m/s is the Fermi velocity and the wave vector $\mathbf{q}$ is measured from either cone K ($\xi = 1$) or K' ($\xi = -1$), these points are also referred to as valleys.[1] Here and hereafter σ_i with $i = 0, x, y, z$ denotes the identity matrix and the Pauli matrices. Remarkably, the time-dependent Schrödinger equation corresponding to the Hamiltonian in Eq. 2.6 is formally identical with the 2+1 dimensional Dirac equation of massless fermions, therefore K and K' points are customarily called Dirac points, and it is in this context that one can call the electrons of graphene as massless Dirac fermions.[2] The linear dispersion relation and the two-component spinorial eigenfunctions are

$$\epsilon^{\mathrm{G}}(\mathbf{q}) = \pm \hbar v_F q, \tag{2.7}$$

$$\Phi_{\mathbf{q}}^{\mathrm{G},\xi=1}(\mathbf{r}) = \frac{e^{i\mathbf{qr}}}{\sqrt{2}} \begin{pmatrix} e^{-i\vartheta/2} \\ \pm e^{i\vartheta/2} \end{pmatrix}, \quad \Phi_{\mathbf{q}}^{\mathrm{G},\xi=-1}(\mathbf{r}) = \frac{e^{i\mathbf{qr}}}{\sqrt{2}} \begin{pmatrix} e^{i\vartheta/2} \\ \pm e^{-i\vartheta/2} \end{pmatrix}. \tag{2.8}$$

Here $q = |\mathbf{q}|$ and $\vartheta = \arctan(q_y/q_x)$. Note that the above expansion is valid if the wave

[1] We use the (A, B) basis in both cones for further computational ease. It is customary to use the (B, A) basis in K', which may be calculated from the present form by a unitary transformation $U = i\sigma_x$.

[2] This fact was first pointed out in [145], the nature and symmetries of graphene's Dirac equation is discussed, among others, in Ref. [105].

vector $|\mathbf{q}| \ll |\mathbf{K}| \sim 1/a$, where a is the lattice constant. This gives a 1.5eV cutoff in energy.

The components of this spinorial wave function may be identified as components of a pseudospin. The first component that represents sublattice A is now interpreted as the *up spin*, denoted as $\Uparrow$, the second component (sublattice B) is similarly interpreted as the *down spin* ($\Downarrow$). Note that this pseudospin appears due to the two sublattices and is independent of the real spin of the electrons.[3]

As an experimental outlook we mention that the angle-resolved photoemission spectroscopy (ARPES), which directly resolves the electronic structure of the material in energy-momentum space, made it possible to observe the conical dispersion relation. The observed deviation from the predictions of the single-particle picture shed light on possible interaction effects, including velocity renormalization, see [22]. Scanning tunnelling spectroscopy (STS) provides direct access to the density of states, one of the first STS measurement is made by Li *et al.* in Ref. [90].

2.2.3 Graphene in a Perpendicular Magnetic Field

In this subsection we consider a graphene sheet in a perpendicular magnetic field $\mathbf{B} = (0, 0, B)$. As we are concentrating on the low-energy regime, it is convenient to take the Hamiltonian in Eq. 2.6, which describes the Dirac cones around K and K', as our starting point. In a magnetic field, the appropriate Hamiltonian is deduced from Eq. 2.6 by minimal coupling. Again, we use Landau gauge with $\mathbf{A} = (A_x, A_y, A_z) = (-yB, 0, 0)$. We apply the convention that $\mathbf{q} = -i\nabla$ and $\mathbf{p} = (q_x + eA_x/\hbar, q_y + eA_y/\hbar) = (q_x - y/l^2, q_y)$ in our particular gauge choice. Then the Hamiltonian becomes:

$$\hat{H}_{\mathrm{G}}^{\xi} = \hbar v_F[\xi p_x \sigma_x + p_y \sigma_y] = \hbar v_F[\xi(q_x - \frac{y}{l^2})\sigma_x + q_y \sigma_y]. \tag{2.9}$$

[3]It is common practice to describe the eigenfunctions in Eq. 2.8 with their helicity. The helicity operator, which is the projection of the momentum operator along the spin direction, is defined for graphene in Refs. [54] and [27]. One finds that $\Phi_{\mathbf{q}}^{\mathrm{G},\xi=1}$ and $\Phi_{\mathbf{q}}^{\mathrm{G},\xi=-1}$ have well-defined helicity, they are eigenfunctions of the helicity operator. Note that in the ultra-relativistic limit the helicity operator coincides with the chirality operator, therefore one may also say that a Dirac electron has well-defined chirality, the notion *chiral electrons* is also frequently used. A related issue is that the Berry's phase of massless electrons of graphene is π, for detailed derivation see Ref. [179].

The eigenvalues and eigenfunctions of this Hamiltonian is derived by McClure in [103] and the derivation is reproduced in App. A in great detail. The LLs are

$$\epsilon_n^{\mathrm{G}} = \mathrm{sgn}(n)\sqrt{2|n|}\frac{v_F\hbar}{l} \tag{2.10}$$

with integer n, $\mathrm{sgn}(n)$ denotes the signum function. Note that the energy spectrum unusually scales with $\sqrt{n}$ and $\sqrt{B}$, see Fig. 2.1(b) for comparison with 2DEG.

The corresponding eigenfunctions in cone $\xi = 1$ reads

$$\Phi_{|n|,k}^{\mathrm{G},\xi=1}(x,y) = \frac{1}{\sqrt{2}}\frac{e^{ikx}}{\sqrt{2\pi}}\begin{pmatrix}\mathrm{sgn}(n)\phi_{|n-1|}(y-kl^2)\\ -\phi_{|n|}(y-kl^2)\end{pmatrix}, \tag{2.11}$$

similarly in cone $\xi = -1$

$$\Phi_{|n|,k}^{\mathrm{G},\xi=-1}(x,y) = \frac{1}{\sqrt{2}}\frac{e^{ikx}}{\sqrt{2\pi}}\begin{pmatrix}\phi_{|n|}(y-kl^2)\\ \mathrm{sgn}(n)\phi_{|n-1|}(y-kl^2)\end{pmatrix}, \tag{2.12}$$

where $\phi_n(y)$ is the harmonic oscillator function of Eq. A.5.

Shubnikov-de Haas and IQH measurements can be used to directly access the unique LL structure of graphene. In Ref. [122] Novoselov *et al.* identified the quantum Hall plateaus in Hall conductivity σ_{xy}. As opposed to the conventional 2DEG with plateaus at $\sigma_{xy} = 2n\frac{e^2}{h}$, in graphene they appear at $\sigma_{xy} = \pm 2(2n+1)\frac{e^2}{h}$, that is when the filling factor is $\nu = 2(2n+1)$, n is a positive integer in both cases. The fourfold degeneracy of the LLs comes from the spin and valley-pseudospin.[4] This unusual QHE is the fingerprint of graphene, it made its identification possible.

A further branch of measurements which directly probes the special LL structure is magnetospectroscopy; these measurements are reviewed in Chap. 3 and in Ref. [11].

[4]Note that spin is only a good quantum number at the $B = 0$T limit. However, as the Zeeman splitting is tiny compared to any other energy scales, see [54], taking spin as a good quantum number is a reliable approximation.

2.2.4 Relativistic Properties of Massless Fermions in Graphene

As we have seen, graphene hosts *relativistic* electrons moving with the Fermi velocity v_F instead of the speed of light c. This subsection is devoted to show how the machinery of relativistic quantum mechanics can be used to deduce the LL spectrum when graphene is placed in a perpendicular magnetic and an in-plane electric fields.[5]

Consider the in-plane electric field $\mathbf{E} = (0, -E_{\|}, 0)$. The corresponding scalar potential $\phi = E_{\|} y$. We use Landau gauge, as was given previously. The Hamiltonian of the electrons in graphene under these circumstances is

$$\hat{H}^{\xi}_{\mathrm{E}_{\|}} = \hbar v_F[\xi p_x \sigma_x + p_y \sigma_y] - eE_{\|} y \sigma_0. \tag{2.13}$$

The eigenvalue problem may be solved algebraically following Peres [130], but here we reproduce the solution of Lukose *et al.*, see [96]. Their procedure is based on the covariance of the Dirac equation corresponding to the Hamiltonian in Eq. 2.13. One can boost from the laboratory frame R to another frame of reference R' in such a way that in the R' frame the electric field vanishes and the magnetic field is rescaled. In the R' frame the solution of the eigenvalue problem of the transformed Hamiltonian is readily given. The solution of the original problem may be found by applying the inverse Lorentz transformation, that is we need to boost back the eigenvalues and eigenvectors to the lab frame R.[6]

Let us introduce contravariant and covariant coordinate *three-vectors* and the metric tensor following the notations of Ref. [59]:

[5]The relativistic nature of the electrons in graphene manifests itself in many other ways. Consider the scattering of chiral electrons by a square potential. Using the wave function in Eq. 2.8 one can calculate the probability that a chiral electron transmits the barrier, see Ref. [78]. With normal incidence, the transmission is identically 1, independent of the barrier width, that is the barrier is transparent and backscattering is absent. This is the manifestation of the Klein paradox in graphene. Using extremely narrow graphene heterostructures Young and Kim in Ref. [178] observed the Klein paradox in a condensed matter system. A related relativistic phenomenon is the so called Zitterbewegung, which has been discussed theoretically in Refs. [32], [36] and [77], but no experiments are available up to now.

[6]We emphasize that in the Lorentz boost we apply v_F appears instead of the speed of light c.

$$x^\mu = (v_F t, x, y), \qquad x_\mu = (v_F t, -x, -y), \qquad g_{\nu\mu} = \begin{pmatrix} 1 & 0 & 0 \\ 0 & -1 & 0 \\ 0 & 0 & -1 \end{pmatrix},$$

where t denotes time. We also introduce here the Lorentz transformation rules between the lab frame R and the coordinate system R'. All covariant and contravariant quantities transform in the same way as the particular components of the coordinate three-vector:

$$x'^\mu = \Lambda^\mu_\nu \, x^\nu, \qquad x'_\mu = (\Lambda^{-1})^\nu_\mu \, x_\nu.$$

Here Λ (Λ^{-1}) is the (inverse) Lorentz transformation. For further use we also introduce the following notations for the momentum, the gradient operator, and the vector potential, respectively:

$$p^\mu = (\frac{\epsilon}{v_F}, \hbar k_x, \hbar k_y), \qquad \partial^\mu = \frac{\partial}{\partial x_\mu} = (\frac{1}{v_F}\frac{\partial}{\partial t}, -\frac{\partial}{\partial x}, -\frac{\partial}{\partial y}),$$
$$A^\mu = (\frac{\phi}{v_F}, A_x, A_y) = (\frac{E_\parallel y}{v_F}, -yB, 0).$$

Having set down the notation, we start with the time-dependent Schrödinger equation corresponding to the Hamiltonian 2.13 with the choice of $\xi = 1$ (cone K). By applying the notation introduced above and by multiplying the Schrödinger equation by σ_z we arrive at the covariant form of the Dirac equation in the lab frame R:

$$-i\hbar v_F \gamma_\mu (\partial^\mu - \frac{ie}{\hbar} A^\mu) \Phi(x, y) = 0. \tag{2.14}$$

Here $\gamma_0 = \sigma_z$, $\gamma_1 = -\sigma_z\sigma_x$, and $\gamma_2 = -\sigma_z\sigma_y$.[7] We are in the position to construct the appropriate Lorentz boost which should transform $A^\mu = (\frac{E_\parallel y}{v_F}, -yB, 0)$ in R to $A'^\mu = (0, -yB', 0)$ in R'. By straightforward algebra the Lorentz transformation turns

[7] The γ_μ matrices fulfill the requirements that γ_0 is Hermitian and unitary, while $\gamma_{1\backslash 2}$ are both anti-Hermitian and unitary. Moreover, they also fulfill the commutation relation $\gamma_\nu\gamma_\tau + \gamma_\tau\gamma_\nu = 2g_{\nu\tau}\sigma_0$ [59], that is they satisfy the Clifford algebra.

out to be

$$\Lambda = \begin{pmatrix} \cosh\zeta & \sinh\zeta & 0 \\ \sinh\zeta & \cosh\zeta & 0 \\ 0 & 0 & 1 \end{pmatrix}, \tag{2.15}$$

where we have introduced the rapidity or boost parameter ζ as $\tanh\zeta = \beta = E_{\parallel}/(v_F B) > 0$ and $\lambda = \sqrt{1-\beta^2}$. β is the ratio of the usual drift velocity $E_{\parallel}/B$ and the Fermi velocity v_F. Notice that $\tanh\zeta = \beta \leq 1$ is required by definition, this criterion should be fulfilled by an appropriate choice of the magnetic and the electric fields, see also discussion below. The rescaled magnetic field B' becomes $B' = \lambda B$, while the magnetic length rescales as $l' = l/\sqrt{\lambda}$. By construction, the Hamiltonian $\hat{H}' = \hbar v_F[(q_x - y/l'^2)\sigma_x + q_y\sigma_y]$ has a simple form, its eigenstates and eigenvalues have been given in Eqs. 2.10 and 2.11, though here we shall use the rescaled magnetic length l'. Knowing the eigenvalue spectrum in R', that is ϵ'_n, we apply the inverse boost Λ^{-1} on the momentum three-vector $p'^{\mu} = (\epsilon'_n/v_F, \hbar k'_x, \hbar k'_y)$ and solve the system of equations to ϵ_n. Then we recover the energy spectrum in frame R:

$$\epsilon_n^{\mathrm{E}_{\parallel}} = \mathrm{sgn}(n)\sqrt{2|n|}\frac{\hbar v_F}{l}\lambda^{3/2} - \hbar k\beta v_F. \tag{2.16}$$

We note that the same system of equations should be used to determine the argument Υ_n of the wave function, defined later on.

As compared with graphene in a magnetic field, but with $E_{\parallel} = 0$, the energy levels are rescaled by $\lambda^{3/2}$, but they preserve their $\sqrt{n}$ and $\sqrt{B}$ dependence. Fig. 2.4(a) shows the LL spectrum as a function of the magnetic field B. Panel (b) depicts how the LL spectrum changes with β for a fixed magnetic field. It is evident that by increasing the electric field the LLs are getting closer and at a critical electric field determined by the condition $\beta = 1$, the LL spectrum collapses, see also [96]. We emphasize that the Lorentz boost Λ of Eq. 2.15 is only valid in the $\beta \leq 1$ range. By increasing further the electric field one finds non-localized electrons, the study of these states is outside the scope of the present thesis.

To proceed, we determine the eigenfunctions of the Hamiltonian in frame R. For this, we need to construct the matrix S, which represents the Lorentz boost in spinor space

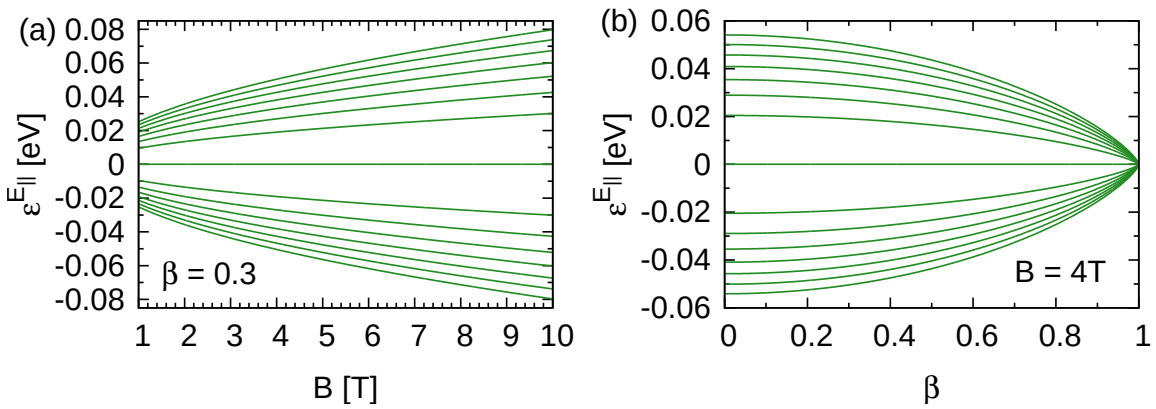

Figure 2.4: Lowest few LLs of Eq. 2.16 as a function of the magnetic field for fixed $\beta = 0.3$ (panel (a)), and as a function of β for fixed $B = 4$T (panel (b)). $k = 0$ is chosen.

as $S\Phi = \Phi'$. Making the usual assumption that the γ_μ matrices have the same form in all frames and that S satisfies $S^{-1}\gamma_\mu S = (\Lambda^{-1})^\nu_\mu \gamma_\nu$ (see [59]), we get $S = \exp(\frac{\zeta}{2}\sigma_x)$. After the application of S^{-1} and proper normalization the wave function becomes for $n \neq 0$:

$$\Phi^{\xi=1}_{n,k}(\mathbf{r}) = \frac{1}{\sqrt{4(1+\lambda)}} \left[\begin{pmatrix} -\beta \\ 1+\lambda \end{pmatrix} \phi_{n,k}(\mathbf{r}) + \begin{pmatrix} -1-\lambda \\ \beta \end{pmatrix} \mathrm{sgn}(n)\phi_{n-1,k}(\mathbf{r}) \right], \tag{2.17}$$

while for the $n = 0$ LL,

$$\Phi^{\xi=1}_{0,k}(\mathbf{r}) = \frac{1}{\sqrt{2(1+\lambda)}} \begin{pmatrix} -\beta \\ 1+\lambda \end{pmatrix} \phi_{0,k}(\mathbf{r}). \tag{2.18}$$

We have used the subformulas

$$\phi_{n,k}(\mathbf{r}) = \frac{e^{ikx}}{\sqrt{2\pi}} \frac{\lambda^{1/4}}{(2^{|n|}|n|!\sqrt{\pi}l)^{1/2}} e^{-\Upsilon_n^2/2} H_{|n|}(\Upsilon_n), \tag{2.19}$$

and

$$\phi_{n-1,k}(\mathbf{r}) = \frac{e^{ikx}}{\sqrt{2\pi}} \frac{\lambda^{1/4}}{(2^{|n-1|}|n-1|!\sqrt{\pi}l)^{1/2}} e^{-\Upsilon_n^2/2} H_{|n-1|}(\Upsilon_n), \tag{2.20}$$

with the argument

$$\Upsilon_n = \sqrt{\lambda}y/l - \sqrt{\lambda}lk - \beta\sqrt{2|n|}\mathrm{sgn}(n). \tag{2.21}$$

Notice that Υ_n depends on the LL index (including its sign). Also, the argument is identical for functions $\phi_{n,k}$ and $\phi_{n-1,k}$, even though their indeces are different.

From Eq. 2.13 one can derive the eigenvalues and eigenfunctions for cone K' ($\xi = -1$) in a similar manner. Note that the electric field does not change sign in cone K'. The eigenvalues are identical with that of cone K in Eq. 2.16, while the wave function differs. For $n \neq 0$ in cone $\xi = -1$, the orbitals are

$$\Phi_{n,k}^{\xi=-1}(\mathbf{r}) = \frac{1}{\sqrt{4(1+\lambda)}} \left[\begin{pmatrix} 1+\lambda \\ \beta \end{pmatrix} \phi_{n,k}(\mathbf{r}) + \begin{pmatrix} \beta \\ 1+\lambda \end{pmatrix} \mathrm{sgn}(n)\phi_{n-1,k}(\mathbf{r}) \right], \tag{2.22}$$

while for $n = 0$

$$\Phi_{0,k}^{\xi=-1}(\mathbf{r}) = \frac{1}{\sqrt{2(1+\lambda)}} \begin{pmatrix} 1+\lambda \\ \beta \end{pmatrix} \phi_{0,k}(\mathbf{r}). \tag{2.23}$$

2.3 Bilayer Graphene

Bilayer graphene, as its band structure is entirely different from graphene, has also been the focus of intense research since its first experimental identification in 2006, see [123]. In their work Novoselov *et al.* measured the quantum Hall conductivity σ_{xy}, and found plateaus at $\sigma_{xy} = \pm 4n\frac{e^2}{h}$ with $n \geq 1$. This sequence of fourfold degenerate LLs and an eightfold degenerate *central Landau band* is the fingerprint of bilayer graphene and served as a clue for its identification. Similar IQH measurements at $\nu = \pm 4, \pm 8$ of Ref. [87] determined the activation gap. Besides the transport measurements, in Ref. [62] Henriksen *et al.* measured the cyclotron resonance via IR absorption spectroscopy and provided an experimental confirmation of the peculiar magnetic field dependence of the LL spectrum characteristic to the material. A related magneto-Raman experiment is presented in Ref. [43]. Other measurements, such as compressibility measurements, are also available for bilayer graphene for both zero and non-zero magnetic fields, see Ref. [64], reinforcing the validity of the single-particle picture. The peculiar LL structure of these chiral fermions with Berry's phase 2π was discussed in great detail by several authors in [60], [101], [102], [129], [182], and a detailed review is found in [41].

In bilayer graphene two single-layers of graphene are coupled together through van

der Waals forces, the distance between the two layers being 3.35 Å. The structure of bilayer graphene is shown in Fig. 2.5. Each layer consists of two sublattices, denoted A and B in the top layer and $\widetilde{A}$ and $\widetilde{B}$ in the bottom layer. In Bernal stacking [14] two sublattices, $\widetilde{A}$ and B in our notation, are exactly above/below one another, while the A sites are above the center of the hexagons in the bottom layer, and $\widetilde{B}$ sites are below the centers of hexagons in the top layer.

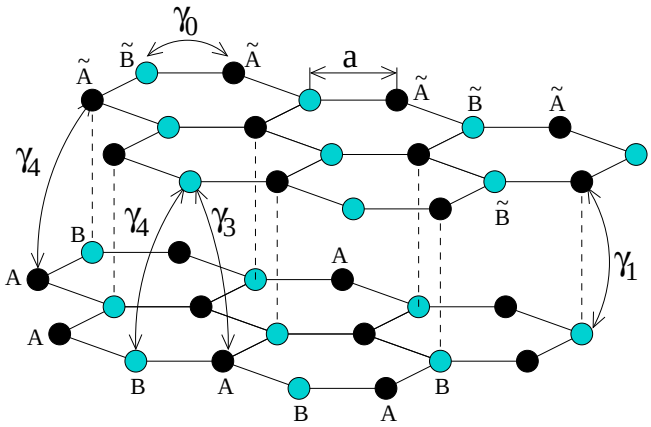

Figure 2.5: Bilayer graphene in Bernal stacking. The hopping parameters of the Slonczewski-Weiss-McClure model, conventionally denoted γ_0, γ_1, γ_3 and γ_4, are also indicated.

The low-energy physics of bilayer graphene can be adequately described by the tight-binding effective theories that specialize the Slonczewski-Weiss-McClure (SWM) model of graphite to the case of just two layers, see Refs. [104], [150] and [168]. In the vicinity of the inequivalent corners of the hexagonal first Brillouin zone K ($\xi = 1$) and K' ($\xi = -1$) this amounts to using the Hamiltonian in Refs. [60] and [102]:

$$\hat{H}_{\mathrm{B}}^{\xi} = \xi \begin{pmatrix} \frac{u-\Delta'}{2} & v_3\pi & -v_4\pi^\dagger & v\pi^\dagger \\ v_3\pi^\dagger & -\frac{u+\Delta'}{2} & v\pi & -v_4\pi \\ -v_4\pi & v\pi^\dagger & -\frac{u-\Delta'}{2} & \xi\gamma_1 \\ v\pi & -v_4\pi^\dagger & \xi\gamma_1 & \frac{u+\Delta'}{2} \end{pmatrix} - \Delta_Z\sigma_z, \tag{2.24}$$

where $\pi = \hbar p_x + i\hbar p_y$ and $\mathbf{p} = (p_x, p_y) = -i\nabla$ for zero magnetic fields. The diagonal of the Hamiltonian contains Δ', which is the on-site energy difference between the dimer sites $(\widetilde{A}, B)$ and the non-dimer sites $(\widetilde{B}, A)$. Its value is estimated to be $\Delta' \approx 0.006\gamma_0$

in [181], γ_0 is defined below. u is the potential energy difference between the layers, which may arise, e.g., because of an applied perpendicular electric field $E_\perp$.[8] In the non-diagonal elements one can readily identify various SWM hopping terms that are relevant in the bilayer case:

- $\gamma_0 = \gamma_{AB} = \gamma_{\widetilde{A}\widetilde{B}}$: intralayer hopping amplitude. The corresponding intralayer velocity: $v = \sqrt{3}a\gamma_0/2\hbar \approx 10^6$ m/s.
- $\gamma_1 = \gamma_{\widetilde{A}B}$: interlayer hopping amplitude. Its value is estimated to be $\gamma_1 \approx 0.133\gamma_0$ by Zhang *et al.* in [181].[9]
- $\gamma_3 = \gamma_{A\widetilde{B}}$: next-nearest-neighbour interlayer hopping amplitude, estimated to be $\gamma_3 \approx 0.1\gamma_0$ by [181]. The related velocity $v_3 = \sqrt{3}a\gamma_3/2\hbar$ is the trigonal warping parameter.
- $\gamma_4 = \gamma_{A\widetilde{A}} = \gamma_{B\widetilde{B}}$: interlayer next-nearest neighbour hopping amplitude. Its value is estimated to be $\gamma_4 = 0.063\gamma_0$ by Zou *et al.* in [186]. The related velocity is $v_4 = \sqrt{3}a\gamma_4/2\hbar$.

The Hamiltonian in Eq. 2.24 acts in the basis of sublattice Bloch states $(A, \widetilde{B}, \widetilde{A}, B)$ in valley K and $(\widetilde{B}, A, B, \widetilde{A})$ in valley K'. Note that the second term of the Hamiltonian $\Delta_Z = g\mu_B B$ is the Zeeman energy with g, μ_B and B being the gyromagnetic factor, the Bohr magneton and the magnetic field respectively; this term acts on the spin space. The Hamiltonian is block-diagonal in the valley index, which is conveniently described as a pseudospin. In the special case $u = 0$ the system has SU(2) pseudospin rotation symmetry. In the theoretical limit $\Delta_Z \to 0$ this is raised to SU(4) symmetry. Throughout our subsequent analysis of bilayer graphene presented in Chap. 5 we will treat Δ_Z and u as small perturbations in comparison with the interaction energy, i.e., we will work in the $\Delta_Z, u \ll e^2/(4\pi\epsilon_0\epsilon_r l)$ limit, where ϵ_0 is the vacuum dielectric constant and ϵ_r is the relative dielectric constant.

[8] As a side note we mention that the bandgap is tunable by an applied electric field, as was revealed by Zhang *et al.* in Ref. [184], where they directly observed this with infrared spectroscopy. Similar measurements were conducted in [26], [99] with related theoretical works available in Refs. [1], [116], [169]. The band gap can also be tuned by selectively controlling the carrier concentration in each layer, see [124].

[9] Note that other estimates are available in the literature concerning the values of the SWM parameters, see [92] as an example. We use these values for the robustness of our analysis at the second part of the section.

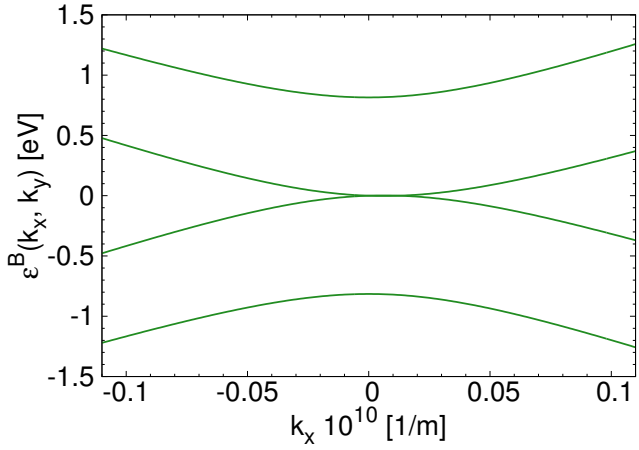

Figure 2.6: Dispersion relation of bilayer graphene around cone K ($\xi = 1$) based on Ref. [102]. $\mathbf{k}$ is measured in units of 10^{10} 1/m. For clarity only the $k_y = 0$ plane is displayed. $u = 0$ limit is taken.

McCann *et al.* in [102] determined the eigenvalue spectrum $\epsilon^{\mathrm{B}}(\mathbf{k})$ of Hamiltonian $\hat{H}^{\xi}_{\mathrm{B}}$ and found 4 valley degenerate bands, which are paraboloids in the $|\epsilon| < \frac{1}{2}\gamma_1(v_3/v)^2$ range. Fig. 2.6 reproduces these bands in the $k_y = 0$ plane.

For describing transport properties we are only interested in the low-energy bands, therefore it is customary to introduce a 2×2 effective Hamiltonian instead of Eq. 2.24 following the derivation in [102], keeping in mind that any approximations containing information only about the 2 low-energy bands is valid for small momenta and that such an approximation neglects parameters γ_4 and Δ'. $\hat{H}^{\xi}_{\mathrm{B,\ eff.}}$ reads as

$$\hat{H}^{\xi}_{\mathrm{B,\ eff.}} = -\frac{v^2}{\gamma_1}\begin{pmatrix} 0 & (\pi^\dagger)^2 \\ \pi^2 & 0 \end{pmatrix} + \xi v_3 \begin{pmatrix} 0 & \pi \\ \pi^\dagger & 0 \end{pmatrix} + \xi u \left[\frac{1}{2}\begin{pmatrix} 1 & 0 \\ 0 & -1 \end{pmatrix} - \frac{v^2}{\gamma_1^2}\begin{pmatrix} \pi^\dagger\pi & 0 \\ 0 & -\pi\pi^\dagger \end{pmatrix}\right]. \tag{2.25}$$

The above Hamiltonian is valid in the $|\epsilon| < \gamma_1/4$ range, and it acts on $(A, \widetilde{B})$ in valley K and $(\widetilde{B}, A)$ in valley K'. Note that the last term vanishes in the $u \to 0$ limit and the second term is responsible for the splitting of the paraboloid into 4 Dirac cones per valley in the smallest energy regime $|\epsilon| < \frac{1}{2}\gamma_1(v_3/v)^2$, the phenomenon usually referred to as trigonal warping. Fig. 2.7 reproduces the dispersion relation $\epsilon^{\mathrm{B}}(\mathbf{k})$ in the smallest energy range where trigonal warping is relevant. Interesting to note that the number of Dirac points may change due to strain or translational

displacement of the graphene layers with respect to one another, as examined in detail by de Gail *et al.* in [48] using a topological point of view. Furthermore, trigonal warping crucially modifies e.g. the minimal conductivity of bilayer graphene, see [33]. For our purposes, however, it is adequate to neglect this term and work in the intermediate energy range $\frac{1}{2}\gamma_1(v_3/v)^2 < |\epsilon| < \gamma_1/4$. To convince ourselves about the accuracy of our approximations in the second part of the section we systematically compare the full and the effective model.

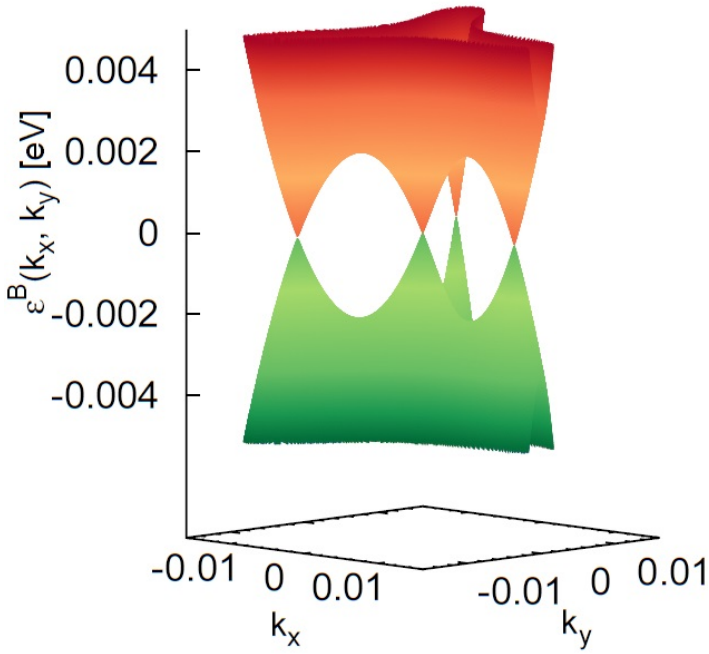

Figure 2.7: The lowest-energy dispersion relation $\epsilon^{\mathrm{B}}(\mathbf{k})$ of bilayer graphene determined by the effective Hamiltonian $\hat{H}^{\xi}_{\mathrm{B,\,eff.}}$ of Eq. 2.25 taking $u = 0$. The momentum $\mathbf{k}$ is measured in units of 10^{10} 1/m.

In the above simplified model the LLs and Landau orbitals, respectively, become, see [102],

$$\epsilon^{\mathrm{B}}_{0,\xi} = \frac{\xi u}{2}, \quad \epsilon^{\mathrm{B}}_{1,\xi} = \frac{\xi u}{2} - \xi\frac{u\hbar\omega_c}{\gamma_1}, \quad \epsilon^{\mathrm{B}}_{n,\xi} = \mathrm{sgn}(n)\hbar\omega_c\sqrt{|n|(|n|-1)} - \xi\frac{u\hbar\omega_c}{2\gamma_1}, \tag{2.26}$$

$$\Phi^{\mathrm{B},\xi}_{0,k} = \begin{pmatrix} \phi_{0,k}(\mathbf{r}) \\ 0 \end{pmatrix}, \quad \Phi^{\mathrm{B},\xi}_{1,k} = \begin{pmatrix} \phi_{1,k}(\mathbf{r}) \\ 0 \end{pmatrix}, \quad \Phi^{\mathrm{B},\xi}_{n,k} = \begin{pmatrix} A^{(n)}_{\xi}\phi_{|n|,k}(\mathbf{r}) \\ B^{(n)}_{\xi}\phi_{|n|-2,k}(\mathbf{r}) \end{pmatrix}, \tag{2.27}$$

$$A^{(n)}_{\xi} = \frac{1}{C^{(n)}_{\xi}}, \quad B^{(n)}_{\xi} = \frac{1}{C^{(n)}_{\xi}}\frac{\epsilon^{\mathrm{B}}_{n,\xi} - \xi\frac{u}{2} + \xi\frac{u|n|\hbar\omega_c}{\gamma_1}}{\hbar\omega_c\sqrt{|n|(|n|-1)}}.$$

Here $n \neq -1$ is an integer, $C_\xi^{(n)}$ is an appropriate normalization factor, and $\phi_{n,k}(\mathbf{r})$ are the single-particle states in the conventional 2DEG given in Eq. 2.3. We have also introduced $\omega_c = 2eBv^2/\gamma_1$. Notice that in the $u = 0$ limit $A_\xi^1 = A_\xi^0 = 1$, $B_\xi^1 = B_\xi^0 = 0$ and $A_\xi^{(n)} = \mathrm{sgn}(n) B_\xi^{(n)} = 1/\sqrt{2}$ if $n \geq 2$, independent of ξ.

The $n = 0, 1$ orbitals are degenerate in the $u \to 0$ limit, furthermore at realistic values of Δ_Z and u, the $n = 0, 1$, $\xi = \pm 1$, $\sigma = \uparrow, \downarrow$ states form a quasi-degenerate band called the *central Landau band* or *central Landau level octet*. IQH states appear at filling factor $\nu = \cdots, -8, -4, 4, 8, \cdots$; they correspond to completely filled LLs with indeces $n = \cdots, -3, -2, 1, 2, \cdots$. Note also that the fourfold degeneracy of the rest of the LLs comes from spin and valley pseudospin, similarly to monolayer graphene. Notice that in the central Landau band the valley and the layer (top or bottom) may be used interchangeably, as the wave functions in valley K are localized in one layer, while those of valley K' are localized in the other layer. Fig. 2.8 shows the first few LLs as a function of the magnetic field.[10]

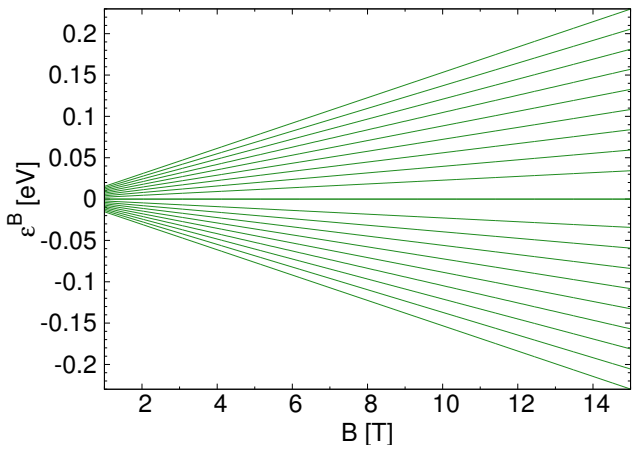

Figure 2.8: Lowest few LLs of Eq. 2.26 as a function of the magnetic field.

In the remaining part of the section we would like to determine to what extent the simplified two-band model $\hat{H}^\xi_{\mathrm{B,\,eff.}}$ in Eq. 2.25 is adequate for the description of the low-energy band structure instead of the four-band Hamiltonian $\hat{H}^\xi_{\mathrm{B}}$ in Eq. 2.24.

[10]In the lowest-energy range where trigonal warping is relevant each cone produces its own LL spectrum respectively, though the spacing between the LLs of the central cone and the others is different. This leads to a sequence of two nondegenerate LLs and a third fourfold degenerate LL, see [102].

Our goal is to systematically explore the range of applicability of this simplified model, which neglects several parameters of the SWM model, notably γ_3, γ_4, and Δ'.

Our method is to calculate the eigenvalues of the Hamiltonian in Eq. 2.24 numerically, and test how the eigenvalues are modified by tuning the neglected parameters $\gamma_3 = \gamma_4 = \Delta' = 0$ from zero to their literary values.

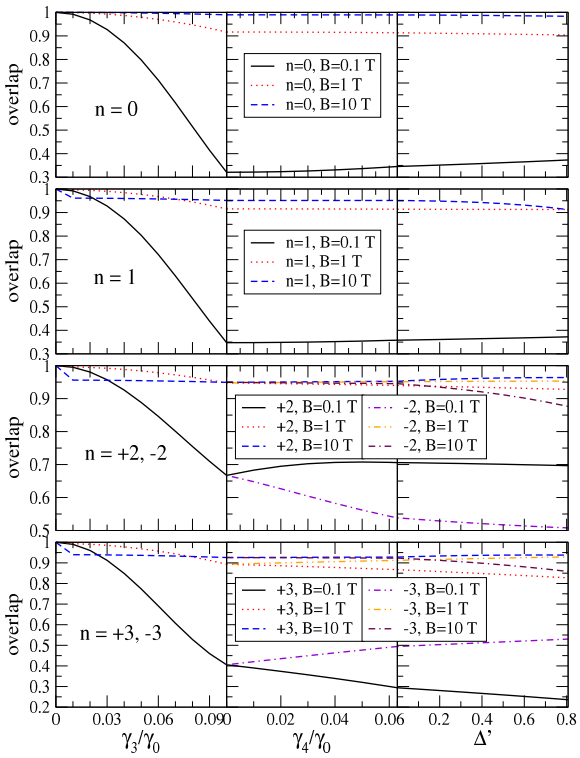

Figure 2.9: The overlap of the Landau orbitals with the *ideal* limit, $\gamma_3 = \gamma_4 = \Delta' = 0$, as the SWM parameters $\gamma_3, \gamma_4, \Delta'$ are gradually tuned from zero to their literary values for the lowest-energy LLs.

With $\pi = \frac{\sqrt{2}\hbar}{il}a$, $[a, a^\dagger] = 1$, the Hamiltonian can be expressed in terms of these LL ladder operators. Then the eigenstates of $\hat{H}_{\mathrm{B}}^{\xi}$ can be calculated numerically. Fig. 2.9 shows the overlap of the Landau orbitals with the *ideal* limit $\gamma_3 = \gamma_4 = \Delta' = 0$ as the SWM parameters $\gamma_3, \gamma_4, \Delta'$ are tuned from zero to their literary values given previously for the central $(n = 0, 1)$ and the two pairs of nearby $(n = \pm 2, \pm 3)$ LLs. At small magnetic field $B = 0.1$T trigonal warping alone significantly changes the orbitals from their ideal limit. Switching on γ_4 hardly affects the central levels, but for $n \geq 2$ it changes the electron and hole pairs $(+n, -n)$ differently, as expected from this electron-hole symmetry breaking term. Finally, the inclusion of Δ' hardly affects the

orbitals. These changes, however, are already small at modest fields ($B = 1\mathrm{T}$), and are further suppressed as the experimentally relevant range ($B \approx 10\mathrm{T}$) is approached. Thus neglecting the $\gamma_3, \gamma_4, \Delta'$ SWM parameters is justified in the high magnetic field range where quantum Hall experiments are typically performed.

As the two-band model in Eq. 2.25 applies for small momenta, and the low-index Landau orbitals have a small amplitude at high momenta, the two-band model is expected to be valid for the lowest few LLs. The Landau orbitals of the two-band model have a large overlap with those of the four-band model in the *ideal* limit $\gamma_3 = \gamma_4 = \Delta' = 0$: 1, 0.9995, 0.9992, 0.9987 for $n = 0, 1, \pm 2, \pm 3$, respectively. We conclude that using the Landau states of two-band model in Eq. 2.25 instead of those of the four-band model $\hat{H}_\xi$ in the lowest-energy Landau bands does not introduce further inaccuracy beyond the neglect of γ_3, γ_4, and Δ'. Therefore, we take $\hat{H}^{\xi}_{\mathrm{B,\,eff.}}$ as our starting point for the analysis of Chap. 5.

Finally, we note that our knowledge of bilayer graphene has gone beyond the single-particle picture, the effect of electron-electron interaction is the scope of today's investigations. This is necessitated by several experimental findings, for instance Henriksen *et al.* in [62] have found that fitting the single-body parameters does not fully explain the observed cyclotron resonance; Deacon *et al.* in [37] and Zou *et al.* in [186] have found a significant particle-hole asymmetry, whose origin is however still debated, see [146]. Other aspects are discussed in excellent reviews [11] and [86] on the topic. We postpone further discussion of the many-body effects in bilayer graphene to Chap. 5, where some of the aspects of the field will be under scrutiny. With the view of the fourfold degenerate LLs and a peculiar eightfold degenerate central Landau band, we are especially concerned with the question how the LL degeneracy is lifted by electron-electron interactions. This naturally leads us to the appearance of symmetry breaking quantum Hall ferromagnetic (QHF) states. The observation of these broken symmetry states at integer filling factors is the center of discussion in Chap. 5, where we discuss both theoretical predictions and experimental findings.

2.4 Organic Quasi-Two-Dimensional Materials - the α-(BEDT-TTF)$_2$I$_3$

2.4.1 Material Properties and Zero-Gap State in α-(BEDT-TTF)$_2$I$_3$

During the last decade the layered organic conductor aI3 has probably been the most intensively investigated member of the (BEDT-TTF)$_2$I$_3$ family. This organic compound was first synthesized in the 80's, see [13], and ever since it has been in the scope of general interest due to its surprisingly rich phase diagram. For reviews, see [118], [160] and [161]. The crystal consists of conductive BEDT-TTF [where BEDT-TTF stands for bis(ethylene-dithio)tetrathiafulvalene] layers which are separated by insulating I_3^- layers. As the layers are weakly coupled to each other, the material has a quasi-2D character, confirmed in ab initio calculations in Ref. [67]. Fig. 2.10(a) shows a BEDT-TTF molecule, while panel (b) shows how the molecules are arranged in the unit cell of the conductive BEDT-TTF layer.

One of the most striking feature of the material is the appearance of Dirac cones in the low-energy band structure under hydrostatic pressure above 15 kbar or under uniaxial strain above 3 kbar, see [157], [158] and [162]. Here we will first review the experimental findings that confirm the existence of Dirac cones, then give a short summary on the available theoretical works.

Most importantly, transport measurements are available for this material, demonstrating that the conductivity parallel to the layers is constant from room temperature down to 2K, while both the carrier density and the mobility changes several orders of magnitude in opposite directions. This behaviour was partially documented in early measurements, see [71], and later elaborated in Refs. [157], [158] and [160]. The interpretation of these findings in terms of the zero-gap state was proposed in several theoretical works, [74], [82].

Another class of experiments considers interlayer magnetoresistance, which decreases with increasing perpendicular magnetic field, and shows a complex behaviour with the angle between the magnetic field and the sample, see Refs. [144] and [162].

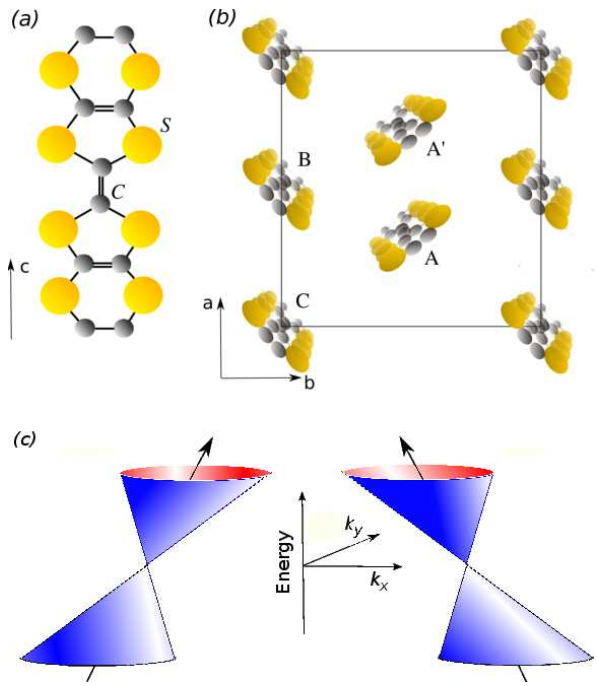

Figure 2.10: Organic compound aI3. (a) Molecule (BEDT-TTF) that consists of carbon (C) and sulfur (S) atoms. (b) Arrangement of the four molecules (A, A', B, and C) in the unit cell of a single layer (ab-plane). (c) Sketch of the low-energy band structure in the vicinity of the Fermi level that has the form of two tilted Dirac cones. The cones are tilted in the k_x direction.

These experimental results are nicely explained in related theoretical studies of the resistivity tensor components within the Dirac cone picture, see [115], [126] and [127]. The interlayer magnetoresistance measurements made it possible to directly observe the $\sqrt{B}$ behaviour of the LL spectrum, see [156].

Finally, the observation of Shubnikov-de Haas (SdH) oscillations and IQH plateaus are reported in Ref. [163]. The idea of Tajima *et al.* is to fix the aI3 crystal to a substrate in such a manner that makes a few of the BEDT-TTF layers close to the substrate significantly hole doped. In the experimental realization the extent of doping decreased rapidly with distance from the substrate, which made only two layers effectively doped. Both of these differently doped layers contributed independently to the transport, giving rise to the observed SdH oscillations and QH plateaus.[11]

[11]Note however, that this interpretation is not the only possible one. Instead of interpreting the two characteristic frequencies of the SdH oscillations in terms of the two differently doped layers, one can also speculate that different carriers, e.g. massive and massless ones might lead to the observed peculiar SdH oscillations and QH pattern. Our efforts to give such a consistent interpretation were not fruitful, as the number of observed plateaus and SdH oscillation maxima is not enough to draw a

Theoretical works in the field also include ab initio calculations, e.g. in Refs. [3], [81], which confirmed the presence of massless fermions in the material. Besides, extended Hubbard model calculations were developed by several authors, see [65], [74], [75], [76] and [82], as well as tight-binding model calculations appeared concerning aI3 and related layered organic compounds, see [112], [113], [114]. According to theory Dirac points may occur at ambient pressure above the metal to insulator transition, however hydrostatic pressure or strain suppresses the phase transition to lower temperature and stabilize the Dirac points. At even higher pressure or strain the Dirac points coalesce at a high-symmetry Γ point of the Brillouin zone where a gap opens, see [109], [110]. As was discussed by Mori in Ref. [113], the Dirac points appear at low-symmetry, time-reversal related points, with non-stripe charge order.

To conclude this section, we have shown through various experiments and theoretical works that at high pressure or high strain massless Dirac fermions occur in aI3. In the next subsections we highlight the differences of the Dirac cone in this organic compound with respect to graphene and also discuss the open questions about the low-energy band structure of the material.

2.4.2 Tight-Binding Description of the Conical Bands

aI3 is a 3D crystal with triclinic crystal structure, containing conducting BEDT-TTF and insulating I_3^- anion layers. As confirmed by theory, see Ref. [67], this crystal has a strong 2D nature with negligible interlayer coupling, therefore it is customary to regard each conducting layer independently as a 2D crystal and develop a 2D model accordingly. The unit cell of the 2D model is oblique, with the primitive vectors enclosing an angle $\gamma \approx 90.8°$. The length of the primitive vectors change monotonically from $a \approx 9.1$ Å and $b \approx 10.8$ Å to $a \approx 8.6$ Å and $b \approx 10.35$ Å as the pressure is increased from ambient pressure to 17.6 kbar, see [84]. Fig. 2.11(a) shows a sketch of the unit cell containing four BEDT-TTF molecules, and panel (b) shows the first Brillouin zone with the distinguished points and directions we refer to later.

The low-energy band structure can be derived from a tight-binding model that involves the four relevant highest occupied molecular orbitals of the BEDT-TTF molecules

conclusive picture. More precise measurement is needed before far-reaching conclusions are drawn.

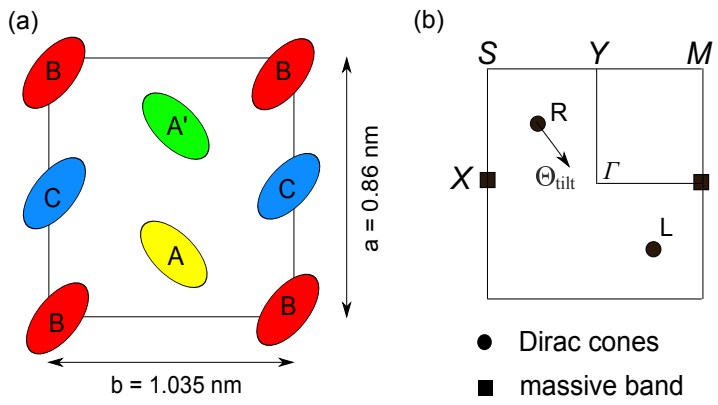

Figure 2.11: Schematic view of the unit cell (panel (a)) and the first Brillouin zone of aI3 (panel (b)). The high-symmetry points, the location of the massive valley (squares), and that of the Dirac cones (dots) are indicated. The arrow from point R indicates the smallest steepness of cone R. Directions in the momentum plane will be related to this angle, $\theta_{\rm tilt}$.

in the unit cell, see Refs. [53], [82]. Among the four bands, only the upper two play a role as the filling is 3/4 at charge neutrality [112]. These two bands have contact points at low-symmetry, time-reversal related points L and R, the conical bands are anisotropic and tilted [81]. The massless Dirac carriers are suitably described by the minimal Weyl Hamiltonian using four velocity parameters v_0^x, v_0^y, v_x and v_y as

$$\hat{H}_{\rm W}^{\xi}(\mathbf{q}) = \xi\hbar[(v_0^x q_x + v_0^y q_y)\sigma_0 + v_x q_x \sigma_x + \xi v_y q_y \sigma_y] \tag{2.28}$$

where $\xi = 1$ ($\xi = -1$) represents the cone at R (L), and $\mathbf{q}$ is measured from the Dirac point R or L. This Hamiltonian obviously respects time-reversal symmetry, $\hat{H}_{\rm W}^{\xi=1}(\mathbf{q}) = [\hat{H}_{\rm W}^{\xi=-1}(-\mathbf{q})]^*$. It has spin-degenerate bands, but the dispersions in valleys $\xi = \pm 1$ differ. The inclination of the Dirac cone is determined by the combined effect of the tilt and the anisotropy. By the *anisotropy* of the Dirac cone we mean the difference between v_x and v_y, and we characterize it by the parameter

$$\alpha = \sqrt{v_x/v_y}. \tag{2.29}$$

By its *tilt* we mean that the constant energy slices are not concentric because $(v_0^x, v_0^y) \neq (0,0)$. For convenience, we will also use a rescaled and rotated coordinate system

similarly to Ref. [115] defined by the transformation

$$\left.\begin{aligned} \tilde{q}_x &= q_x \cos\theta + \tfrac{q_y}{\alpha^2}\sin\theta \\ \tilde{q}_y &= -q_x \sin\theta + \tfrac{q_y}{\alpha^2}\cos\theta \end{aligned}\right\}. \tag{2.30}$$

The corresponding transformed real-space coordinates $\tilde{\mathbf{r}} = (\tilde{x}, \tilde{y})$ are

$$\left.\begin{aligned} \tilde{x} &= x\cos\theta + \alpha^2 y \sin\theta \\ \tilde{y} &= -x\sin\theta + \alpha^2 y\cos\theta \end{aligned}\right\}. \tag{2.31}$$

Rescaling the q_y coordinate removes the anisotropy. The rotation brings the $\tilde{q}_x$ coordinate in the tilt direction if we choose

$$\cos\theta = \cos\theta_{\text{tilt}} \equiv \frac{v_0^x v_y}{\sqrt{(v_0^y v_x)^2 + (v_0^x v_y)^2}}. \tag{2.32}$$

After some straightforward algebra and a unitary transformation, see [115], the Weyl Hamiltonian can be written as

$$\hat{H}_{\text{W}}^{\xi}(\tilde{\mathbf{q}}) = \xi\hbar v_x[\beta\tilde{q}_x\sigma_0 + \tilde{q}_x\sigma_x + \xi\tilde{q}_y\sigma_y], \tag{2.33}$$

where we have introduced the dimensionless parameters

$$\beta = \sqrt{(v_0^x/v_x)^2 + (v_0^y/v_y)^2} \quad \text{and} \quad \lambda = \sqrt{1-\beta^2} \tag{2.34}$$

to quantify the tilt. Notice that $0 \leq \beta \leq 1$, and that $\beta = 0$ corresponds to the case of graphene. In the following we will work in the coordinate system introduced in Eq. 2.30 for computational simplicity, however, we formulate our main results in the original coordinate system. Fig. 2.10(c) depicts the oppositly tilted Dirac cones.[12]

An open issue concerning the low-energy band structure of this crystal is the determination of the parameters β, α and θ_{tilt} describing the Dirac cones. Note that our knowledge of the geometry of the cones comes from theory, as the available, mainly

[12]Even though in this subsection we have not considered magnetic field, we note for further reference that the magnetic length gets also rescaled due to the change of coordinates. The rescaled magnetic length is $\tilde{l} = \alpha l$.

transport, measurements are insensitive to the inclination or the anisotropy of the cones. In the literature several sets of parameters are available, see [75], [82], and their pressure dependence is also analyzed in detail, see Ref. [65]. Motivated by these considerations, in Chap. 3 we present an analysis of the magneto-optical selection rules in this material, which might lead to an experimental indication for at least some of the parameter values. In Chap. 4, however, to illustrate the collective plasmon excitations in the system, we choose a representative set of parameters based on [82]. We emphasize that our results are robust and survive within a broad range of the parameter values.

Another open question of the low-energy band structure is that in addition to the linear valleys, there may be a band maximum at the time-reversal symmetric point X on the edge of the first Brillouin zone, which may host massive holes. The existence of a parabolic valley besides the linear ones is proposed by a recent ab initio calculation in Ref. [3] and experimentally verified by Monteverde *et al.* in Ref. [111]. In his article, Monteverde conducted magnetotransport experiments, identified both massive and massless carriers and deduced several quantities of interest, e.g. carrier densities for both types of carriers, the effective Fermi velocity of the massless carriers and the effective mass for the massive ones. Note, however, that his findings are not verified by additional transport measurements yet, thus we believe it is a timely issue to discuss such properties of the electron system in this material which in principle probe the existence of both carrier types. This leads us to the central idea of the *three-valley model* discussed in Chap. 4.

2.4.3 Relativistic Covariance in α-(BEDT-TTF)$_2$I$_3$

In this subsection we derive the LL eigenstates and eigenfunctions of aI3 in a perpendicular magnetic field. This problem may be solved by an algebraic method presented in Ref. [115], nevertheless we utilize the relativistic covariance of the underlying Dirac equation similarly to Sec. 2.2.4. We draw a parallel between graphene in a crossed electric and magnetic fields and aI3 in a magnetic field, in the latter case the tilt plays a role essentially identical to that of the electric field in graphene. The same line of reasoning can be applied to any system with tilted Dirac cones, e.g. to the conical

valleys realized on the surface of 3D topological insulators in a crossed electric and magnetic field, see Ref. [172]. There again, the LL eigenstates and eigenfunctions can be computed in complete analogy.

Consider the Hamiltonian in Eq. 2.33 in a perpendicular magnetic field with vector potential $\mathbf{A} = (-yB, 0, 0)$.[13] The Schrödinger equation of the Hamiltonian Eq. 2.33 with the covariant notation introduced previously becomes

$$-i\hbar v_x \gamma_\mu (\partial^\mu - \frac{ie}{\hbar} A^\mu)\Phi(x,y) + i\hbar v_x \gamma_0 \beta \partial^x \Phi(x,y) = 0 \tag{2.35}$$

with $A^\mu = (\beta By, -yB, 0)$.

One can make the last term containing the derivative harmless by writing the ansatz for the wave function $\Phi(x,y) = e^{ikx}\psi(y)$. With this the Dirac equation becomes

$$-i\hbar v_x \gamma_\mu (\partial^\mu - \frac{ie}{\hbar} A^\mu)\Phi(x,y) + \gamma_0 \hbar v_x \beta k \Phi(x,y) = 0. \tag{2.36}$$

Comparing this Dirac equation with that of the graphene system in Eq. 2.14, we find the two equations are identical, if we equate the tilt parameter β of the Weyl system with $\beta = E_\parallel / v_F B$ describing the quotient of the drift and Fermi velocity in graphene. Note that precisely this correspondence made it possible to denote these two quantities different in nature with the same symbol. Hereafter, we use β to refer to the tilt parameter in the context of the Weyl Hamiltonian, while β is also the appropriate parameter in the context of graphene, which describes the electric field. One may also rephrase the correspondence in terms of an effective electric field. The tilt in the Weyl systems may be interpreted as an effective electric field $E_\parallel^{\text{eff}} = \beta v_x B$, where $E_\parallel^{\text{eff}}$ plays the same role as $E_\parallel$ in graphene.

The eigenfunctions and eigenvalues of the Dirac equation in Eq. 2.36 is easily recovered with exactly the same machinery as was discussed for graphene. The wave function of this Dirac equation in the frame R is identical with that of graphene with an in-plane electric field. The eigenvalue spectrum is modified by the last term of Eq.

[13] Note that here we are working in the rotated, rescaled coordinates $\tilde{\mathbf{r}}$ introduced in Eq. 2.31 for computational simplicity. Similarly, the magnetic field B is also considered in the new coordinates. Apparently, the use of $\tilde{B} = B/\alpha^2$ would be more consistent. We have omitted the ˜ sign for simplifying notations.

2.36, which is finally[14]

$$\epsilon_n^{\mathrm{W}} = \mathrm{sgn}(n)\sqrt{2|n|}\frac{\hbar\sqrt{v_x v_y}}{l}\lambda^{3/2}. \tag{2.37}$$

Comparing the latter equation with Eq. 2.16, it is evident that $\sqrt{v_x v_y}$ plays the role of graphene's Fermi velocity v_F, and the dependence of Eq. 2.37 on the magnetic field B and LL index n is identical to that of Fig. 2.4.

In principle, the same derivation can be applied to cone $\xi = -1$ to recover its proper eigenfunctions. Note, however, that while in graphene the electric field does not change sign in the two cones, in aI3 the tilt is opposite in the two valleys. Therefore the eigenfunctions are not identical in the second valley in graphene, and in the Weyl system. To follow closely the above line of derivation, we need to change the sign of the effective electric field, which does not correspond to a physical situation in graphene. For further reference the eigenfunctions for both cones are reproduced in App. B.

2.4.4 Massless Fermions in Related Zero-Gap Organic Compounds

In the previous subsections we have investigated in detail the organic compound aI3 and its particular high-pressure phase in which Dirac fermions occur. The existence of Dirac electrons is verified by numerous experiments hand in hand with the detailed theoretical investigations. Indeed, aI3 is the best established example among the layered organic crystals that host Dirac electrons. The quest for Dirac cones in similar organic compounds has naturally set off. Several theoretical investigations appeared, though the experimental data concerning related organic crystals is still very limited.

^{13}C NMR experiments and transport measurements with $\theta-$(BEDT-TTF)$_2$I$_3$ provided evidence for the existence of Dirac femions in the material, see [108] and [159], though there might be a tiny gap, see [159]. Theoretical investigations are mostly based on tight-binding analysis. In [113] and [114] Mori presented a systematic investigation of two, three and four-molecule compounds, he deduced analytic conditions to the appearance of the zero-gap state and the contact point (in which case the apex of

[14] We present the eigenvalue spectrum and the eigenfunctions (see App. B) in the original coordinates $\mathbf{r}$, where we have incoorporated the effect of the rescaled magnetic length.

the Dirac cone does not coincide with the Fermi energy) and identified several other potential massless Dirac materials among layered organic conductors. One promising candidate was the four-molecule crystal α-(BEDT-TTF)$_2$KHg(SCN)$_4$, though further investigations revealed that the apex of cones is well below the Fermi energy, only a contact point appears. Other theoretical works proposed α-(BEDT-TTF)$_2$NH$_4$Hg(SCN)$_4$ to have a zero-gap state, here the Dirac cones are predicted to be isotropic, see [30]. Undoubtedly, these proposals require experimental confirmation.

In the following we will refer to the compounds that might host Dirac electrons as *2D Weyl materials*, as their electronic behaviour can be described in a similar manner by the generalized Weyl equation, see [53], [115]. As a particular example, however, we always keep aI3 in mind. Our predictions presented in Chaps. 3 and 4 may be equally valid for any of these compounds with tilted, anisotropic Dirac cones, as there we only rely upon these facts.

Chapter 3

Magneto-Optical Properties within the Single-Particle Picture

3.1 Introduction

In the previous chapter we reviewed the basic properties of those 2D materials that are under scrutiny in the present thesis. In this chapter we are focusing on two of them: monolayer graphene in a perpendicular magnetic and a crossed electric field, and Weyl materials in a perpendicular magnetic field. We have shown previously that the in-plane electric field in graphene and the tilt in the Weyl materials play a similar role, leading to identical LL eigenfunctions. We have introduced the same notation for the tilt parameter and for the parameter describing the in-plane electric field, reflecting their common role. Here we build up a unified model of the magneto-optical properties of these systems, however, when necessary we point out their differences. Note that β is a tunable parameter for graphene, in that case experimental verification of the following results might become possible. For the Weyl materials β is a built-in material property, which we take as a constant. With this in mind we develop an experimental procedure by which the determination of this and related material parameters may become possible.

The appearance of the LLs in graphene in zero electric field have been extensively studied. Besides the usual QH measurements presented in Chap. 2, several magneto-optical measurements are available. In Ref. [143] Sadowski *et al.* performed

far infrared transmission experiments on ultrathin epitaxial graphite samples. Using unpolarized light they identified several LL transitions as a function of the magnetic field, and found excellent agreement with the predictions of the single-particle picture discussed in Chap. 2. For right or left circular polarization a selection rule applies, making only $\delta_{|n|,|n'|\pm 1}$ LL transitions available, where $n \to n'$ are the two LLs involved. Later, in Refs. [63] and [70] similar infrared magnetospectroscopy measurements were conducted, however, they found some indications of many-body effects in monolayer graphene.

In Ref. [2] Abergel *et al.* calculated the absorption coefficient, which turns out to have a universal value $\pi\alpha \approx 2.3$ %, where α is the fine structure constant. Experimental verification of the above value is given in [119] by Nair *et al.*, who deduced it from the measurement of transmittance. These results are confirmed both theoretically and experimentally by [18], [91] and [98].

Our aim here is to determine the absorption coefficient both for graphene in a magnetic and an in-plane electric field and for Weyl materials in a magnetic field. For this we apply a single-particle picture. As was seen in the literature, the many-body effects renormalize the LL spectrum to such a small extent that we believe the single-particle picture gives a good first approximation. Moreover, we handle the incoming radiation within a classical picture. With these assumptions we present a simple derivation of the absorption coefficient, which, nevertheless, gives us a surprisingly rich physics. The possible experiments are discussed at the end of the chapter.

3.2 Derivation of the Dimensionless Absorption Coefficient

To derive the dimensionless absorption coefficient $i_{\text{abs}}(\omega)$ for arbitrary polarization we follow Ref. [180], note that a similar derivation is presented by Booshehri *et al.* in [21] for circular polarization. In this chapter we derive i_{abs} for cone $\xi = 1$. One can check by direct calculation that both cones give the same contribution to the absorption coefficient, therefore we take the valley and the spin degeneracy into account by a factor of 4.

For simplicity we handle the incoming electromagnetic field classically. We use Coulomb gauge in SI units, then the radiation field is

$$\mathbf{A}^{\mathrm{rad}}(\mathbf{r},t) = \frac{|E_0|}{\omega}(\kappa\hat{\mathbf{e}}_x + \tau\hat{\mathbf{e}}_y)e^{i\omega t} + h.c. \tag{3.1}$$

where ω is fixed, $|E_0|$ is an ω independent constant, and we have taken the $z = 0$ plane. The parameters κ and τ determine the light polarization in a way that $|\kappa|^2 + |\tau|^2 = 1$, and $\hat{\mathbf{e}}_{x/y}$ are unit vectors. For right ($\circlearrowright$) / left ($\circlearrowleft$) circularly polarized light the parameters κ and τ are $\kappa = 1/\sqrt{2}$ and $\tau = \mp i/\sqrt{2}$, for linear polarization $\kappa = \cos\theta$ and $\tau = \sin\theta$, where the linearly polarized light has its own parameter θ.[1] For the Weyl materials the rescaled, rotated $\tilde{\kappa}, \tilde{\tau}$ should be applied.[2]

We take the effect of the radiation field $\mathbf{A}^{\mathrm{rad}}$ into account through minimal coupling, that is we replace $\mathbf{A}$ of Eq. 2.13 (graphene) and of Eq. 2.33 (Weyl materials) by $\mathbf{A} + \mathbf{A}^{\mathrm{rad}}$. As the dispersion relation of these systems is linear, one can separate the non-perturbative and the perturbative Hamiltonians without further approximations, as opposed to conventional 2DEG. The perturbative Hamiltonians describing the radiation field become

$$^{\mathrm{E}_\parallel}\delta H = ev_F\frac{|E_0|}{\omega}(\kappa\sigma_x + \tau\sigma_y), \tag{3.2}$$

$$^{\mathrm{W}}\delta H = ev_x\frac{|E_0|}{\omega}(\tilde{\kappa}\sigma_x + \tilde{\tau}\sigma_y + \beta\tilde{\kappa}\sigma_0). \tag{3.3}$$

With the view of applying Fermi's Golden Rule, first we compute the matrix element:

$$^{\mathrm{E}_\parallel}\delta H^{n',k'}_{n,k} = \int \mathrm{d}\mathbf{r}[\Phi^{\xi=1}_{n,k}(\mathbf{r})]^\dagger \cdot {}^{\mathrm{E}_\parallel}\delta H \cdot \Phi^{\xi=1}_{n',k'}(\mathbf{r}) = ev_F\frac{|E_0|}{\omega}\delta(k-k')\ {}^{\mathrm{E}_\parallel}Q^{n'}_n, \tag{3.4}$$

$$^{\mathrm{W}}\delta H^{n',k'}_{n,k} = \int \mathrm{d}\mathbf{r}[\Phi^{\xi=1}_{n,k}(\mathbf{r})]^\dagger \cdot {}^{\mathrm{W}}\delta H \cdot \Phi^{\xi=1}_{n',k'}(\mathbf{r}) = e\sqrt{v_x v_y}\frac{|E_0|}{\omega}\delta(k-k')\ {}^{\mathrm{W}}Q^{n'}_n, \tag{3.5}$$

where we used the spinorial wave functions $\Phi^{\xi=1}_{n,k}(\mathbf{r})$ of Eq. 2.17 and $\delta(x)$ is the Dirac

[1] In addition to θ, the elliptically polarized light has another parameter ϕ. Then $\kappa = \cos\theta$ and $\tau = e^{i\phi}\sin\theta$.

[2] Here the same transformation rule applies as for the momentum $\mathbf{q}$ in Eq. 2.30: $\tilde{\kappa} = \kappa\cos\theta_{\mathrm{tilt}} + \tau\sin\theta_{\mathrm{tilt}}/\alpha^2$ and $\tilde{\tau} = -\kappa\sin\theta_{\mathrm{tilt}} + \tau\cos\theta_{\mathrm{tilt}}/\alpha^2$.

delta function. $Q_{n'}^{n}$ denotes the dimensionless part of the matrix element

$$
\begin{aligned}
{}^{\mathrm{E}_\parallel}Q_n^{n'} &= -\frac{1}{2}\Big[F_{|n|,|n'|}^{n,n'}\kappa\beta + \mathrm{sgn}(n)\mathrm{sgn}(n')F_{|n-1|,|n'-1|}^{n,n'}\kappa\beta \\
&\qquad + \mathrm{sgn}(n')F_{|n|,|n'-1|}^{n,n'}(\kappa + i\tau\lambda) + \mathrm{sgn}(n)F_{|n-1|,|n'|}^{n,n'}(\kappa - i\tau\lambda)\Big], \qquad (3.6)\\
{}^{\mathrm{W}}Q_n^{n'} &= \frac{\lambda}{2}\Big[\mathrm{sgn}(n')F_{|n|,|n'-1|}^{n,n'}(\lambda\tilde{\kappa} - i\tilde{\tau}) + \mathrm{sgn}(n)F_{|n-1|,|n'|}^{n,n'}(\lambda\tilde{\kappa} + i\tilde{\tau})\Big]. \qquad (3.7)
\end{aligned}
$$

The function $F_{|n|,|n'|}^{n,n'}$ is defined in App. C.

Next we calculate the transition rate per unit area A using Fermi's Golden Rule and taking notice of the occupancy of the initial and final states. Then

$$
R_{n,k\to n',k'}^{\mathrm{emi/abs}} = \frac{1}{A}\frac{2\pi}{\hbar}\left|\delta H_{n',k'}^{n,k}\right|^2 \delta(\epsilon_{n'} - \epsilon_n \pm \hbar\omega) f_0(\epsilon_n)(1 - f_0(\epsilon_{n'})), \qquad (3.8)
$$

where $f_0(\epsilon)$ is the Fermi function.[3] $R_{n,k\to n',k'}^{\mathrm{emi/abs}}$ represents the emission/absorption processes. The total transition rate is obtained by integrating over the available k states and summing over the filled (n) and empty (n') LLs

$$
R = \sum_{n,n'}\int \mathrm{d}k \int \mathrm{d}k' \left[R_{n,k\to n',k'}^{\mathrm{abs}} - R_{n',k'\to n,k}^{\mathrm{emi}}\right]. \qquad (3.9)
$$

The dimensionless magneto-absorption coefficient is given by

$$
i_{\mathrm{abs}}^{\mathrm{W/G}}(\omega) = \frac{R\hbar\omega}{S}, \qquad (3.10)
$$

where $S = |E_0|^2/2\mu_0 c$ is the magnitude of the time averaged Poynting vector, and μ_0 is the vacuum permeability. As an approximation we take the $T \to 0$ limit. Furthermore, we introduce a Lorentzian broadening Γ for neglected effects (impurities, phonons, etc). Then one finds

$$
\begin{aligned}
i_{\mathrm{abs}}^{\mathrm{W/E}_\parallel}(\omega) &= \frac{2v^2\hbar\mu_0 c e^2}{l^2}\sum_{n,n'}\frac{1}{\epsilon_{n'} - \epsilon_n}\left|{}^{\mathrm{W/E}_\parallel}Q_n^{n'}\right|^2 \delta(\epsilon_{n'} - \epsilon_n - \hbar\omega) \\
&= \frac{2v^2\hbar\mu_0 c e^2}{l^2}\sum_{n,n'}\frac{1}{\epsilon_{n'} - \epsilon_n}\left|{}^{\mathrm{W/E}_\parallel}Q_n^{n'}\right|^2 \frac{1}{\pi}\frac{\Gamma}{\Gamma^2 + (\epsilon_{n'} - \epsilon_n - \hbar\omega)^2}. \qquad (3.11)
\end{aligned}
$$

[3]Note that to get a dimensionless absorption coefficient for a 3D material, one shall compute the transition rate per unit volume V.

Here and hereafter we use the notation v both for the Fermi velocity v_F of graphene and for the *Fermi velocity* $\sqrt{v_x v_y}$ of aI3. Also, we estimated $\Gamma = 0.002$eV on the basis of Ref. [143] and use this value as a constant broadening.

3.3 Results and Discussion

3.3.1 The Dimensionless Matrix Element

With the view of calculating the absorption coefficient we find it illuminating to examine the modulus square of the dimensionless matrix element $\left|{}^{\mathrm{E}_\parallel/\mathrm{W}}Q_n^{n'}\right|^2$. It corre-

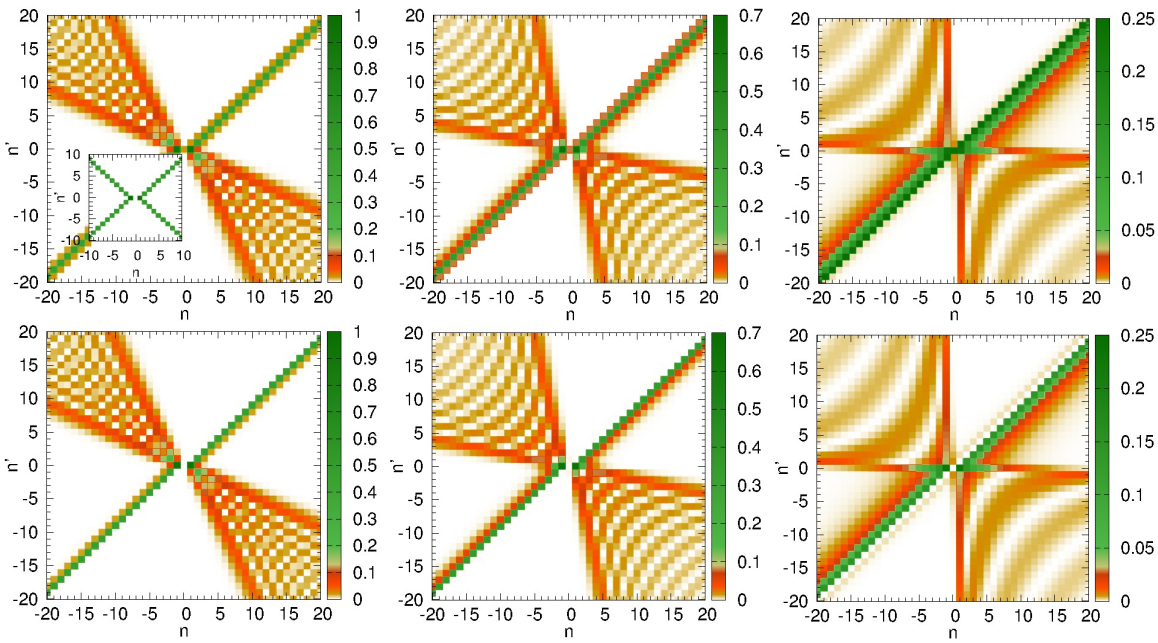

Figure 3.1: In the first row dimensionless matrix elements $\left|{}^{\mathrm{E}_\parallel}Q_n^{n'}\right|^2$ of graphene corresponding to $n \to n'$ transitions are depicted for $\beta = 0.2, 0.4, 0.7$, respectively. Here right circularly polarized light is considered. The inset shows the $\beta = 0$ case. In the second row $\left|{}^{\mathrm{W}}Q_n^{n'}\right|^2$ is shown, for the same β parameters, but for such an elliptically polarized light that appears right circularly polarized in the rotated, rescaled system.

sponds to a fixed $n \to n'$ LL transition, for which a particularly severe selection rule applies in the $\beta = 0$ ($E_\parallel = 0$) limit: under right/left circular polarization only the matrix elements satisfying $\left|Q_n^{n'}\right|^2 \propto \delta_{|n|,|n'|\pm 1}$ are non-zero. In this chapter we are interested in whether the electric field or the tilt induce additional transitions and analyze

their structure, if they appear.

Fig. 3.1 shows the modulus square of the matrix elements for both systems under consideration for various β values under right circular polarization. Here we only consider right circular polarization, as the identity $\left|{}^{\circlearrowright}Q^{\mathrm{sgn}(n')|n'|}_{\mathrm{sgn}(n)|n|}\right|^2 = \left|{}^{\circlearrowleft}Q^{\mathrm{sgn}(n')|n|}_{\mathrm{sgn}(n)|n'|}\right|^2$ holds for the right and left circular polarizations. For direct comparison with graphene we apply such an elliptically polarized light to the Weyl materials that appears to be right circularly polarized after the rotation and rescale. The results of the two systems are essentially identical, nevertheless, there are some minor differences, e.g. the matrix elements along the antidiagonal ultimately vanish for the Weyl materials for all polarizations, whereas they are proportional to β^2 for graphene under circularly polarized light. We will see that these differences between the two material systems are marginal in the following analysis of the absorption coefficient, therefore we may examine the two systems together.

As it is visible in Fig. 3.1, we obtain novel transitions beyond the usual dipolar ones (see inset in Fig. 3.1). The intraband matrix elements that change the LL index n by more than one unit become non-zero, their weight grows with β. More saliently, the interband transitions show a complex *fan* structure whose opening angle increases with β, and it displays a noticable arc pattern. The fan itself is bounded by large values of the perturbation matrix elements that are not affected by the arc pattern, the arc itself is visible in the middle of the fan, it becomes wider with increasing β.

To understand the origin of the remarkable arc pattern, let us consider a bunch of the matrix elements, namely those along the main diagonal, which correspond to transitions $-n \to n$, see Fig. 3.2 and the explanation therein. These matrix elements may be computed analytically, leading to a simple form for both material systems under circular polarization (or elliptical polarization that appears as circular in the rotated, rescaled coordinates):

$$Q_n^{-n} \propto (\beta^2 - 1)\beta e^{-2n\beta^2} L^1_{n-1}(4\beta^2 n), \tag{3.12}$$

where $L^m_n(x)$ is the associated Laguerre polynomial. For the sake of the argument we

take n as a continuous variable,[4] bearing in mind that physically relevant values of the function Q_n^{-n} are only those with integer n.

Let us consider the high-β limit first. The period δn of the continuous Q_n^{-n} function is more than, but close to unity. By Nyquist's sampling theorem in the $\delta n < 2$ range a beating pattern of the physically relevant points arise, with a distance Δn between the consecutive zeros much higher than unity. Indeed, a beating pattern is well-visible in panel 3.2(d). Note that this discussion deals with one particular bunch of the matrix elements only. A similar argument applies for interband transitions along straight lines

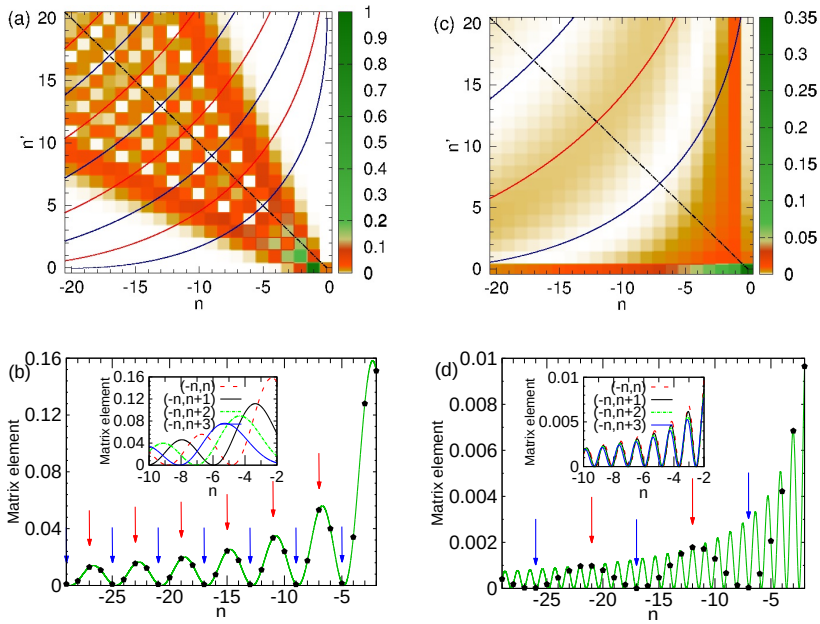

Figure 3.2: Interband matrix elements $\left|{}^{\mathrm{E}_\parallel}Q_n^{n'}\right|^2$ under circularly polarized light for $\beta = 0.2$ (panel (a)) and 0.8 (panel (c)) are reproduced. Black dotted line indicates the diagonal along which Eq. 3.12 is valid. Equienergy contours are represented as blue and red curves, whose energy is identical with the energy of the matrix elements indicated by arrows in panels below. Red curves corresponds to high, blue curves to low-energy matrix elements. Panel (b) and (d) show the matrix elements $\left|{}^{\mathrm{E}_\parallel}Q_{-n}^{n}\right|^2$ along the diagonal as a function of n for $\beta = 0.2$ and 0.8, respectively. n is taken as a continuous variable (green line). The black dots indicate the physically relevant values of the matrix elements, where n, the index of the two involved LLs, is an integer. Inset: Matrix elements along various straight lines of the (n, n') plane.

that go through the origin in the (n, n') plane, although the formulas are considerably more complicated than for the above case. These continuous functions are in phase

[4]The associated Laguerre polynomial is generalizable in terms of confluent hypergeometric function.

and have the same period as the one along the main diagonal. Thus, the arc pattern finds its origin as a beating pattern of the underlying Laguerre functions along straight lines of the (n, n') plane of the matrix elements. This also means that one single period exists to describe the arc pattern. More impressively, we also find that the constant energy contours in the plane of the matrix elements are arcs that follow the striped pattern of the interband matrix elements. This coincidence is remarkable, especially at high β values. Consequently, we anticipate the appearance of this periodic pattern in the absorption coefficient.

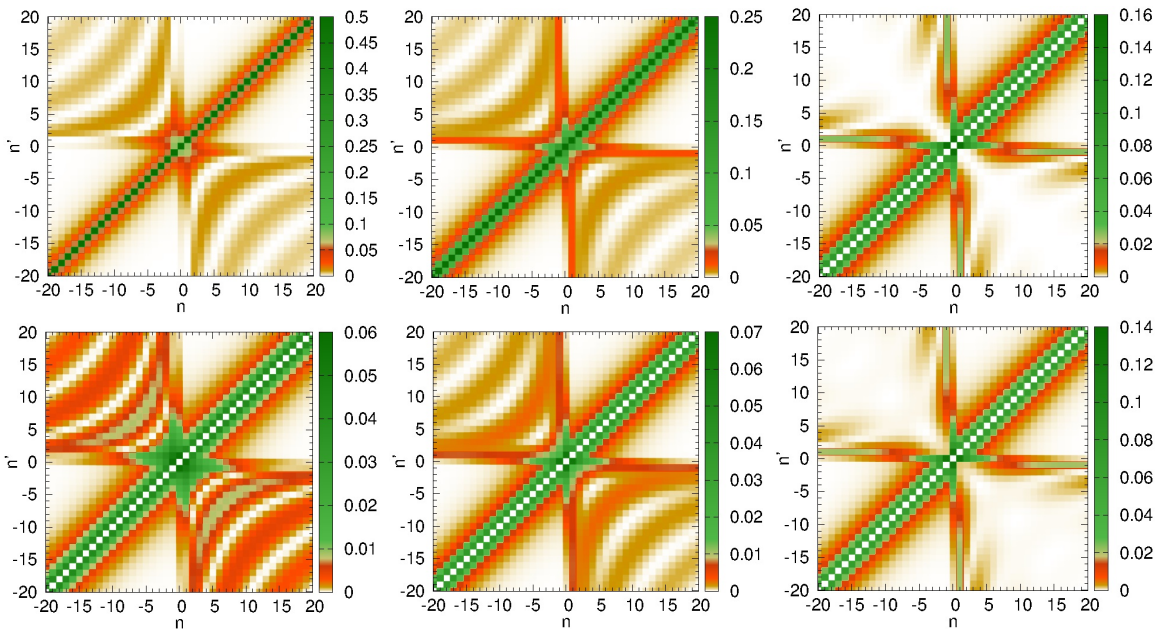

Figure 3.3: First row: Modulus square of the dimensionless matrix elements $\left|{}^{\mathrm{E}_\parallel}Q_n^{n'}\right|^2$ at fixed $\beta = 0.7$ under linearly polarized light with $\theta = 0°, 45°, 90°$, respectively. Second row: Similar results for the Weyl materials, but here the corresponding angle of the linearly polarized light is $\theta = \theta_{\mathrm{tilt}}, \theta_{\mathrm{tilt}} + 45°, \theta_{\mathrm{tilt}} + 90°$.

The above analysis is true if Nyquist's theorem is applicable, that is $\delta n < 2$, which corresponds to $\beta > 0.35$. At smaller β values, applying the same procedure we find that the equienergy contours roughly follow the arc pattern, especially in the middle of the fan, which forecasts the presence of the periodic oscillations in the absorption coefficient. By examining the matrix elements as continuous functions along various straight lines we find that they have approximately the same period, but are out-of-phase, which makes it impossible to describe the corresponding arc pattern by a single

well-defined period, see Fig. 3.2(b). As we shall see later on analyzing the absorption coefficients, two characteristic periods will appear.

So far we have considered circular polarization and have found a remarkable arc pattern with a characteristic period depending on the value of β. One may also consider linear polarization, then the matrix elements are described by β, as previously, and by the angle of the polarization θ.

Fig. 3.3 shows a strong dependence of the matrix elements on θ for a fixed value of β. Comparing these results with that of the circularly polarized case, a surprisingly new feature is that as θ approaches the direction perpendicular to the electric field or to the tilt direction, the matrix elements inside the fan vanish. As we have already forecast, and will verify in great detail in the next section, the matrix elements inside the fan are responsible for the appearance of a periodic oscillation in the absorption coefficient, we expect that the disappearance of the matrix elements at a certian angle of the polarization will cancel the observable periodic oscillation as well.[5]

3.3.2 The Absorption Coefficient

In this section we present our final results of the experimentally accessible absorption coefficient calculated in Eq. 3.11 both for graphene in a crossed electric and magnetic fields and for the Weyl materials in a magnetic field. We take the highest-filled LL $n^F = 0$ throughout the chapter. A straightforward generalization of our result for arbitrary doping is possible.

Fig. 3.4(a) shows the absorption coefficient for graphene as a function of the frequency for several values of β. While for $\beta = 0$ we get back the expected dipolar transitions satisfying the selection rules $\delta_{|n|,|n'|+1}$ for all frequency range, for $\beta \neq 0$ the lines of many newly emerging transitions coalesce resulting in a periodic oscillation of the absorption curve. This feature is especially well-pronounced in the high-frequency regime, for intermediate and large values of β. This resulting supermodulation stems

[5]In principle, using elliptically polarized light and tuning its parameters θ and ϕ, one may also deduce the anisotropy parameter $\alpha = \sqrt{v_x/v_y}$ from the θ and ϕ dependence of the intensity of low-energy transitions. However, we expect that the higher-frequency tail of the absorption spectrum remains insensitive to the polarization, see Fig. 3.4. As we are primarily interested in the high-energy behaviour of the absorption spectrum in the following, we do not examine the elliptically polarized case, leaving the investigation to future work.

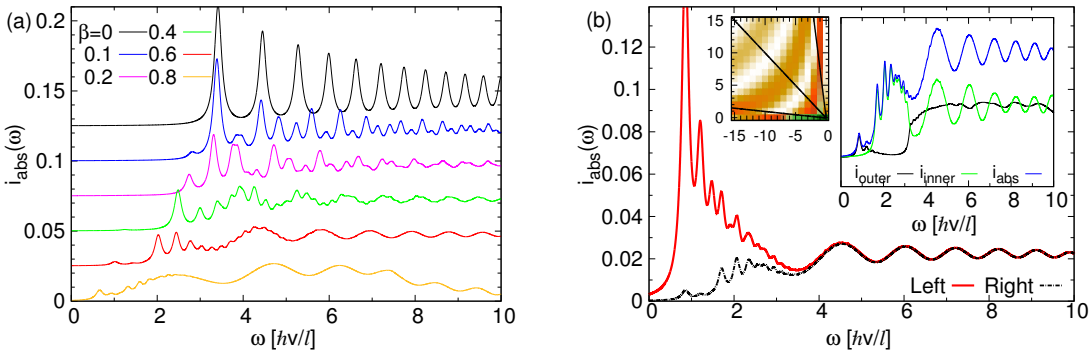

Figure 3.4: $i_{\text{abs}}^{\text{E}_\parallel}(\omega)$ is depicted for various values of β using right circularly polarized light (panel (a)). The absorption coefficient is shown for fixed $\beta = 0.7$ under left and right circularly polarized light (panel (b)). Inset of panel (b): $i_{\text{abs}}^{\text{E}_\parallel}(\omega)$ is reproduced (right circular polarization, $\beta = 0.7$) with i_{outer} and i_{inner} as explained in the text.

from the arc pattern, as the arcs connect transitions that have the same energy, see Fig. 3.2. We point out that the oscillatory behaviour of the high-frequency tail is robust and does not depend on the particular polarization. Fig. 3.4(b), which shows i_{abs} for both right and left circularly polarized light, makes it evident that only few low-frequency LL transitions depend on the light polarization, the absorption becomes polarization-independent in the large frequency range, sensitive only to the above-mentioned supermodulation. The inset of Fig. 3.4(b) examines the weight of various matrix elements to the final oscillatory behaviour of i_{abs}. We divided the matrix elements of the $(n,\ n')$ plane into two parts, one part representing the *inner* matrix elements, that give the arc pattern, while the other part contains those elements that delimit the fan, referred to as *outer* elements. As it is nicely shown in the figure the inner elements (i_{inner}) are responsible for the oscillatory behaviour, while i_{outer} only gives a featureless background. In other words, we verified the arc pattern explained in terms of the period of the underlying Laguerre function is the source of the oscillations in the absorption coefficient.

To proceed, we highlight that even though the matrix elements entering i_{abs} are a periodic function of the LL index n, the LL spectra itself scales as $\sqrt{n}$. Therefore we consider the spectra as a function of $\omega' = \omega^2$, and seek the effect of the high-frequency regular pattern in the Fourier transform $\mathcal{F}[i_{\text{abs}}(\omega')](t)$. The rescaled absorption coeffi-

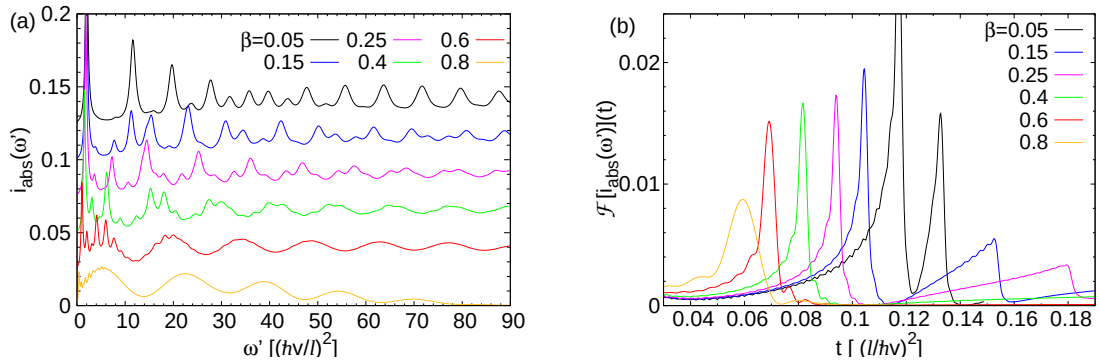

Figure 3.5: Rescaled absorption coefficient $i^{\mathrm{W}}_{\mathrm{abs}}(\omega')$ is shown in panel (a) for linearly polarized light with $\theta = \theta_{\mathrm{tilt}}$. The corresponding Fourier transformed curves $\mathcal{F}[i_{\mathrm{abs}}(\omega')](t)$ are shown in panel (b).

cient and the Fourier transform read:

$$i_{\mathrm{abs}}(\hbar\omega = \sqrt{\hbar\omega'}) = \frac{2v^2\hbar\mu_0 ce^2}{l^2}\sum_{n,n'}\frac{1}{\epsilon_{n'}-\epsilon_n}\left|Q^{n'}_n\right|^2\frac{1}{\pi}\frac{\Gamma}{\Gamma^2+(\epsilon_{n'}-\epsilon_n-\sqrt{\hbar\omega'})^2},$$
$$\mathcal{F}[i_{\mathrm{abs}}(\omega')](t) = \int_0^\infty \mathrm{d}\omega' e^{-i2\pi t\omega'} i_{\mathrm{abs}}(\hbar\omega = \sqrt{\hbar\omega'}). \tag{3.13}$$

Fig. 3.5 shows the rescaled absorption curves and the corresponding Fourier transformed curves for the Weyl materials for several β using linearly polarized light with $\theta = \theta_{\mathrm{tilt}}$. At $\beta > 0.3$ we find one significant Fourier transformed peak, whose location is determined by β. In the small β regime, however, an additional satellite peak appears, as expected from the analysis of the arc pattern in the previous section.

Based on the discussion of the previous section, we expect that by tuning the angle of the linearly polarized light there exists a particular polarization direction for which the visibility of the oscillations of the absorption curves is optimal, and at a perpendicular direction the oscillations vanish. The same is true for the Fourier transformed peaks. This is shown in Fig. 3.6(a) for the Weyl materials, in which case the direction of optimal visibility is the tilt direction. For graphene, this is the direction of the electric field.

One can effectively use the above discussed properties to determine experimentally the tilt parameter β and the tilt direction θ_{tilt}, which have been unaccessible so far. The experimental procedure we propose is based on applying linearly polarized light. By

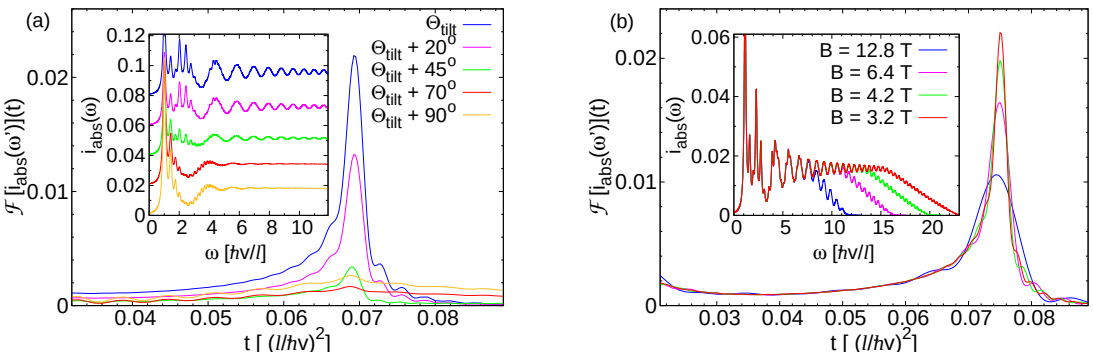

Figure 3.6: Panel (a) shows both the absorption coefficient $i^{\mathrm{W}}_{\mathrm{abs}}(\omega)$ (inset) and the corresponding Fourier transformed curves using $\beta = 0.6$ and linearly polarized light with various angles of the polarization. In a similar arrangement ($\beta = 0.5$ and using linearly polarized light with $\theta = \theta_{\mathrm{tilt}}$), panel (b) depicts how the number of available LLs affects the height of the Fourier transformed peaks. Arbitrary values of $B = 12.8, 6.4, 4.2, 3.2$T have been chosen, that correspond to 25, 50, 100 and 150 LLs.

tuning the angle of the polarization θ and measuring the optical absorption, its high-frequency, oscillatory behaviour could also be tuned. By identifying the angle, where the oscillations vanish, one can determine θ_{tilt}. Once in the tilt direction (perpendicular to the one before), the location of the Fourier transformed peaks is directly linked to the parameter value β. Fig. 3.7 shows the location of the peak(s) as a function of the tilt parameter in the direction of the tilt.

Extracting β is straightforward in the moderate-tilt limit, $\beta \leq 0.35$, via the splitting of the two peaks in $\mathcal{F}[i_{\mathrm{abs}}(\omega')](t)$. In the large-tilt region, however, there is only one peak. To extract the exact value of β, one should have an independent value for the Fermi velocity. Note that it is not straightforward to measure the Fermi velocity, as the density of states $\rho(\epsilon) = \epsilon/2\pi v_x v_y \hbar^2 (1-\beta^2)^{3/2}$ does not depend on the velocity solely, but is also a function of β, which we wish to determine, see Ref. [53]. Thus it is more useful to plot the location of the peak in units of $(l/\hbar v^*)^2$, where $v^* = \sqrt{v_x v_y}(1-\beta^2)^{3/4}$, see Fig. 3.8. The velocity v^* is measurable directly in thermodynamics or low-frequency magneto-optics.

Finally, we consider the issue of the number of available LLs. For graphene the linear dispersion relation is valid up to 1.5eV, therefore the available number of LLs is high enough to see the above oscillations in the absorption, the question of cutoff

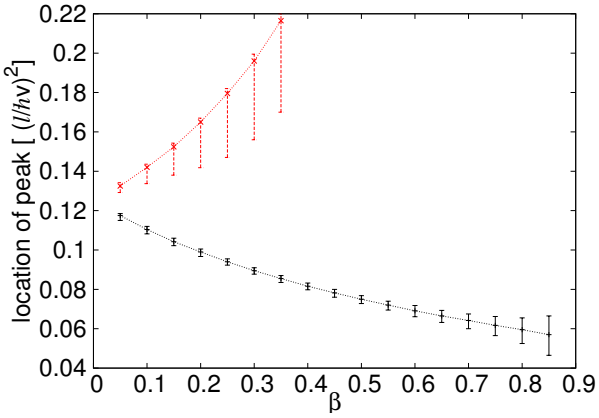

Figure 3.7: The location of the peak(s) in the Fourier-transformed rescaled absorption spectrum $\mathcal{F}[i_{\text{abs}}(\omega')](t)$ for linearly polarized light with $\theta = \theta_{\text{tilt}}$ as a function of the tilt parameter β for a 2D Weyl material. Error bars indicate the FWHM assuming a Lorentzian broadening.

does not arise. However, the number of LLs within the range of validity of the Weyl Hamiltonian is limited, we examine the robustness of our results against the change of the LL cutoff. We estimated the number of available LLs as $320/B$.[6] The inset of Fig. 3.6(b) shows the effect of an arbitrary change of the magnetic field with this particular cutoff. By lowering the available number of LLs, the oscillatory behaviour remains visible in the $i^{\text{W}}_{\text{abs}}(\omega)$ curves. The relevant peaks of $\mathcal{F}[i_{\text{abs}}(\omega')]$ also survive, though with reduced height. We can see that the oscillatory behaviour of $i^{\text{W}}_{\text{abs}}$ is present for as few as 25 LLs ($B = 12.8$T). We conclude that our previous predictions are valid up to $B \approx 6.5$T, which is a safe choice of the magnetic field.

3.4 Concluding Remarks and Future Perspectives

In conclusion, the pseudo-relativistic nature of electrons in graphene in a crossed electric and magnetic fields and in 2D Weyl materials, such as aI3, manifests itself in unique magneto-optical properties. Large number of transitions beyond the usual dipolar ones become possible. Their coalescence at high frequencies is the fingerprint of the broken rotational invariance in both cases, either due to the particular tilt or to the electric field, which results in an oscillatory behaviour of the absorption coefficient

[6]The detailed discussion of the derivation is presented in Sec. 4.2.2

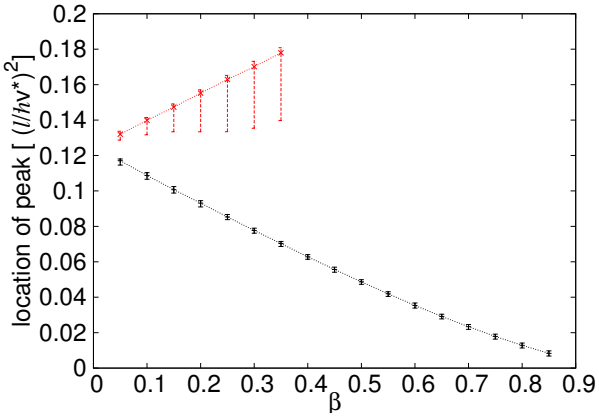

Figure 3.8: The same as in Fig. 3.7, but the location of the peak(s) are given in units $(l/\hbar v^*)^2$.

measured as a function of the frequency. We have pointed out that the oscillations show a strong β dependence, this feature may be exploited to determine the actual β parameter only by measuring the magneto-optical response under linearly polarized incident radiation.

In graphene, this effect might be observed easier than the earlier predicted LL collapse in Ref. [96], because the magneto-optical effect is present in the low-β range where the change of the LL energies is still small. Note that here the electric field is an experimentally tunable parameter, therefore experiments are only expected to verify our theory. However, a complication may arise due to screening of the external electric field. Here, as the LL energies are k dependent, see Eq. 2.16, the LLs may intersect the Fermi energy even in the middle of the sample, leading to an additional screening effect similar to that of the edge states at the boundaries of the sample, see Refs. [29] and [93]. The detailed analysis of the screening effect due to the k dependent LLs is delegated to future work.

We note that an upper limit to the achievable β-values in graphene is set by the condition that the potential energy change over a magnetic length should be less then the energy difference between adjecent LLs to avoid tunnelling current along the parallel electric field. For the $n = 0, 1$ LLs, this means $eE_{\parallel} l < \epsilon_1^{\mathrm{E}_{\parallel}} - \epsilon_0^{\mathrm{E}_{\parallel}} = \frac{\hbar v_F \sqrt{2}}{l}(1-\beta^2)^{3/4}$, which sets $\beta < 0.75$.

In aI3 and potentially other quasi-2D organic materials with massless Dirac cones,

see Sec. 2.4.4, on the other hand, a quantitative analysis of this phenomenon, in combination with other information on Fermi velocities if the tilt turns out to be large, helps us determine the tilt parameter and the tilt direction of the massless Dirac cones. In this context, however, the size of the window of the pressure cell may set an upper limit to the wavelength of the incident light. We propose therefore to extend our present calculations and determine the response measured in Raman spectroscopy.

Finally, we notice that the same magneto-optical features should appear in strained graphene, where uniaxial strain yields tilted Dirac cones, see Ref.[53]. Strained graphene is predicted to show a clear magneto-optical signature also in Raman spectroscopy, see[6].

Chapter 4

Magnetoplasmons - Density Oscillations in a Magnetic Field

4.1 Introduction

In the previous chapter we examined the magneto-optical properties of aI3 in a magnetic field and that of graphene in a crossed electric and magnetic fields assuming noninteracting electrons. In this chapter we aim to examine the collective excitations of aI3. For this we shall consider electron-electron interactions within the *random phase approximation*. Our objective is to calculate the density-density response function, hand in hand with the dynamical dielectric function, which yields the spectrum of collective excitations.

4.1.1 General Formalism of the Density-Density Response Function

Consider a perturbative external field given by its Fourier transformed amplitude $V_{\text{ext}}(\mathbf{k}, \omega)$ acting on the system of interacting electron gas and suppose that we are in a *linear response* regime.[1] As the external potential couples to the induced density

[1]Detailed discussion about the linear response theory and the various approximations of the interacting electron gas is available in many excellent textbooks. In the subsequent chapter I mainly rely on Ref. [52] by G. F. Giuliani and G. Vignale, Ref. [151] by J. Sólyom or Ref. [47] by A. L. Fetter and J. D. Walecka, though this list is far from being complete. In connection with the collective excitations of electron systems, see also the Refs. [19], [20] and [135].

of the electron system n_{ind} one of the quantities of crucial importance is the retarded density-density response function denoted as $\chi(\mathbf{k},\omega)$ and defined as

$$n_{\text{ind}}(\mathbf{k},\omega) = \chi(\mathbf{k},\omega)V_{\text{ext}}(\mathbf{k},\omega). \tag{4.1}$$

The calculation of the density-density response function $\chi(\mathbf{k},\omega)$ means the description of an interacting electron system, for which certain approximation methods are needed. The most frequently used approximation scheme is the random phase approximation (RPA), where χ is given as follows:

$$\chi^{\text{RPA}}(\mathbf{k},\omega) = \frac{\chi^{(0)}(\mathbf{k},\omega)}{\epsilon_r^{\text{RPA}}(\mathbf{k},\omega)} \equiv \frac{\chi^{(0)}(\mathbf{k},\omega)}{1 - v(\mathbf{k})\chi^{(0)}(\mathbf{k},\omega)}, \tag{4.2}$$

where we have introduced the dynamical dielectric function $\epsilon_r^{\text{RPA}}(\mathbf{k},\omega)$, the bare Coulomb interaction in 2D $v(\mathbf{k}) = e^2/2\epsilon_r\epsilon_0 k$, and $k = |\mathbf{k}|$ is the magnitude of the wave vector. $\chi^{(0)}(\mathbf{k},\omega)$ is the density-density response function of the noninteracting electron gas, usually called the Lindhard-function.[2] In diagrammatic perturbation theory the bare bubble diagram describes the interactionless propagation of an electron-hole pair, that is an electron and a hole disappears at a certain place but another electron-hole pair is created simultaneously in another place. To determine $\chi^{(0)}$ the usual procedure is to calculate the noninteracting, time-ordered response function, which is:

$$\chi^{\text{T}}(\mathbf{k},\omega) = -\frac{i}{\hbar}\text{Tr}\int\frac{\text{d}E}{2\pi}\int\frac{\text{d}\mathbf{p}}{(2\pi)^2}\mathcal{G}^{(0)}\left(\mathbf{p},E\right)\mathcal{G}^{(0)}\left(\mathbf{p}+\mathbf{k},E+\omega\right). \tag{4.3}$$

Here $\mathcal{G}^{(0)}(\mathbf{k},\omega)$ denotes the time-ordered, noninteracting Green's function, and Tr denotes trace. The retarded response function and the time-ordered response function relate to each other in the following way:

$$\begin{aligned}\text{Re}\chi^{(0)}(\mathbf{k},\omega) &= \text{Re}\chi^{\text{T}}(\mathbf{k},\omega),\\ \text{Im}\chi^{(0)}(\mathbf{k},\omega) &= \text{sgn}(\omega)\text{Im}\chi^{\text{T}}(\mathbf{k},\omega).\end{aligned} \tag{4.4}$$

A practically relevant property of the electron system which is simply deducible from

[2]This quantity may also be referred to as the bare or noninteracting polarization function or even free polarization bubble.

the bare density-density response function is the particle-hole excitation continuum or excitation spectrum (PHES). The PHES is a well-defined segment of the $\omega - \mathbf{k}$ space where $\mathrm{Im}\chi^{(0)}(\mathbf{k}, \omega) \neq 0$ and where it is possible to excite elementary electron-hole pairs.[3] Naturally, the PHES may also be characterized by $\mathrm{Im}\epsilon_r(\mathbf{k}, \omega) \neq 0$. The PHES is delimited by boundaries to be determined for each particular system.

Furthermore, the poles of the density-density response function determine the frequencies of the collective modes in an interacting many-body system. Besides the particle-hole excitations present in the PHES, where $\mathrm{Im}\chi^{(0)} \neq 0$, collective density oscillations appear where both the imaginary and real part of the dielectric function vanish. These density fluctuations, called plasmons, appear at the long wavelength limit, at higher energies than the boundaries of the PHES. The spectral weight of the electron-hole excitations is greatly reduced, part of the spectral weight is transferred to the plasmon mode. Further properties of an interacting electron gas, such as static screening, may also be deduced from the density-density response functions.

In the following chapter we apply the RPA to approximate the total polarizability of aI3 assuming a perpendicular magnetic field. First we review existing calculations of $\chi^{\mathrm{RPA}}(\mathbf{k}, \omega)$ and $\epsilon_r^{\mathrm{RPA}}(\mathbf{k}, \omega)$ for conventional 2DEG and for graphene. In the main part of the chapter we present a similar calculation for a more complex setup of aI3, thus we extend existing zero-field calculation of this material. In addition, we compare our results with graphene and analyze the effect of tilt and anisotropy of the Dirac cones on the collective modes of the layered organic compound.

4.1.2 Magnetoplasmons in Two-Dimensional Systems

In the present subsection we review the calculation of the dynamical dielectric function and the density-density response function in a conventional 2DEG with a parabolic dispersion relation and m_Q effective mass. First, we summarize the zero magnetic field results, then we review the non-zero field case.

In the case of a parabolic band only intraband excitations are possible, and the

[3]Note that for isotropic materials this reduces to the $\omega - k$ plane, where $k = |\mathbf{k}|$.

PHES is delimited by parabolic boundary lines

$$\omega_{\pm}^{Q}(\mathbf{k}) = \frac{\hbar^2}{2m_Q}k^2 \pm \frac{\hbar^2 k_Q^F}{m_Q}k, \tag{4.5}$$

where the superscript Q stands for *quadratic* and k_Q^F is the Fermi wave vector, see Fig. 4.1(a).

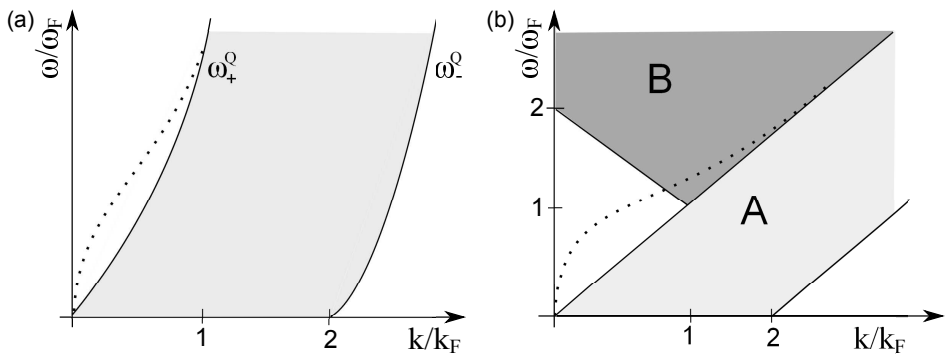

Figure 4.1: Panel (a): The shaded region corresponds to the PHES of a conventional 2DEG with a parabolic band. The demarcating lines of Eq. 4.5 are marked with solid lines. The plasmon mode is marked with a dotted line. Panel (b): The PHES of graphene. Intraband (A) and interband (B) excitations are marked separately. The plasmon mode is also shown. The forbidden region is left unshaded. Note that the momentum k and the energy ω are both measured in units of the Fermi momentum k_{F} and the Fermi energy ω_{F}, respectively.

In zero magnetic field the bare polarization function for 2DEG was first determined by Stern in Ref. [154]. As argued in [52], the imaginary part of the bare polarization function in zero magnetic field presents some structure, e.g. a higher spectral weight in the small energy region near the ω_{+}^{Q}, this feature forecasts the presence of the plasmon mode. Indeed, the $k \to 0$ limit of the plasmon mode, determined from the expansion of χ^{RPA} in [154], disperses as $\sqrt{k}$, and marked as a dotted line in Fig. 4.1(a). The plasmon mode touches the PHES at some critical value of k_c, disperses parallel to the boundary line, and is slowly Landau-damped due to the particle-hole pairs.[4] Note that within the RPA the boundaries of the PHES are identical with that of the noninteracting boundaries $\omega_{\pm}^{Q}(\mathbf{k})$.

For non-zero magnetic fields the eigenvalues and eigenfunctions of the 2DEG are

[4]This is in contrary to the 3D case, where the plasmon mode is heavily damped when entering the PHES at k_c, see Ref. [52].

given in Eqs. 2.2 and 2.3. The noninteracting polarization was determined in Refs. [72] and [89] and is given as follows

$$\chi_Q^{(0)}(\mathbf{k},\omega) = \frac{1}{2\pi l^2} \sum_{n' \leq n_Q^F} \sum_{n > n_Q^F} \left(\frac{|F_{n,n'}(\mathbf{k})|^2}{\omega - \epsilon_n^{\mathrm{Q}} + \epsilon_{n'}^{\mathrm{Q}} + i\delta} + \frac{|F_{n',n}(\mathbf{k})|^2}{-\omega - \epsilon_n^{\mathrm{Q}} + \epsilon_{n'}^{\mathrm{Q}} - i\delta} \right). \tag{4.6}$$

ϵ_n^{Q} is the LL spectrum introduced in Eq. 2.2, and n_Q^F is the index of the highest filled LL. In App. D we first calculate the bare Green's function, see D.1, then by Eq. 4.3 we determine the bare polarization function, see App. D.2. The corresponding form factor $F_{n',n}(\mathbf{k})$ is defined in App. E.1. Fig. 4.2 shows the noninteracting and the RPA polarization functions. Note that the color bar represents the magnitude of Imχ.

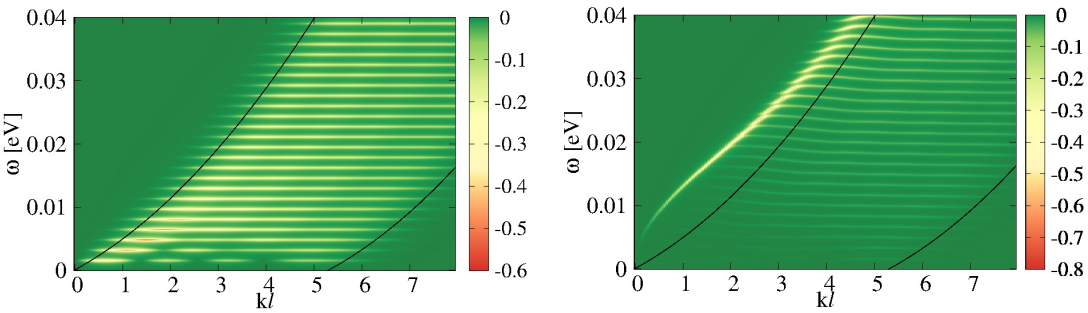

(a) Im$\chi_{\mathrm{Q}}^{(0)}$ (b) Im$\chi_{\mathrm{Q}}^{\mathrm{RPA}}$

Figure 4.2: Dimensionless polarization function for 2DEG. We use the following parameters: $\epsilon_r = 10$, $m_{\mathrm{Q}} = 0.3m_0$, $B = 4$T, $\delta = 0.1\hbar\omega_c$, $n_Q^F = 3$, the latter being the highest-filled LL and with m_0 we refer to the electron rest mass. The black curves denote the boundaries of the PHES calculated using Eq. 4.5. Note that the density-density response is divided by the density of states at the Fermi energy.

Due to the LL quantization the PHES is chopped into horizontal lines that are equally spaced, separated by $\hbar\omega_c$, as it is well-visible in Fig. 4.2(a). Here we choose a disorder broadening $\delta = 0.1\hbar\omega_c$, which determines the width of each horizontal line. Though the spectral weight is quite homogeneously distributed, there is a considerable *island* structure present in the particle-hole excitations in the lowest-energy range: here the horizontal lines are splitted into several parts, the number of parts are determined by the filling factor. The detailed discussion of the origin of this particular feature is given in Ref. [140].

The electron-electron interaction causes the appearance of a collective mode above

the PHES, see Fig. 4.2(b). This mode, which is the plasmon mode modified by the magnetic field, is referred to as the upper-hybrid mode (UHM).[5] An approximation for the dispersion relation of the UHM is given in Refs. [28] and [154]. Besides the UHM with certainly the highest spectral weight, the horizontal lines may be interpreted as magnetoexcitons, bound particle-hole pairs with well-defined center of mass momentum k. The notion of magnetoexcitons is introduced in detail later in Chap. 5. The avoided level crossings visible at higher energies in Fig. 4.2 are the so called Bernstein modes, which are the hybridization of the UHM and the inter-LL excitations, see [15]. This chapter is, however, devoted to the examination of the UHM as the latter collective mode is the best captured within the RPA.

Let us now consider monolayer graphene. A detailed review of the PHES and the collective modes of graphene is given in [54]. For zero magnetic field, the polarizability of graphene was first investigated by Shung in Ref. [149]. His primary interest was to examine the dielectric function and plasmon structure of graphene intercalation compounds, which consists of a series of (one or more) graphene and intercalated layers. As an intermediate step he considered a single graphene layer, calculated the dielectric function $\epsilon_r(\mathbf{k}, \omega)$, and determined its PHES as well as the plasmon modes. Besides, Ando examined graphene and its static screening and impurity scattering in Ref. [5], he emphasized the absence of backscattering, and examined its consequences. Wunsch *et al.* and Hwang *et al.* determined the dielectric function within the RPA, the plasmon mode and its decay rate, see Refs. [66] and [174]. Gangadharaiah *et al.* in Ref. [49] demonstrated that for undoped graphene summing up only the RPA bare bubble diagrams is insufficient, the inclusion of the ladder diagrams is necessary to capture the plasmon mode.[6]

To proceed, consider the particle-hole excitation spectrum in more detail, see Fig. 4.1(b). It consists of two different types of excitations, one is the intraband excitations (A), also available in 2DEG, the other is the interband excitations (B). In zero magnetic fields the bare polarizability is not homogeneously distributed within the PHES,

[5]Note that the same mode may also be referred to as magnetoplasmon, however we stick to the convention of using the term upper-hybrid mode instead.

[6]Here we note that in the present chapter we only deal with doped cases when determining the dielectric function for aI3, therefore the inclusion of the ladder diagrams is not necessary.

contrary to the 2DEG. Here, the chirality factor plays a crucial role, making most of the spectral weight center around the line $\omega = v_F k$. Within the RPA, the plasmon mode appears with the same $\sqrt{k}$ type dispersion relation as for 2DEG. The plasmon enters the interband excitation region and is damped there.

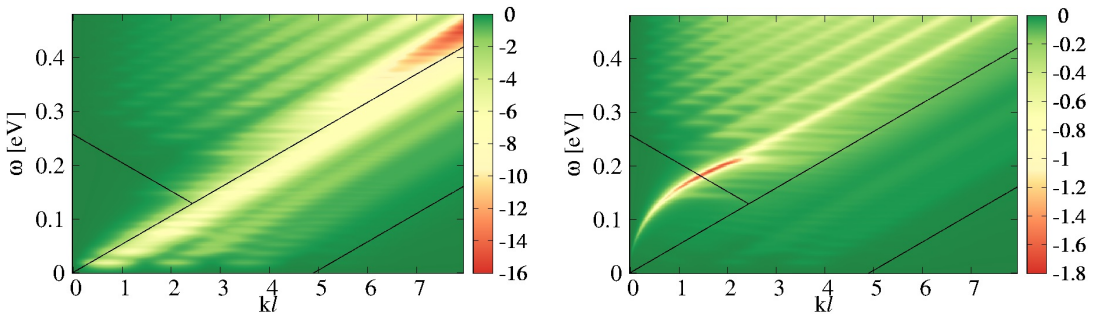

(a) $\mathrm{Im}\chi_{\mathrm{G}}^{(0)}$ (b) $\mathrm{Im}\chi_{\mathrm{G}}^{\mathrm{RPA}}$

Figure 4.3: The dimensionless density-density response function for graphene. The figures are reproduced from Ref. [140] with the parameters $\epsilon_r = 1$, $n_G^F = 3$ and $B = 4$T. The density-density response is divided by the density of states at the Fermi energy.

Consider now doped graphene in non-zero magnetic field. In Fig. 4.3 we reproduce the noninteracting density-density response function $\chi_{\mathrm{G}}^{(0)}$ and also the density-density response within RPA $\chi_{\mathrm{G}}^{\mathrm{RPA}}$. As shown in panel (a), the PHES is also chopped into horizontal lines, but due to the LL quantization of Eq. 2.10, these lines are not equidistantly spaced, rather their density increases even at moderate excitation energies, so they overlap even at small disorder broadening. Furthermore, each horizontal line is split into several parts, referred to as islands. The appearance of these islands is similar in nature to the case of 2DEG, however, due to the non-equidistant LL spacing they do not merge, but remain separated for all horizontal lines. These two effects together with the chirality factor lead to the appearance of linear magnetoplasmons visible in χ^{RPA}. Though these modes are essentially a coalescence of magnetoexcitons, their high spectral weight justifies their identification as a distinct mode. In χ^{RPA} the UHM is also visible, starts in the forbidden region, and ends in the interband region. Moreover, Bernstein modes are also visible in Fig. 4.3(b), the detailed discussion of their appearance in graphene is given in Ref. [142].

4.2 Magnetoplasmons in α-(BEDT-TTF)$_2$I$_3$: the Continuum Model

The calculation of the polarization function in aI3, considering its linear valleys only, is a non-trivial extension of the isotropic graphene-case, as here due to the anisotropy and tilt one shall consider the $\omega - \mathbf{k}$ space instead of the usual $\omega - k$ plane. Studying one of the anisotropic Dirac cones in zero magnetic field, which is undoubtedly an unphysical situation, one expects the occurrence of the plasmon mode just like in graphene, however with an angle dependent dispersion. Indeed, this expectation is verified by Nishine *et al.* in Ref. [120]. However, the presence of two oppositely tilted Dirac cones, which is the physically relevant situation, necessitates the investigation of their interplay. This leads us to the question of the number of plasmon modes and their mutual damping characteristics. This issue was discussed in Ref. [121]. Indeed, Nishine *et al.* identified a new plasmon mode and interpreted its appearance in terms of the *plasmon filtering effect*.

In this chapter our aim is twofold. First we extend the existing zero-field calculation, comprising both Dirac cones, to the non-zero magnetic field case. We give a comprehensive explanation for the appearance of the new plasmon mode in terms of *intervalley-damping*. Second we include the massive valley and determine how its presence affects the polarization of the linear valleys. This inclusion leads us to the so called *three-valley model*. By doping and/or tuning the magnetic field it is possible to switch on and off the massive valley, therefore it might be possible to experimentally verify its presence or absence.

4.2.1 The Particle-Hole Excitation Spectrum at $B = 0$T Field

Nishine *et al.* discussed the dynamical dielectric function and the density-density response function of aI3 in [120] and [121]. They detemined the $\chi^{(0)}(\mathbf{k}, \omega)$ and $\chi^{\mathrm{RPA}}(\mathbf{k}, \omega)$ in a semi-analytic calculation. Dealing only with one of the cones they determined the angle dependence of the boundaries of the PHES, and extensively discussed the effect of tilt and anisotropy on the various quantities, including the optical conductivity and screening. They found an angle dependent $\hbar\omega \sim \sqrt{k}$ behaviour for the plasmon mode.

Considering the two cones together they calculated the collective modes within RPA. They observed a new mode besides the regular one at an intermediate and large k range, whose presence and spectral weight depend strongly on the angle. They interpreted this as the cooperation between the two cones and called it a plasmon filtering effect: certain angles filter the new mode more effectively than others. As we shall see later in Sec. 4.3, the non-zero magnetic field results show essentially the same phenomenon. Our basic premise, however, is that each valley has its own proper plasmon mode, and we give a comprehensive interpretation in terms of the damping effect between valleys named as *intervalley-damping*.

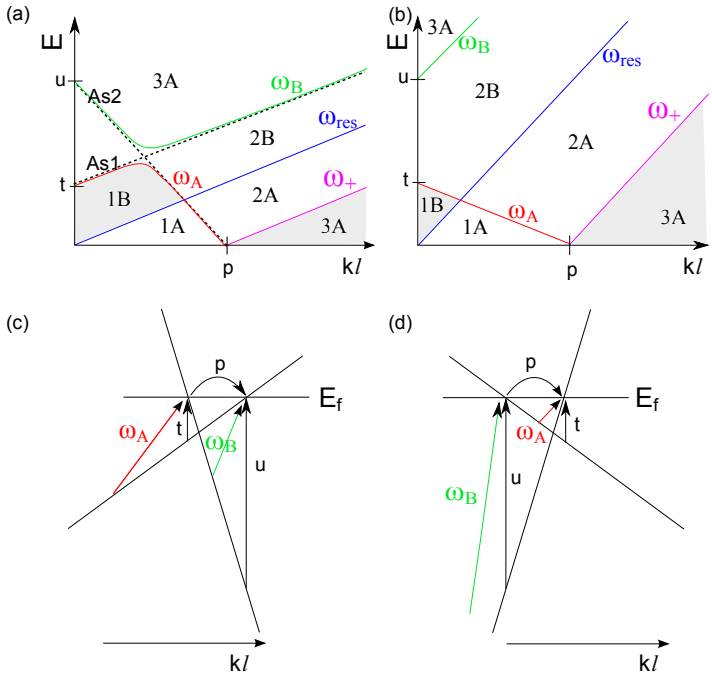

Figure 4.4: The regions and subregions of the (ω, k) plane from the point of view of (a) cone R, and (b) cone L in a particular direction $\theta = \theta_{\text{tilt}}$. (c,d) Cuts of cones R and L in the same direction. In the direction $\theta = \theta_{\text{tilt}} + \pi$, the cones L and R are interchanged, such that the panels (a,c) would correspond to cone L and (b,d) to cone R. The distinguished energies t, u, momentum p, and asymptotes $As1, As2$ are indicated. The gray shading indicates the forbidden regions 1B and 3A, where there are no particle-hole excitations in the absence of electron-electron interactions. E_f denotes here the Fermi energy.

Regarding the possibility of particle-hole excitations, the (ω, k) plane can be divided into several regions. The regions of possible intraband (A) and interband (B) particle-hole excitations are separated by the boundary line ω_{res}. Due to the opposite tilt, the

various regions and their boundaries differ for the two cones in any general directions. Both regions are divided into subregions, as explained below.

Figs. 4.4(a) and (b) depict the (ω, k) plane in the direction $\theta = \theta_{\text{tilt}}$, where $\theta = \arctan(k_y/k_x)$ is the angle of the momentum. In this direction the steepness of cone R is minimal, while that of cone L is maximal. First consider cone R in this direction [Figs. 4.4(a) and (c)]. Zero-energy excitations must have a momentum transfer less than the major axis p of the ellipsoidal Fermi surface. Excitations with higher momenta require a minimal energy, which defines the upper boundary ω_+ of the forbidden subregion 3A, where $\text{Im}\chi_R^{(0)} = 0$.

Excitations with zero momentum transfer must be interband. For $k = 0$, there are two special energies. The smallest one is denoted t in Fig. 4.4. Below this energy no $k = 0$ excitation is possible. If we increase the total momentum of the particle-hole pair in the positive manner, we must move the hole in the $-k$ direction [see arrow at ω_A in Fig. 4.4(c)]. Then the excitation energy increases, which explains the rise of the boundary line ω_A for small momenta. By thus decreasing the hole's wave vector, one follows the asymptote $As1$ in Fig. 4.4(a), which ultimately merges into the boundary line ω_B.

Starting from u, one can decrease the excitation energy with positive total momentum; this branch corresponds to ω_B and follows asymptote $As2$ at small momenta, which merges into ω_A in the intraband region. At larger values of the momentum, ω_B asymptotically follows $As1$. The reason why the boundaries ω_A and ω_B deviate from the asymptotes $As1, As2$ and do not intersect each other is due to the 2D nature of the excitations, i.e., one needs to consider transitions outside of the one-dimensional cut examined so far. Between ω_A and ω_{res} no particle-hole excitations exist, thus region 1B is forbidden, just like 3A for intraband excitations.

If one considers excitations of cone L in the same momentum direction, the shapes of boundaries ω_B and ω_A differ considerably [Fig. 4.4(b)]. The smallest energy of a $k = 0$ excitation is still t. However, in contrast to cone R, it is possible to decrease the energy from t by moving the hole in the $-k$ direction [Fig. 4.4(d)], and the corresponding branch defines boundary ω_A. Starting from u one can only increase the excitation energy with a negative total momentum, and one thus obtains the branch corresponding

to ω_B. Naturally, the two cones are related by time-reversal symmetry, which also changes the sign of $\mathbf{k}$. The role of the R and L cones are therefore interchanged in the $\theta_{\text{tilt}} + \pi$ direction, and the regions of cone R (L) are then those in Figs. 4.4(b,d) [Figs. 4.4(a,c)].

4.2.2 Approximations and Methods

The Three-Valley Model

Consider the first Brillouin zone of aI3 in Fig. 2.11(b). In our *three-valley model* we incorporate the two linear valleys at R and L as well as the massive valley at X. We divide the Brillouin zone into regions where the linear dispersion relation (in a circle around R and L), the quadratic approximation (in a circle around X), or none of these is valid. As we are interested in low-energy, low-momentum excitations in this chapter, we can safely neglect those parts of the Brillouin zone that are outside of either the linear or the quadratic approximations, see also the discussion below.

Assume that the linear approximation is valid around R and L separately in a circular region, whose radius is chosen as about 1/8 of the side of the first Brillouin zone [$\approx 2\pi/(1\text{ nm})$]. This picture is consistent with the band structure obtained in Refs. [3], [75] and [81]. As it was mentioned in Chap. 2, there are several available parameter sets to describe the tilted cones. To be specific, we will use Kobayashi *et al.*'s estimate of the velocity parameters, see [82]:

$$v_0^x = -9.4\ 10^4\ \tfrac{\text{m}}{\text{s}},\quad v_0^y = -8.32\ 10^4\ \tfrac{\text{m}}{\text{s}},\quad v_x = 3.45\ 10^5\ \tfrac{\text{m}}{\text{s}},\quad v_y = 2.45\ 10^5\ \tfrac{\text{m}}{\text{s}}, \tag{4.7}$$

which yield $\beta = 0.437$, $\alpha = 1.18$, $\lambda = 0.89$, and $\theta_{\text{tilt}} = 51.14°$. We emphasize that we are focusing on qualitative features that hardly depend on this particular choice. Using these velocities the energy cutoff E_L^c and the number of available LLs n_L^c are

$$E_L^c \approx 0.16\text{eV}, \qquad n_L^c \approx 320/B\ [\text{T}]. \tag{4.8}$$

We estimate furthermore the Fermi wave vector. Based on Monteverde *et al.*'s electron density data in Ref. [111], k_L^F in the linear valleys is tiny, $k_L^F = \sqrt{4\pi\rho_L/g_L} \approx 2 \times 10^6$

m^{-1}, using $g_L = 4$ for valley and spin degeneracy.

The quadratic approximation is valid in a circle around point X, with a radius that is estimated to be 17.5% of the side of the first Brillouin zone. The massive valley is taken as isotropic with an effective mass

$$m_Q \approx 0.3 m_0. \tag{4.9}$$

The valley is hole-like, a paraboloid of revolution open from below. The Hamiltonian of the massive band is $\hat{H}_{\mathrm{Q}} = E_{\mathrm{offset}} - \frac{(-i\hbar\nabla + e\mathbf{A})^2}{2m_Q}$ and the LL spectrum is given by $\epsilon_n^{\mathrm{Q}} = E_{\mathrm{offset}} - \hbar\omega_c \left(n + \frac{1}{2}\right)$, where ω_c defined before. Notice that these non-negative integers actually number hole LLs. Combining the carrier densities measured by Monteverde *et al.* in [111] with Eqs. 4.7 and 4.9, the top of the massive band is about

$$E_{\mathrm{offset}} \approx 0.46\mathrm{meV} \tag{4.10}$$

above the Dirac point of the massless valleys. Similar calculations yield the cutoff energy E_Q^c and the number of LLs is n_Q^c as

$$E_Q^c \approx 0.15\mathrm{eV}, \tag{4.11}$$

$$n_Q^c \approx 390/B \text{ [T]}. \tag{4.12}$$

The Fermi mometum k_Q^F of the massive band is $k_Q^F = \sqrt{4\pi\rho_Q/g_Q} \approx 2 \times 10^7$ m^{-1}, using $g_Q = 2$ for spin degeneracy.

Polarizability of the Total System

We identify the collective modes in RPA using Eq. 4.2. $\chi^{(0)}$ is calculated from Eqs. 4.3 and 4.4. In Eq. 4.3, $\chi^{\mathrm{T}}(\mathbf{k}, \omega)$ picks up a contribution only if $(\mathbf{p}, E)$ and $(\mathbf{p}+\mathbf{k}, E+\omega)$ specify one filled and one empty state. As we will restrict our attention to $\omega < \min(E_Q^c, E_L^c) \approx 0.15$eV, we can ignore the cases when both of these points are outside the vicinities of the L, R and X points, respectively, assuming that the Fermi energy is near the contact points. We can also ignore the cases where the states $(\mathbf{p}, E)$ and $(\mathbf{p}+\mathbf{k}, E+\omega)$ are in distinct valleys, as long as we focus on small momenta

$k < K \equiv \min(k_Q^c, k_L^c)$. This approximation is justified because the Coulomb interaction intervenes in the dielectric function $\epsilon^{\mathrm{RPA}}(\mathbf{k}, \omega)$, and suppresses intervalley contributions in comparison to intravalley contributions at fixed ω by a factor $v(K)/v(k_F) = k_F/K \ll 1$ near the characteristic Fermi momentum k_F. Furthermore, for small doping $\mu \ll \min(E_Q^c, E_L^c)$, we can also ignore the transitions that involve a state in the range of validity of the linear/quadratic approximations and a state outside of this domain. Thus we can safely approximate the bare polarizability for our limited purposes as the sum of the contributions of intravalley particle-hole pairs:

$$\chi^{(0)}(\mathbf{k}, \omega) \approx \chi_L^{(0)}(\mathbf{k}, \omega) + \chi_R^{(0)}(\mathbf{k}, \omega) + \chi_Q^{(0)}(\mathbf{k}, \omega), \tag{4.13}$$

where $\chi_{\mathrm{V}}^{(0)}(\mathbf{k}, \omega)$ is the polarizability contribution from intravalley transitions in valley V, with $V = L, R, Q$.

For illustration purposes, we consider occasionally the polarizability, the dielectric function and the density-density response functions stemming from only one or two valleys, even if such model systems are unphysical. Thus $\epsilon_V^{\mathrm{RPA}}(\mathbf{k}, \omega)$ and $\chi_V^{\mathrm{RPA}}(\mathbf{k}, \omega)$ are defined in terms of $\chi_V^{(0)}(\mathbf{k}, \omega)$ in an obvious manner, where V is either L, R, or Q for the respective valley. Moreover, we also consider cases with only two valleys taken into account. Sometimes this is a physically relevant situation, e.g., when the system is electron-doped or charge-neutral and the magnetic field is large, sometimes a theoretical contrast. Then we define $\chi_{V_1+V_2}^{(0)}(\mathbf{k}, \omega) = \chi_{V_1}^{(0)}(\mathbf{k}, \omega) + \chi_{V_2}^{(0)}(\mathbf{k}, \omega)$ and again $\epsilon_{V_1+V_2}^{\mathrm{RPA}}(\mathbf{k}, \omega)$ and $\chi_{V_1+V_2}^{\mathrm{RPA}}(\mathbf{k}, \omega)$ follow in analogy to Eq. 4.2.

Polarizability of the Linear Valleys

Based on Eq. 4.13 the determination of the density-density response of aI3 is reduced to the calculation of $\chi_Q^{(0)}(\mathbf{k}, \omega)$ and $\chi_{L/R}^{(0)}(\mathbf{k}, \omega)$. The polarizability of the quadratic valley is already presented in Eq. 4.6 and in App. D and App. E.1. In this chapter we calculate the bare polarizability of the linear valleys. The crucial difference with respect to the 2DEG is that now one must take into account the matrix structure of the Green's functions, which appears due to the spinorial wave function.

The field operators are given in terms of the spinorial wave functions ($\xi = \pm 1$)

$$\Psi_\xi(\tilde{\mathbf{r}}, t) = \sum_n \int \mathrm{d}q \Phi^\xi_{n,q}(\tilde{\mathbf{r}}) e^{-it\epsilon^{\mathrm{W}}_n} c_{\xi,n,q}, \tag{4.14}$$

$$\Psi^\dagger_\xi(\tilde{\mathbf{r}}, t) = \sum_n \int \mathrm{d}q [\Phi^\xi_{n,q}(\tilde{\mathbf{r}})]^\dagger e^{-it\epsilon^{\mathrm{W}}_n} c^\dagger_{\xi,n,q}. \tag{4.15}$$

Note that $[\Phi^\xi_{n,q}(\tilde{\mathbf{r}})]^\dagger$ is a row vector. Here $c_{\xi,n,q}$ denotes the annihilation operator of particles in ξ valley, n LL index and q momentum; spin index is suppressed for simplicity. We use the orbitals that Eqs. B.1 and B.3 specified in the rotated, rescaled coordinate system of Eq. 2.30. Even if the computation is more convenient in the rotated, rescaled coordinate system, the figures of Sec. 4.3 are presented in the non-rotated, non-rescaled coordinate system.

First we compute the time-ordered Green's function, which is by definition

$$\begin{aligned}\mathcal{G}^{(0)}_\xi(\tilde{\mathbf{r}}, \tilde{\mathbf{r}}', t) &= -i \left\langle \mathcal{T} \Psi_\xi(\tilde{\mathbf{r}}, t) \otimes \Psi^\dagger_\xi(\tilde{\mathbf{r}}', 0) \right\rangle \\ &= -i\Theta(t) \sum_{n',n} \int \mathrm{d}q \int \mathrm{d}q' \Phi^\xi_{n,q}(\tilde{\mathbf{r}}) \otimes [\Phi^\xi_{n',q'}(\tilde{\mathbf{r}})]^\dagger e^{-it\epsilon^{\mathrm{W}}_n} \langle c_{\xi,n,q} c^\dagger_{\xi,n',q'} \rangle \\ &\quad + i\Theta(-t) \sum_{n',n} \int \mathrm{d}q \int \mathrm{d}q' \Phi^\xi_{n,q}(\tilde{\mathbf{r}}) \otimes [\Phi^\xi_{n',q'}(\tilde{\mathbf{r}})]^\dagger e^{-it\epsilon^{\mathrm{W}}_n} \langle c^\dagger_{\xi,n',q'} c_{\xi,n,q} \rangle.\end{aligned} \tag{4.16}$$

Note that the time-ordered Green's function has a matrix structure, $\otimes$ denotes standard outer product of a column and a row vector, while $\mathcal{T}$ is the time-ordering operator and $\Theta(t)$ is the Heaviside step function. It is convenient to introduce the center of mass and relative coordinates, $\tilde{\mathbf{R}} = (\tilde{\mathbf{r}} + \tilde{\mathbf{r}}')/2$ and $\Delta\tilde{\mathbf{r}} = \tilde{\mathbf{r}} - \tilde{\mathbf{r}}'$. Then the Green's function is

$$\mathcal{G}^{(0)}_\xi(\tilde{\mathbf{R}}, \tilde{\mathbf{p}}, E) = \sum_n \int \mathrm{d}q \int \mathrm{d}\Delta\tilde{\mathbf{r}} e^{i\tilde{\mathbf{p}}\Delta\tilde{\mathbf{r}}} \frac{\Phi^\xi_{n,q}(\tilde{\mathbf{R}} + \frac{\Delta\tilde{\mathbf{r}}}{2}) \otimes [\Phi^\xi_{n,q}(\tilde{\mathbf{R}} - \frac{\Delta\tilde{\mathbf{r}}}{2})]^\dagger}{E - \epsilon^{\mathrm{W}}_n + i\delta \mathrm{sgn}(\epsilon^{\mathrm{W}}_n - \epsilon_F)}. \tag{4.17}$$

δ denotes the disorder broadening. The time-ordered response function in the rotated, rescaled coordinates is

$$\chi^{\mathrm{T}}_\xi(\tilde{\mathbf{k}}, \omega) = -i\mathrm{Tr} \int \frac{\mathrm{d}E}{2\pi} \int \frac{\mathrm{d}\tilde{\mathbf{p}}}{(2\pi)^2} \mathcal{G}^{(0)}_\xi(\tilde{\mathbf{R}}, \tilde{\mathbf{p}} - \frac{\tilde{\mathbf{k}}}{2}, E) \mathcal{G}^{(0)}_\xi(\tilde{\mathbf{R}}, \tilde{\mathbf{p}} + \frac{\tilde{\mathbf{k}}}{2}, E + \omega). \tag{4.18}$$

Note that in the evaluation of Eq. 4.18 one can essentially follow the derivation applied

in the case of 2DEG, however, here we have to take care of the matrix structure of the Green's function and execute the trace. The evaluation of the trace leads to the following equivalent expression

$$\begin{aligned}\chi_\xi^{\mathrm{T}}(\tilde{\mathbf{k}},\omega) = \int \frac{\mathrm{d}\tilde{\mathbf{p}}}{(2\pi)^2}\sum_{n,n'}\int \mathrm{d}q \int \mathrm{d}q' \frac{\Theta(\epsilon_{n'}^{\mathrm{W}}-\epsilon_F)-\Theta(\epsilon_n^{\mathrm{W}}-\epsilon_F)}{\omega+\epsilon_n^{\mathrm{W}}-\epsilon_{n'}^{\mathrm{W}}+i\delta\mathrm{sgn}(\omega)}\times \\ \times \int \mathrm{d}\Delta\tilde{\mathbf{r}}[\Phi_{n',q'}^{\xi}(\tilde{\mathbf{R}}+\frac{\Delta\tilde{\mathbf{r}}}{2})]^\dagger e^{i(\tilde{\mathbf{p}}-\frac{\tilde{\mathbf{k}}}{2})\Delta\tilde{\mathbf{r}}}\Phi_{n,q}^{\xi}(\tilde{\mathbf{R}}+\frac{\Delta\tilde{\mathbf{r}}}{2})\times \\ \times \int \mathrm{d}\Delta\tilde{\mathbf{r}}'[\Phi_{n,q}^{\xi}(\tilde{\mathbf{R}}+\frac{\Delta\tilde{\mathbf{r}}'}{2})]^\dagger e^{i(\tilde{\mathbf{p}}+\frac{\tilde{\mathbf{k}}}{2})\Delta\tilde{\mathbf{r}}'}\Phi_{n',q'}^{\xi}(\tilde{\mathbf{R}}+\frac{\Delta\tilde{\mathbf{r}}'}{2}).\end{aligned}$$

To proceed, first we execute the matrix multiplication, then we evaluate the integrals with respect to $\Delta\tilde{\mathbf{r}}$ (see App. E.2 for the derivation), finally we apply Eq. 4.4, which amounts to a simple sign change. Then we arrive at the noninteracting polarization function

$$\chi_\xi^{(0)}(\tilde{\mathbf{k}},\omega) = \frac{1}{2\pi\alpha^2 l^2}\sum_{n'\leq n_L^F}\sum_{n>n_L^F}\left(\frac{|\mathcal{F}_{n,n'}^{\xi}(\tilde{\mathbf{k}})|^2}{\omega-\epsilon_n^{\mathrm{W}}+\epsilon_{n'}^{\mathrm{W}}+i\delta}+\frac{|\mathcal{F}_{n',n}^{\xi}(\tilde{\mathbf{k}})|^2}{-\omega-\epsilon_n^{\mathrm{W}}+\epsilon_{n'}^{\mathrm{W}}-i\delta}\right). \quad (4.19)$$

n_L^F is the index of the highest filled LL. The corresponding form factors $\mathcal{F}_{n,n'}^{\xi}(\tilde{\mathbf{k}})$ are defined as follows

$$\begin{aligned}\mathcal{F}_{n',n}^{\xi}(\tilde{\mathbf{k}}) = \frac{1}{2}F_{|n'|,|n|}^{n',n,\xi}(\tilde{\mathbf{k}})+\frac{1}{2}\mathrm{sgn}(n)\mathrm{sgn}(n')F_{|n'|-1,|n|-1}^{n',n,\xi}(\tilde{\mathbf{k}}) \\ +\frac{\xi\beta}{2}\mathrm{sgn}(n)F_{|n'|,|n|-1}^{n',n,\xi}(\tilde{\mathbf{k}})+\frac{\xi\beta}{2}\mathrm{sgn}(n')F_{|n'|-1,|n|}^{n',n,\xi}(\tilde{\mathbf{k}})\end{aligned} \quad (4.20)$$

for $n, n' \neq 0$. Similarly for $n \neq 0 = n'$,

$$\mathcal{F}_{0,n}^{\xi}(\tilde{\mathbf{k}}) = \frac{1}{\sqrt{2}}F_{0,|n|}^{0,n,\xi}(\tilde{\mathbf{k}})+\frac{\xi\beta}{\sqrt{2}}\mathrm{sgn}(n)F_{0,|n|-1}^{0,n,\xi}(\tilde{\mathbf{k}}), \quad (4.21)$$

and finally, for $n = n' = 0$,

$$\mathcal{F}_{0,0}^{\xi}(\tilde{\mathbf{k}}) = F_{0,0}^{0,0,\xi}(\tilde{\mathbf{k}}). \quad (4.22)$$

Here we have introduced the functions $F_{|n'|,|n|}^{n',n,\xi}(\tilde{\mathbf{k}})$, which are defined in App. E.2. It is easy to check that $F_{|n'|,|n|}^{n',n,\xi}(\tilde{\mathbf{k}}) = \left[F_{|n|,|n'|}^{n',n,\xi}(-\tilde{\mathbf{k}})\right]^*$. Note finally that $\chi_L^{(0)}(\mathbf{k},\omega)$ and

$\chi_R^{(0)}(\mathbf{k},\omega)$ are related by the change of the sign of the tilt β.

4.2.3 Interaction Strength

Here we make a short comment on the possible appearance of correlated phases, including Wigner crystal phase in aI3, which might be the case when the interaction energy overcomes the magnitude of the kinetic energy. We characterize the relative strength of the interaction for each carrier type by the ratio between the interaction energy scale $E_{\text{int}} = e^2/(4\pi\epsilon_0\epsilon_r l)$ and the kinetic energy scale E_{kin} at the characteristic length scale $l \approx 1/k^F$. The kinetic energy scale depends on the carrier type.

For the massive carriers, $E_{\text{kin}} \propto l^{-2}$, and the ratio r_s depends on the Fermi wave vector,

$$r_s = \frac{E_{\text{int}}}{E_{\text{kin}}} = \frac{m_Q}{a_0\epsilon_r m_0 k_Q^F} \approx \frac{300}{\epsilon_r}, \tag{4.23}$$

where a_0 is the Bohr radius. For the estimate we have used the Fermi momentum as estimated for a specific sample in Subsec. 4.2.2. This ratio is traditionally called the Wigner-Seitz radius.

In contrast to the parabolic bands, the kinetic energy of massless Dirac carriers scales in the same manner as the interaction energy, $E_{\text{int}} \propto l^{-1}$, hence there is no characteristic length such as the Bohr radius. Indeed, the ratio between interaction and kinetic energy is independent of the electron density, and it may be characterized by a *fine structure constant* of aI3

$$\alpha_{\text{aI3}} = \frac{\alpha c}{\sqrt{v_x v_y}\epsilon_r} \approx \frac{20}{\epsilon_r}, \tag{4.24}$$

where $\alpha \approx 1/137$ is the fine structure constant of quantum electrodynamics. The origin of the rather large value of the ratio between the interaction and the kinetic energy is that the average Fermi velocity $\sqrt{v_x v_y} \approx 10^5$ m/s is an order of magnitude smaller than the corresponding velocity in graphene, see Ref. [82].

In view of this high value of the energy ratio for both the massless and massive carriers in aI3, one may expect the formation of correlated phases, such as the Wigner crystal. For the conventional 2D electron gas, $r_s \gtrsim 37$ is required to reach the Wigner

crystal phase of the massive carriers [164]. This would require in turn a dielectric constant $\epsilon_r < 10$. To the best of our knowledge there is no available experimental value for ϵ_r in aI3, but we expect it to be such as to rule out the Wigner crystal. In the linear valleys, the high value of the dielectric constant compensates for the small Fermi velocity, in which case, just like in graphene, one would not expect an instability of the semimetallic phase [34], [86]. Throughout the following calculations in Sec. 4.3 we assume that the Wigner crystal phase can be discarded, and use $\epsilon_r = 10$.

4.3 Results and Discussion

The PHES and the collective modes of aI3 at low energies are determined by the two massless Dirac cones and the massive hole pocket. The way the three valleys contribute to the density-density response depends on the doping and the perpendicular magnetic field. For significant electron doping the massive band is full at zero temperature and only the massless carriers contribute to the transport independently of the magnetic field. We discuss this case in Subsec. 4.3.1. In significantly hole-doped samples all valleys contribute. We consider this situation in Subsec. 4.3.2.

At charge neutrality the situation is more delicate. Then in zero magnetic field the chemical potential is between the Dirac point and the top of the massive band. By turning on the magnetic field, the central fourfold degenerate $n = 0$ LL of the massless valleys is fixed at the Dirac points, but the energy $E_{\text{offset}} - \hbar\omega_c/2$ of the topmost $n = 0$ LL of the massive valley decreases. Let B_{nm} be the field when the m-th LL of the massive valley coincides with the n-th LL of the conical valleys.

- For $B > B_{00}$, the $n = 0$ LL of the Dirac valleys is half-filled and the completely electron-filled massive valley is inert, see Fig. 4.5(a). The response is entirely due to the massless valleys and is discussed together with the electron-doped case in Subsec. 4.3.1.

- In the interval $B_{11} < B < B_{00}$ the chemical potential lies between the $n = 0$ LL of the linear band and the $n = 0$ LL of the massive band ($n_L^F = 0$, $n_Q^F = 1$), as depicted in Fig. 4.5(b). The excess electrons in the massless valleys (two per

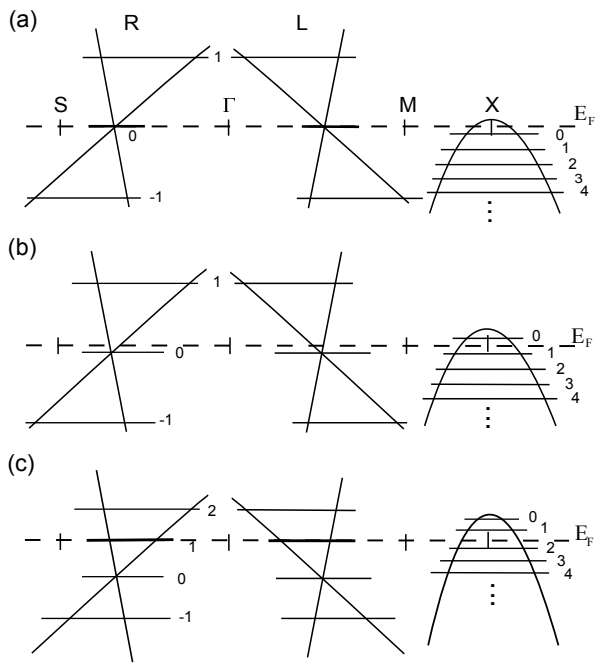

Figure 4.5: Schematic view of the LL structure of the two Dirac cones and the massive valley, with the chemical potential at charge neutrality indicated. (a) $B > B_{00} \approx 2.5$T, (b) $B_{11} < B < B_{00}$, and (c) $B \lesssim B_{11} \approx 0.06$T.

flux quanta) exactly compensate for the excess holes in the massive pocket. Now all valleys contribute to the density-density response, this case is investigated in Subsec. 4.3.2.

- For $B \lesssim B_{11}$, the $n = 1$ LL of the massive valley becomes empty and the fourfold degenerate $n = 1$ LL of the massless Dirac valleys is half-filled; the chemical potential is set somewhere in the (naturally broadened) $n = 1$ LL of the massless Dirac fermions, see Fig. 4.5(c). Here again all the three valleys contribute, Subsec. 4.3.2 applies.

Combining Eqs. 4.7 and 4.9, we estimate $B_{11} \approx 0.06$T and $B_{00} \approx 2.5$T.

4.3.1 Response of the Massless Carriers

With a significant electron-doping in mind, we set $n_L^F = 2$ and $n_Q^F = 0$, i.e., the massive band is full and inert for all realistic values of the magnetic field B. We first examine the response of a single tilted massless Dirac cone with the intention to highlight the direction-dependent effects. Although this model is not directly related to

a concrete physical situation, it reveals some basic phenomena associated with the tilt of the Dirac cones, such as the direction-dependent dispersion of the plasmon mode. This preliminary analysis within the single-cone approximation thus helps us understand the effect of the Coulomb coupling between the two different valleys, discussed in the second part of this subsection. Notice that for the electron-doped case the latter is actually the total density-density response.

The response of a single cone

Figs. 4.6(a) and 4.6(b) show $\mathrm{Im}\chi_R^{\mathrm{RPA}}$ and $\mathrm{Im}\chi_L^{\mathrm{RPA}}$ in the direction of R's smallest velocity $\theta = \theta_{\mathrm{tilt}}$, where we have also plotted the boundaries $\omega_+^{R/L}$, $\omega_A^{R/L}$, $\omega_B^{R/L}$, and $\omega_{res}^{R/L}$, the latter corresponding to the frequency ω_{res} for the right and the left cone, respectively. The zero-field boundaries correctly describe the regions of allowed transitions also for non-zero magnetic fields since the wave vector in the PHES is that of (neutral) electron-hole pairs. It therefore remains a good quantum number also in the presence of a magnetic field. Furthermore, we consider a finite broadening (inverse quasiparticle lifetime) $\delta = 0.1\hbar\sqrt{v_x v_y}/l$. Whereas treating δ as an energy-independent constant is a crude approximation,[7] we use it here only as a phenomenological parameter that renders the structure of the PHES more visible.

As shown in Fig. 4.6(a), the UHM is present with a considerable spectral weight in the originally forbidden region 1B of cone R in its tilting direction $\theta = \theta_{\mathrm{tilt}}$. For cone L, on the other hand, the spectral weight in region 1B in the same direction is definitely smaller, contrary to the naive expectations. The low spectral weight is due to the high value of the dielectric constant $\epsilon_r \approx 10$ we choose on the basis of Sec. 4.2.3. In Fig. 4.7 we have plotted a zoom of $\mathrm{Im}\chi_L^{\mathrm{RPA}}$ in region 1B for different values of ϵ_r. It is apparent that the spectral weight could be increased considerably by lowering the dielectric constant ϵ_r, the reason is that the weakening of the bare interaction pushes the zeros of the RPA dielectric function to higher momenta at fixed energy; eventually the UHM is forced to the borderline of region 1B for cone L in the given direction. All in all, in the physically relevant situation low spectral weight is expected. For cone R

[7] As a consequence of this crude treatment $\mathrm{Im}\chi_{R/L}^{(0)} \leq 0$ fails in generic directions in region 3A. But, $\mathrm{Im}\chi_{R+L}^{(0)} \leq 0$ and $\mathrm{Im}\chi_{R+L}^{\mathrm{RPA}} \leq 0$, as required.

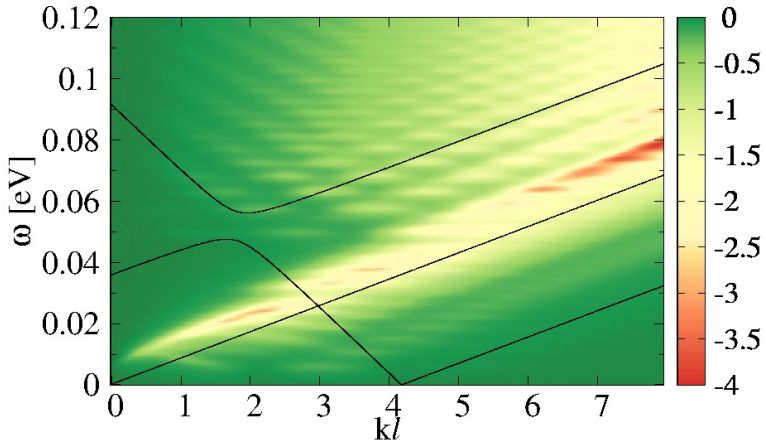

(a) $\mathrm{Im}\chi_R^{\mathrm{RPA}}$ in $\theta = \theta_{\mathrm{tilt}}$ or $\mathrm{Im}\chi_L^{\mathrm{RPA}}$ in $\theta = \theta_{\mathrm{tilt}} + \pi$

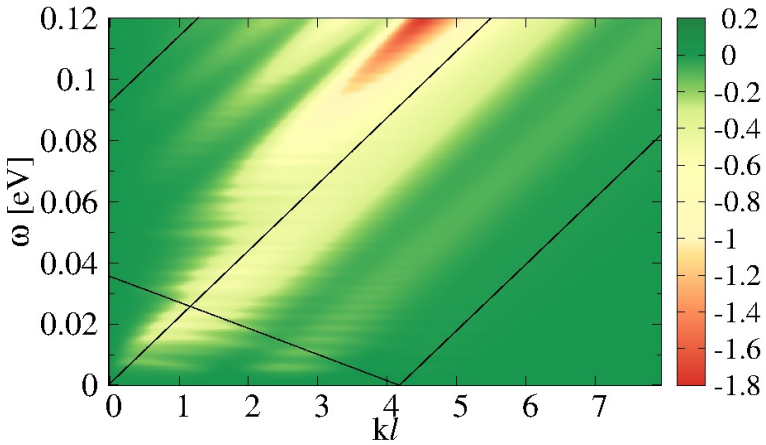

(b) $\mathrm{Im}\chi_L^{\mathrm{RPA}}$ in $\theta = \theta_{\mathrm{tilt}}$ or $\mathrm{Im}\chi_R^{\mathrm{RPA}}$ in $\theta = \theta_{\mathrm{tilt}} + \pi$

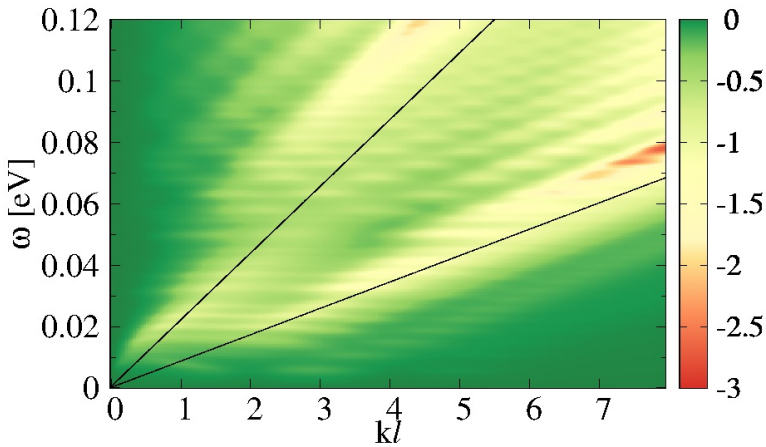

(c) $\mathrm{Im}\chi_{L+R}^{\mathrm{RPA}}$ in $\theta = \theta_{\mathrm{tilt}}$

Figure 4.6: The imaginary part of the dimensionless density-density response of massless carriers. The topmost filled Dirac LL is $n_L^F = 2$, the other parameters are $B = 4\mathrm{T}$ and $\epsilon_r = 10$. The first two panels consider the cones individually, while panel (c) shows $\mathrm{Im}\chi_{L+R}^{\mathrm{RPA}}$, which is the response of the total system for electron doping, or for $B > B_{00} \approx 2.5\mathrm{T}$ at charge neutrality. The straight lines are the boundaries of regions relevant at $B = 0\mathrm{T}$. Notice that in panel (c), we have only depicted the lines $\omega_{res}^{R/L}$ for the two cones, as a guide to the eye. In all cases the density-density response is divided by the density of states at the Fermi energy, making it a dimensionless quantity.

the tendency is similar but less significant.

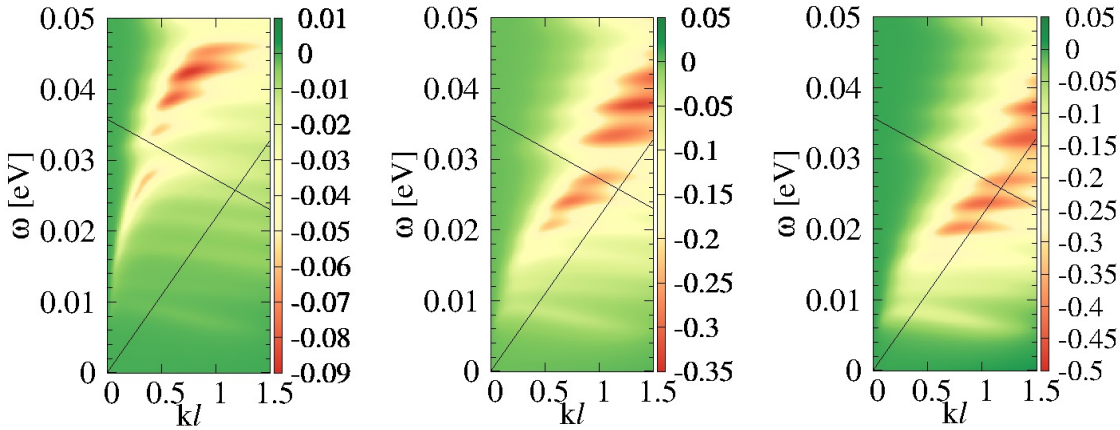

(a) $\epsilon_r = 1$ (b) $\epsilon_r = 4$ (c) $\epsilon_r = 7$

Figure 4.7: The dependence of the upper-hybrid mode of massless Dirac fermions on the background dielectric constant ϵ_r. We show $\mathrm{Im}\chi_L^{\mathrm{RPA}}$ in $\theta = \theta_{\mathrm{tilt}}$ direction, which is the direction opposite to cone L's maximal tilt, for different ϵ_r. The physical parameters are the same as in Fig. 4.6(b), which depicts $\epsilon_r = 10$. As previously, the density-density response is divided by the density of states at the Fermi energy.

After leaving region 1B, the UHM merges into the linear magnetoplasmon mode in region 2B. The concentration of the spectral weight near ω_{res} is in accordance with the $B = 0$T limit in [120] and the $B \neq 0$ behavior of graphene in [54]. Recall that the UHM arises due to the modification of the classical plasmons by cyclotron motion, see [28]. It does not require interband excitations, thus it forms by a transfer of spectral weight from the intraband PHES to the originally forbidden region 1B.

Observing the high-energy range in Fig. 4.6 we recognize the regular *island* structures, which is the alternation of the parts with high and low spectral weight in the (ω, k)-plane. Their structure in momentum space is exactly of the same origin as in the case of non-tilted cones discussed in [140]. The islands appear as the underlying Laguerre polynomials of the form factors in Eqs. 4.20 to 4.22 between deep-lying and high-energy LLs have many zeros.

To summarize, the density-density response of a generic massless Dirac cone in a perpedicular magnetic field exhibits an UHM and linear magnetoplasmons with anisotropic velocities, as a plausible generalization of the graphene case.

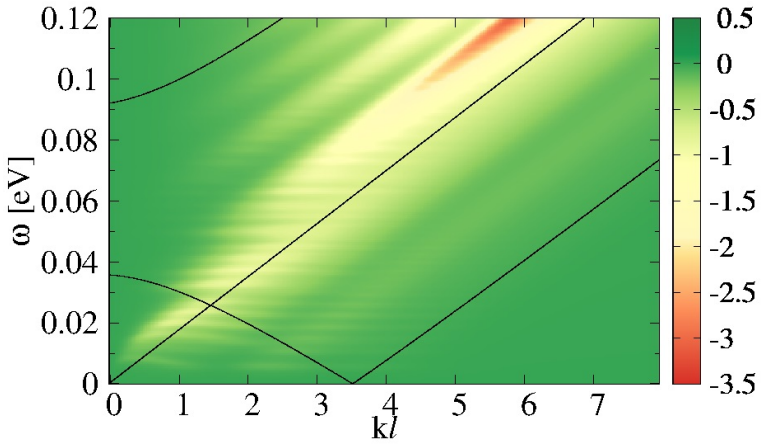

(a) $\mathrm{Im}\chi_R^{\mathrm{RPA}}$ in $\theta = \theta_{\mathrm{tilt}} + \pi/2$ or $\mathrm{Im}\chi_L^{\mathrm{RPA}}$ in $\theta = \theta_{\mathrm{tilt}} + 3\pi/2$

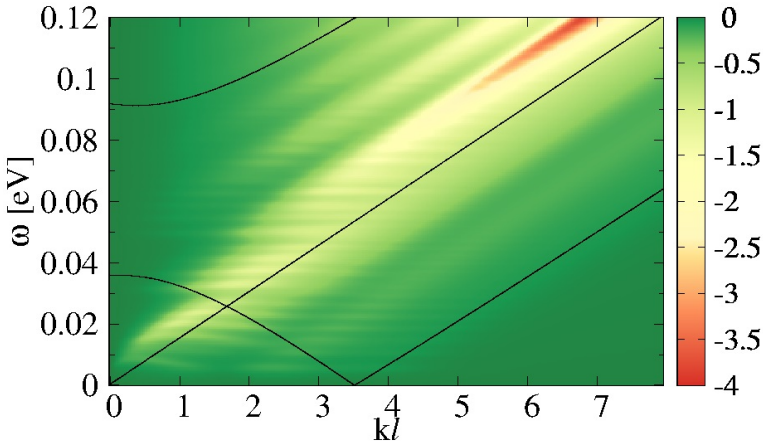

(b) $\mathrm{Im}\chi_L^{\mathrm{RPA}}$ in $\theta = \theta_{\mathrm{tilt}} + \pi/2$ or $\mathrm{Im}\chi_R^{\mathrm{RPA}}$ in $\theta = \theta_{\mathrm{tilt}} + 3\pi/2$

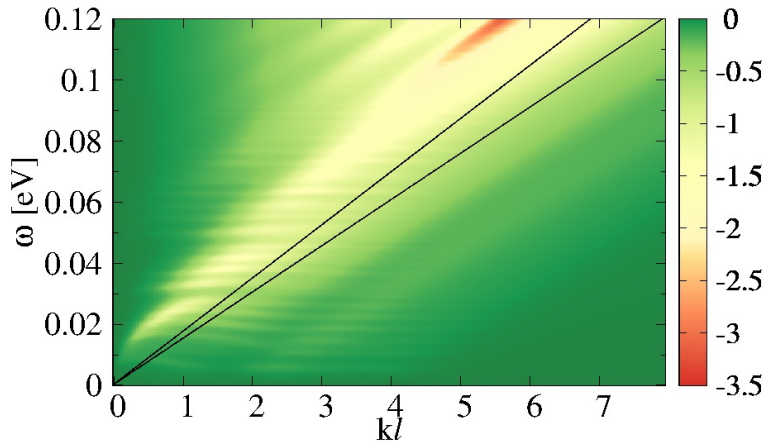

(c) $\mathrm{Im}\chi_{L+R}^{\mathrm{RPA}}$ in $\theta = \theta_{\mathrm{tilt}} + \pi/2$

Figure 4.8: The same as for Fig. 4.6, but for the direction perpendicular to the tilt.

Both Cones Considered

Fig. 4.6(c) shows $\mathrm{Im}\chi^{\mathrm{RPA}}_{L+R}$ for both cones in a fixed direction $\theta = \theta_{\mathrm{tilt}}$ of the momentum plane. The UHM of cone R disappears, though it was the most dominant part of the response in the single-cone approximation. The UHM of cone L is still present, though with a reduced spectral weight in its own forbidden region. Its linear magnetoplasmon mode manifests itself, although at high energies (R's region 2B), it is surrounded by the interband particle-hole excitations of cone R, which have a modest spectral weight in the single-cone approximation. Both modes are approximately in the same place as they were when only one cone was considered.

For interpretation, compare Fig. 4.4(c), where we sketch the (ω, k) plane in a fixed direction $\theta = \theta_{\mathrm{tilt}}$. The forbidden region of cone L lies entirely in that of cone R, hence no damping results from particle-hole excitations of either cones here. The picture is dramatically different for cone R: its forbidden region overlaps with the damped region of cone L, i.e., the UHM of cone R is strongly damped by particle-hole excitations in cone L. For this reason, the UHM of cone R disappears entirely. In the opposite direction the roles of L and R are, of course, interchanged. Therefore, the interaction of the two cones leads to a strong direction-dependent damping, which results in the complete suppression of the UHM of one cone where the other has particle-hole excitations of high spectral weight. This phenomenon, which we refer to as intervalley damping, is also visible in the imaginary part of the dielectric function (not shown).

The linear magnetoplasmons of each cone are situated in the particle-hole continuum of their own PHES respectively, where they are already damped. They do not overlap with each other in the (ω, k) plane in the shown direction $\theta = \theta_{\mathrm{tilt}}$. Therefore, we expect the dominance of the one with higher spectral weight at a particular (ω, k). Fig. 4.6(c) testifies the dominance of the linear magnetoplasmon mode of cone R in this direction, in agreement with its higher spectral weight in the single-cone model. This explains the reappearance of the linear magnetoplasmons at larger momenta, and the disappearance of the linear magnetoplasmons of cone L for intermediate momenta.

Fig. 4.8 shows the density-density response in the direction $\theta = \theta_{\mathrm{tilt}} + \pi/2$, i.e., perpendicular to the direction of the minimal steepness of cone R or maximal steepness of cone L. The responses of the individual cones are almost identical, see panels (a) and

(b), and their forbidden regions practically coincide.[8] Intervalley damping is therefore absent in this direction. The UHM and the linear magnetoplasmon mode of the two-valley system in panel (c) are where they would be for a single cone; albeit with an increased amplitude.

In order to illustrate the phenomenon of intervalley damping in a more precise and quantitative manner, consider the bare polarizability in Eq. 4.13 of a multivalley model, which is generically written as

$$\chi^{(0)}(\mathbf{k},\omega) = \sum_V \chi_V^{(0)}(\mathbf{k},\omega), \tag{4.25}$$

where the sum runs over all different valleys. One may thus rewrite the RPA dielectric function as

$$\epsilon^{\mathrm{RPA}}(\mathbf{k},\omega) = \epsilon_{V_0}^{\mathrm{RPA}}(\mathbf{k},\omega) - v(\mathbf{k}) \sum_{V\neq V_0} \chi_V^{(0)}(\mathbf{k},\omega), \tag{4.26}$$

where $\epsilon_{V_0}^{\mathrm{RPA}}(\mathbf{k},\omega)$ is the RPA dielectric function within a single-valley model, where only the valley V_0 is taken into account. The single-valley model therefore yields a good approximation for the collective modes [given by the zeros of $\epsilon^{\mathrm{RPA}}(\mathbf{k},\omega)$] if

$$v(\mathbf{k}) \sum_{V\neq V_0} \chi_V^{(0)}(\mathbf{k},\omega) \simeq 0 \tag{4.27}$$

in the region of interest, i.e. for $\omega = \omega_{pl}(\mathbf{k})$ obtained from the solution $\epsilon_{V_0}^{\mathrm{RPA}}(\mathbf{k},\omega_{pl}) = 0$. This precisely means that the spectral weight for particle-hole excitations in the other valleys $V \neq V_0$ vanishes in this region, or else that the collective modes of V_0 survive in the forbidden regions of the other cones, as observed in our calculations.

Notice that the phenomenon of intervalley damping is absent if all individual polarizabilities $\chi_V^{(0)}(\mathbf{k},\omega)$ are identical, e.g., in the absence of a tilt of the (albeit anisotropic) Dirac cones. In this case, the RPA dielectric function in Eq. 4.26 simply becomes

$$\epsilon^{\mathrm{RPA}}(\mathbf{k},\omega) = 1 - g v(\mathbf{k}) \chi_V^{(0)}(\mathbf{k},\omega), \tag{4.28}$$

for g identical valleys. Therefore, $\epsilon^{\mathrm{RPA}}(\mathbf{k},\omega)$ has only a single zero, at a slightly larger

[8] Perfect coincidence occurs at a nearby angle.

frequency as compared to the single-valley approximation because of the enhanced coupling $v(\mathbf{k}) \to gv(\mathbf{k})$. This situation is encountered, e.g., when one takes into account the spin degeneracy in conventional electron systems ($g = 2$) or in graphene with non-tilted Dirac cones with a fourfold spin-valley degeneracy ($g = 4$). The tilt of the Dirac cones, or more generally the broken $\mathbf{k} \to -\mathbf{k}$ symmetry in a single valley, is thus the basic ingredient for the mechanism of intervalley damping.

4.3.2 Response within the Three-Valley Model

Undoped samples with $B < B_{00}$ and hole-doped samples allow us to study the contribution of the quadratic valley. In this subsection we investigate how this third valley damps the collective modes of the linear valleys, and how the collective mode of the massive valley appears alongside the excitations of the massless valleys. Recall from Sec. 4.1.2 that a 2D quadratic band has a plasmon mode that disperses $\propto \sqrt{k}$, and in a magnetic field, this mode becomes the gapped UHM, in the same manner as for the linear bands.

Notice that the separation of the LLs scales as $\epsilon_n^{\mathrm{W}} \propto \sqrt{Bn}$ and $\epsilon_n^{\mathrm{Q}} \propto Bn$ for the massless and the massive carriers, respectively. One would therefore expect naively that the LLs of the quadratic valley are less dense in energy than those of the Dirac cones. However, due to the particular values of the Fermi velocities of the Dirac carriers and that of the band mass of the massive carriers, the LL separation of the massive carriers is much lower than that in the tilted Dirac cones in the magnetic-field range discussed here. Furthermore, the relative position of the collective modes of the massive and the massless valleys and the PHES of the three valleys are sensitive to both the magnetic field B and the doping level. Hence we discuss two representative cases, one at charge neutrality and relatively small magnetic fields $B < B_{00}$ (Fig. 4.9), and one at heavy hole-doping (Fig. 4.9). The two situations correspond to the sketches in Figs. 4.5(b) and (c), respectively.

We study the first case in Fig. 4.9, which depicts the density-density response at $n_L^F = 0$ and $n_Q^F = 1$, which is adequate at charge neutrality when $B_{11} < B < B_{00}$. We plot the direction $\theta = \theta_{\mathrm{tilt}}$, for which the difference between the velocities in the two cones is the most pronounced. In addition to the characteristic frequency $\omega_{res}^{R/L}$, we have

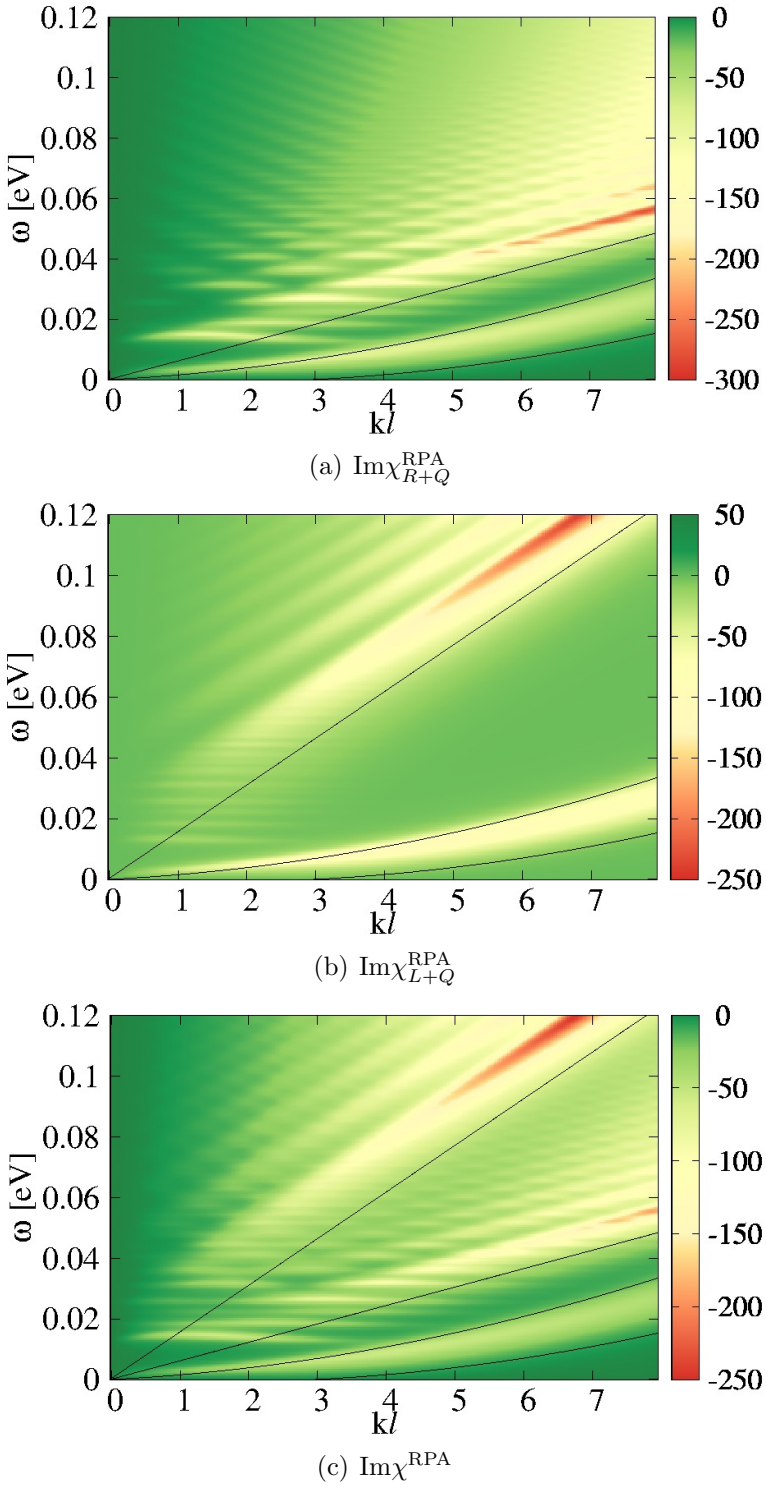

(a) $\mathrm{Im}\chi^{\mathrm{RPA}}_{R+Q}$

(b) $\mathrm{Im}\chi^{\mathrm{RPA}}_{L+Q}$

(c) $\mathrm{Im}\chi^{\mathrm{RPA}}$

Figure 4.9: The density-density response in direction $\theta = \theta_{\mathrm{tilt}}$ in momentum space. The topmost filled band is $n^F_L = 0$ in the massless valleys and $n^F_Q = 1$ in the massive valley. Other parameters are $B = 2\mathrm{T}$ and $\epsilon_r = 10$. The units are $\mathrm{s/m^2}$; normalization by the density of states is not applied. The straight line $\omega^{R/L}_{\mathrm{res}}$ is the boundary between the interband and intraband excitations of massless carriers, and the curved ones [$\omega^Q_\pm$ in Eq. 4.5] demarcate the particle-hole continuum of massive carriers for $B = 0\mathrm{T}$.

also sketched the lines $\omega_+^Q(\mathbf{q})$ and $\omega_-^Q(\mathbf{q})$, which delimit the particle-hole continuum of the massive carriers.

As it is demonstrated in Figs. 4.9(a) and 4.9(b), where one of the cones is disregarded for visibility reasons, the particle-hole continuum of the quadratic valley lies well below the linear magnetoplasmon mode of the massless Dirac carriers in both cones. In other words, the particle-hole excitations of the massive carriers do not overlap with those of the Dirac valleys, and its spectral weight is comparable to the dominant linear magnetoplasmon modes of the latter. It is the main reason that the UHM of the massive holes cannot be damped either, as it lies at very small energies, well below the cyclotron frequency of the massless carriers.[9]

The total, physical density-density response in Fig. 4.9(c) indicates that the response of aI3 in the lowest-energy range is determined by the massive carriers. At higher energies the Dirac carriers dominate, with intervalley-damped collective modes, as discussed above. The reason is the separation of energy scales, and not any difference in the density of states.

Fig. 4.10 shows the second case, a strongly hole-doped situation with $n_L^F = -2$ and $n_Q^F = 13$. Now the massive carriers are definitely involved in the damping. In direction $\theta = \theta_{\text{tilt}}$, the forbidden region 1B of cone R overlaps with the particle-hole continuum of the massive valley, see Fig. 4.10(a). Furthermore the UHM, which stems from the Dirac carriers, is found at a comparable energy as that associated with the massive carriers.[10] As a result, only one collective mode is discernible, which is damped once it enters the overlap region between the two lines ω_+^Q and ω_{res}^R, which is not a forbidden region for particle-hole excitations of the massive carriers. Furthermore, it is clear from Fig. 4.10(a) that the UHM avoids entering this region and rather approaches asymptotically the border ω_+^Q, as one expects for the UHM in a single-band model of massive carriers, for reference see [28] and [52]. However, the situation is slightly more involved in the present case, where one observes a coupling between the UHM with the linear magnetoplasmons of the massless Dirac carriers, which gives rise to a

[9]The former is characterized by the energy scale $\epsilon_1^{\text{Q}} \approx 0.001$eV, while the latter by $\epsilon_1^{\text{W}} \approx 0.015$eV at $B = 2$T.

[10]At $B = 4$T the cyclotron frequency is characterized by the energy scale $\epsilon_1^{\text{Q}} \approx 0.0023$eV for the massive carriers, while by $\epsilon_1^{\text{W}} \approx 0.02$eV for the massless ones.

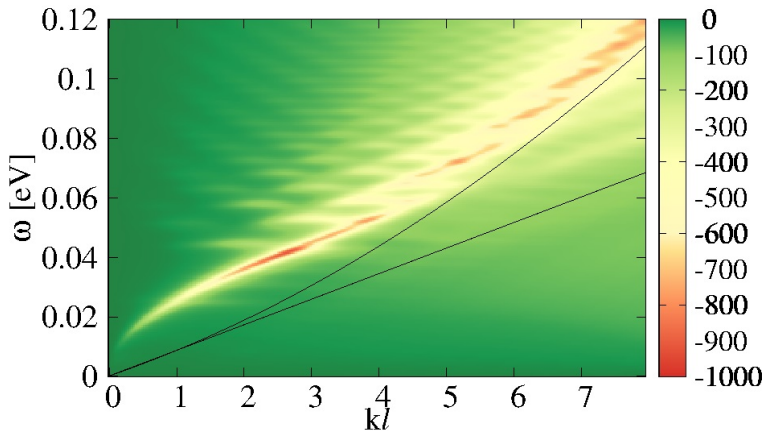

(a) $\mathrm{Im}\chi^{\mathrm{RPA}}_{R+Q}$

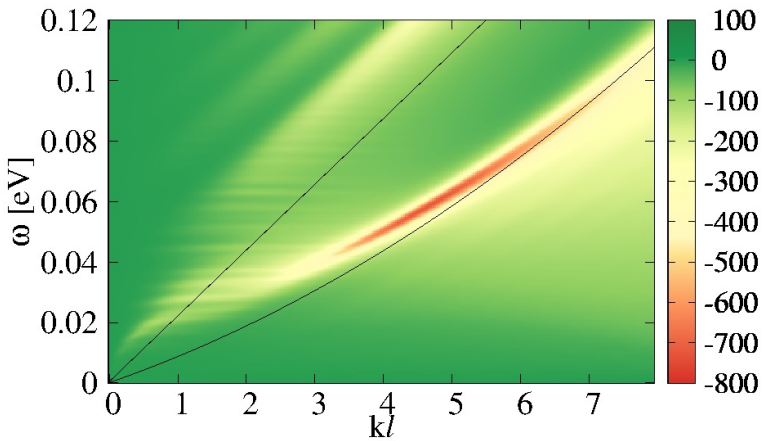

(b) $\mathrm{Im}\chi^{\mathrm{RPA}}_{L+Q}$

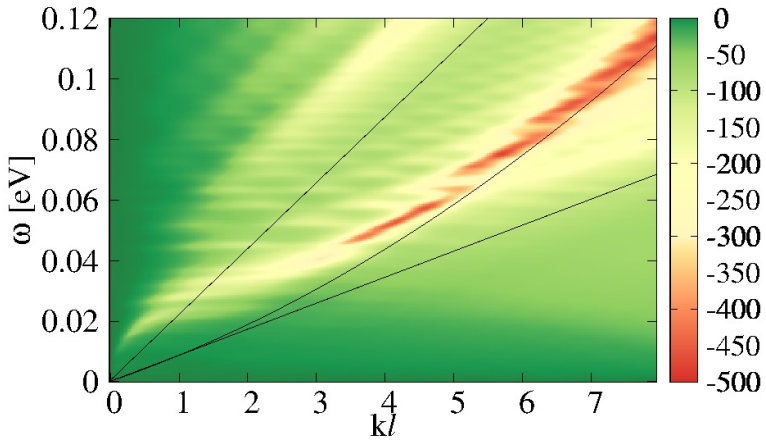

(c) $\mathrm{Im}\chi^{\mathrm{RPA}}$

Figure 4.10: The same as in Fig. 4.9, but in a hole-doped sample. The topmost filled massless LL is $n_L^F = -2$, while among the massive LLs it is $n_Q^F = 13$. Other parameters are $B = 4$T and $\epsilon_r = 10$. Notice that one of the curves demarcating the particle-hole continuum of the massive valley for $B = 0$T, ω_-^Q in Eq. 4.5, is not visible because $2k_Q^F$ is outside of the presented momentum range.

modulation of the spectral weight along the UHM. This coupling is reminiscent to the Bernstein modes discussed in the framework of graphene in Ref. [142]. For cone L (or cone R in the $\theta = \theta_{\text{tilt}} + \pi$ direction), on the other hand, the forbidden region of the massive valley overlaps with the 1A intraband region of the massless valley. The UHM is therefore strongly damped and almost invisible at small momenta but reappears at $kl \gtrsim 4$, as visible in Fig. 4.10(b). This reappearance of the UHM, even if it occurs in a region of possible intraband particle-hole excitations of the massless Dirac carriers, may be understood from the particular chiral properties of the latter. Indeed, the spectral weight of particle-hole excitations, in the case of Dirac fermions, is concentrated around the lines ω_{res} due to the suppression of backscattering, ([5], [66], [86], [140], [149] and [174]) such that the UHM is barely damped once it is further away from ω_{res}.

In the regions where the allowed PHESs overlap, the one with the greater spectral weight dominates. This is visible in Fig. 4.10(a), where the particle-hole continuum of the massive valley is almost as bright as the more concentrated linear magnetoplasmon mode of the Dirac fermions. This also applies to the total, physical density-density response, Fig. 4.10(c), where the spectral weight is mostly concentrated on the excitations of the massive valley, although the linear magnetoplasmon of cone R becomes visible at large momenta.

4.3.3 Static Screening

The interplay between massless carriers in tilted anisotropic Dirac cones and massive holes in a roughly isotropic pocket gives rise to a remarkable doping-dependent angular dependence of the screening properties.

Fig. 4.11 shows the real part of the static bare polarizability $\text{Re}\chi^{(0)}(\mathbf{k}, 0)$, and the dielectric function $\text{Re}\epsilon^{\text{RPA}}(\mathbf{k}, 0)$ in the RPA, respectively. For electron-doping or charge neutrality at $B > B_{00} \approx 2.5$T, the bare polarizability shown in panel (a) is entirely due to the linear bands. This anisotropy is naturally inherited by the RPA dielectric function depicted in panel (b), which means that screening due to the discussed bands is anisotropic. If the magnetic field is reduced, $B < B_{00}$, however, massive carriers can also be polarized at zero temperature. Because of their higher density of states at small energies, their contribution is dominant in the total polarizability, which shows a very

weak angular dependence, see panel (c). As a result, screening is almost isotropic, see Fig. 4.11(d). The suppression of the anisotropic screening of the tilted cones by the massive valley naturally becomes stronger in hole-doped samples.

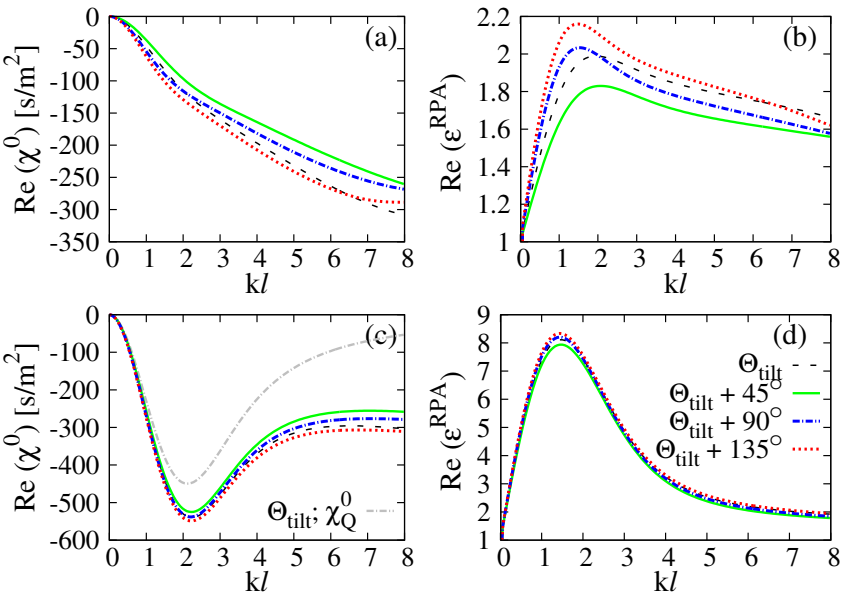

Figure 4.11: The static screening properties of aI3 at charge neutrality. Upper row: $B = 4$T, the massive valley is completely filled and inert. Lower row: $B = 2$T, the topmost LL of the massive valley is empty. Left panels: $\mathrm{Re}\chi^{(0)}(\mathbf{k}, 0)$ in s/m^2, right panels: $\mathrm{Re}\epsilon^{\mathrm{RPA}}(\mathbf{k}, 0)$. We show several directions in the momentum plane, specified by the angle θ relative to θ_{tilt}, the tilting direction of cone R. The grey line in panel (c) shows the polarizability of the massive valley, which is dominant and suppresses any anisotropy due to the tilted Dirac cones if $B < B_{00}$.

4.4 Conclusion

In this chapter we have studied the low-energy magnetic excitations and the collective modes of one conductive layer in aI3 within RPA. We have found that the tilt of the cones causes a direction-dependent intervalley damping of the upper-hybrid modes of the Dirac valleys, while the linear magnetoplasmons are less affected. The magnetoplasmons of the massive band may coexist with those of the massless ones, depending on doping and the strength of the magnetic field. The latter also tunes the system between isotropic and anisotropic screening regimes.

Magnetoplasmons have been studied in graphene nanoribbons through infrared transmission spectroscopy in Ref. [136], besides infrared nano-imaging has been successfully used in Ref. [44], however, these type of experiments may be challenging under high pressure. On the other hand, the layered structure of these organic conductors recommends itself to inelastic light scattering experiments, which have successfully clarified the intrasubband plasmon modes of multilayer GaAs-(AlGa)As heterostructures. Details on the method and some early experiments are presented in [42], [69], [125] and [153].

In the previous analysis we relied upon the three-valley model, which assumes the presence of two tilted and anisotropic massless Dirac cones and a massive hole pocket in the low-energy band structure of this material under high pressure or uniaxial strain. We based our model on ab initio calculations of Ref. [3], and transport experiments of Ref. [111], though we acknowledged the ambiguity regarding the presence of massive carriers. A recent theoretical analysis of Proskurin *et al.* in [137] investigated the magnetic field and temperature dependence of the longitudinal conductivity and provided an alternative interpretation of Monteverde *et al.*'s transport experiment in terms of a single-carrier scenario of Dirac electrons. Apparently, to resolve the ambiguity regarding the presence or absence of massless carriers is a timely issue and requires further experimental investigations, including e.g. the previously proposed infrared transmission spectroscopy or inelastic light scattering experiments. We believe that our theoretical predictions may shed light on the validity of the three-valley model.

Chapter 5

Magnetoexcitons - Bound Particle-Hole Pairs in a Magnetic Field

5.1 Introduction

In the final chapter of the present thesis we turn our attention to bilayer graphene. In Sec. 2.3 we have already reviewed its continuum model, we have introduced an effective 2×2 Hamiltonian to describe the low-energy dispersion relation, however we neglected trigonal warping. We have also presented the LL spectrum and the related orbitals: in bilayer graphene IQH states appear at filling factors $\nu = \cdots, -8, -4, 4, 8, \cdots$. When $|\nu| > 4$ Landau levels are fourfold degenerate, and commonly referred to as Landau band quartets, while at $|\nu| \leq 4$ an eightfold degenerate central Landau band or Landau band octet appears in the single-electron picture. The former degeneracy is caused by spin and valley, while in the latter case orbital degeneracy is also present. The relevance of orbital degeneracy makes bilayer and multilayer graphene especially interesting.

When the filling factor is integer the minimization of electron-electron interactions leads to the appearance of *quantum Hall ferromagnetic* (QHF) states, which are gapped states, they break either spin rotation or pseudospin (valley) rotation symmetry, or both. These symmetry breaking states arise due to exchange interaction, single-body

terms such as the Zeeman energy play a secondary role, see [51]. QHF also emerges in conventional two-component systems at odd integer fillings even if the Zeeman energy is tuned to zero. This observation straightforwardly generalizes to SU(n) systems, see [176]. In bilayer graphene QHF states appear at $\nu \in [-3, 3]$, as has been theoretically discussed in [9], [10], [16], [31], [55], [56], [57], [166] and [176]. Experimentally, quantum Hall plateaus have been observed at all of these integer filling factors through conductance measurements in Refs. [39], [45], [173] and [185]. Local compressibility measurements in [100] reinforce the above findings. In addition to those of the central Landau band, similar states have been observed in the $n = -2$ LL, see Ref. [8].

In this chapter we address the issue of the inter-LL excitations of bilayer graphene both in the IQH and QHF regimes. Because of the clear separation of the filled and empty Landau bands in the (mean-field) ground state, the excitations of both classes of quantum Hall systems are described in the same way, they are bound particle-hole pairs, called magnetoexcitons. Our main focus is the interaction-induced mixing of excitons between different LL pairs. For inter-LL excitations, the many-body corrections to cyclotron resonance have been calculated by renormalization in [146] including the possible particle-hole symmetry-breaking terms, but using the unscreened Coulomb interaction, with partial agreement with experiments of Ref. [62]. We believe that our approach, which allows the mixing of excitations between different LL pairs, is suitable to describe screening effects. To complement previous studies, we also investigate the finite wave vector behaviour of the excitations.

The chapter is organized as follows. First, we briefly comment on the reasons why Kohn's theorem does not apply for bilayer graphene, then we review the adaptation of the mean-field theory of magnetoexcitons to the case of bilayer graphene. Afterwards, we study the excitations of the IQH states at filling factors $\nu = \pm 4, \pm 8, \pm 12$, then we discuss QHF states of the central Landau band. We conclude the chapter with an outlook on experiments and a short note on recent theoretical results.

5.2 The Central Landau Band in Bilayer Graphene

In addition to the quantum number k electrons in the eightfold degenerate LL octet ($\Delta_Z, u \to 0$) is described by the spin index σ, valley (or equivalently layer) pseudospin ξ and orbital LL index n, the latter may also be interpreted as a pseudospin as $n = 0$ or 1. If either the Zeeman energy Δ_Z or the interlayer energy difference u is present, they affect the order how the LLs are filled, but exchange energy considerations are more crucial in most cases, see [9], [147]. The most convenient basis in pseudospin space may differ; we introduce symmetric (S) and antisymmetric (A) linear combinations as follows:

$$\hat{a}_{n,S,\sigma,k} = \cos\frac{\theta}{2}\hat{a}_{n,\xi=1,\sigma,k} + \sin\frac{\theta}{2}e^{i\phi}\hat{a}_{n,\xi=-1,\sigma,k}, \tag{5.1}$$

$$\hat{a}_{n,A,\sigma,k} = \sin\frac{\theta}{2}\hat{a}_{n,\xi=1,\sigma,k} - \cos\frac{\theta}{2}e^{i\phi}\hat{a}_{n,\xi=-1,\sigma,k}. \tag{5.2}$$

With a proper choice of θ and ϕ, Eqs. 5.1 and 5.2 include states of definite valley and intervalley phase-coherent states.

Barlas *et al.* showed that for balanced bilayers ($u = 0$), the eightfold degeneracy of the LL octet is lifted due to electron-electron interactions, and for integer filling factors it is filled according to *Hund's rule*: first spin polarization, then layer pseudospin, finally the orbital LL pseudospin is maximized, see Ref. [9] and Table 5.1.

ν	Filled states	$\nu_{\text{PH symmetric pair}}$
-3	(0,S,↑)	1
-2	(0,S,↑); (1,S,↑)	2
-1	(0,S,↑); (1,S,↑); (0,A,↑)	3
0	(0,S,↑); (1,S,↑); (0,A,↑); (1,A,↑)	-
1	(0,S,↑); (1,S,↑); (0,A,↑); (1,A,↑); (0,S,↓)	-3
2	(0,S,↑); (1,S,↑); (0,A,↑); (1,A,↑); (0,S,↓); (1,S,↓)	-2
3	(0,S,↑); (1,S,↑); (0,A,↑); (1,A,↑); (0,S,↓); (1,S,↓); (0,A,↓)	-1

Table 5.1: The filling of the LL octet for balanced bilayers follows Hund's rule, see [9].

Notice that $|\nu|$ and $-|\nu|$ pairs are not related by particle-hole symmetry, rather it connects states with ν and $\nu + 4$. Table 5.1 shows how various integer fillings are connected by particle-hole symmetry within the LL octet. In the following we handle

particle-hole related filling factors together.

For $\nu = 0$, Hund's rule implies that the state is ferromagnetic and the choice of the pseudospin basis is irrelevant. At this filling factor, however, two QHF ground states exist: a spin-polarized one and a valley-polarized (or equivalently layer-polarized) one, as discussed in [9], [55], [56], [57], [79], [80], [166] and [173]. Their respective range of validity is determined by the ratio of the Zeeman energy Δ_Z to the energy difference between the valleys, which in turn is related to the potential difference u.[1] For concreteness we are discussing the ferromagnetic state, where $\Delta_Z > u$. Here the magnitude of the pseudospin P^2 is a good quantum number of the excitations, while S^2 is not. See Fig. 5.6 for the transitions that span the Hilbert space of the mean-field Hamiltonian.

For $\nu = -2$, both the $n = 0$ and $n = 1$ orbital LLs of identical spin and pseudospin are filled, where ϕ and θ are determined by electrostatics (Fig. 5.8).

At $\nu = -3$ for $u = 0$ the ground state is an XY valley pseudospin ferromagnet, with orbital LL $n = 0$, that is, the state (0,S,↑) is fully filled, see Table 5.1. This state may also be referred to as intervalley phase-coherent state, the respective angles vary as $0 < \theta \leq \pi/2$.[2] As shown in [10], above a critical u^c, the ground state is (0,$\xi = 1$,↑), all electrons are in the bottom layer, or equivalently with valley pseudospin $\xi = 1$, with $\theta = 0$. Apparently, on both sides of u_c the ground state is a fully filled state, therefore bound particle-hole excitations may exist at any u. We will collect the possible magnetic excitations in Sec. 5.5.2, and show how their mixing influence the cyclotron resonance within a mean-field approach. For concreteness, we work in the $u = 0$ limit. The case of $\nu = -3$ is depicted in Fig. 5.10.[3]

At $\nu = -1$ the situation is more difficult, as discussed in detail in [31]. For $u = 0$ the ground state is given in Table 5.1, it is an XY valley pseudospin ferromagnet with

[1] At certain values of the in-plane pseudospin anisotropy, which may arise due to electron-electron and electron-phonon interactions, two more phases are possible: a canted antiferromagnet and a partially layer polarized state, see Ref. [79]. These recently proposed states are beyond the scope of our study.

[2] The states in Eq. 5.1 progress from the layer balanced limit $\theta = \pi$ at $u = 0$ to the layer polarized state $\theta = 0$; this limit is achieved about $u = u_c \approx 0.001e^2/(4\pi\epsilon_0\epsilon_r l)$, which is only 0.082 meV at $B = 20$T.

[3] As a side note, in the $u < u^c$ range Barlas identified a phase transition with a phase corresponding to a quantum Hall ferromagnet above a critical temperature T_c and a quantum Hall smectic state below T_c, see [10].

orbital LL index $n = 1$. At any finite potential energy difference the situation changes completely. At $u < u_1^c$ intervalley-coherent state emerges with unequal populations of the two valleys (layers), while at $u > u_2^c$ one valley is fully occupied, and in the other valley orbital coherence emerges. For intermediate potential energy differences mixed state appears with both intervalley and interorbital coherence. Due to the relevance of orbitally-coherent states, we do not handle this filling factor in the following.

To summarize, we have reviewed the QHF ground states of bilayer graphene at filling factors $\nu \in [-3, 3]$. We have concluded that our mean-field approach is not suitable to handle $\nu = -1, 3$ due to the appearance of orbitally-coherent states. It is, however, readily applicable to discuss $\nu = 0, \pm 2, -3, 1$. We emphasize that we work in the $u \to 0$ limit. The case when both u and Δ_Z Zeeman splitting are finite is discussed in detail in Ref. [88]. There Lambert *et al.* give a comprehensive picture of the various phases, including spin-, layer- and orbitally-coherent phases, that are realized as a function of u.

5.3 Kohn's Theorem and Interaction Strength

Kohn's theorem introduced in [83] states that interactions do not shift the cyclotron resonance in a parabolic band, it applies equally to 2D and 3D systems. In this section we review its derivation for conventional 2DEG, and also show following Roldán *et al.* in Ref. [141] why it fails for graphene, then we consider the case of bilayer graphene. We will see that the theorem also fails in the latter case, even though the bands of $\hat{H}_{\mathrm{B}}^{\xi}$ in Eq. 2.24 start quadratically at low energies, and those of $\hat{H}_{\mathrm{B,\ eff.}}^{\xi}$ in Eq. 2.25 are exactly parabolic for $v_3 = u = 0$.

Let us consider the case of 2DEG. Introduce the Hamiltonian of N noninteracting particles in a perpendicular magnetic field:

$$\hat{H}_0 = \frac{1}{2m_Q} \sum_{i=1}^{N} \mathbf{P}_i^2, \tag{5.3}$$

where $\mathbf{P}_i = \mathbf{p}_i + e\mathbf{A}(\mathbf{r}_i)$ with $\mathbf{p}_i$ and $\mathbf{r}_i$ being the canonically conjugate momentum and position operators and $\mathbf{A}$ is the appropriate vector potential of the homogeneous

magnetic field. The total momentum $\mathbf{P}$ is defined as $\mathbf{P} = \sum_i \mathbf{P}_i$, with its P_x and P_y components introduced straightforwardly as $P_x = \sum_i p_{i,x}$ and $P_y = \sum_i p_{i,y}$. Note that P_x and P_y are generators of global translations, hence they commute with any translation-invariant interaction. It is common practice to introduce ladder operators $P^{\pm} = P_x \pm iP_y$; $P^{\pm}$ acts among the eigenstates of the total kinetic energy operator $\hat{H}_0$. The commutation relation $[\mathbf{P}, \hat{v}] = 0$ can also be checked directly, here $\hat{v}$ is the direct Coulomb interaction. Let us now consider the interaction with a radiation field $\mathbf{A}^{\mathrm{rad}}(t)$. The perturbative Hamiltonian is

$$^{\mathrm{Q}}\delta\hat{H} = \sum_{i=1}^{N} \frac{\mathbf{p}_i \cdot \mathbf{A}^{\mathrm{rad}}}{m_{\mathrm{Q}}} \propto \mathbf{P}.$$

With this equation in mind, $[^{\mathrm{Q}}\delta\hat{H}, \hat{v}] = 0$ can be checked easily, it is valid independently of the fact whether $\mathbf{A}^{\mathrm{rad}}$ is described classically or quantum mechanically.

For monolayer graphene, the commutation relation $[\mathbf{P}, \hat{v}] = 0$ is equally valid, but the perturbative Hamiltonian has the form

$$^{\mathrm{G}}\delta H = \sum_{i=1}^{N} v_F \left(A_x^{\mathrm{rad}} \sigma_x + A_y^{\mathrm{rad}} \sigma_y \right). \tag{5.4}$$

As here $^{\mathrm{G}}\delta H$ is not proportional with $\mathbf{P}$, Kohn's theorem naturally fails. Thus the interaction energy may differ in the optically excited many-body state and the initial state, it may lead to a many-body correction to the cyclotron resonance even at zero momentum.

Let us now examine the case of bilayer graphene. Similarly to the previous case, $[\mathbf{P}, \hat{v}] = 0$ is valid. In the two-band model of bilayer graphene the interaction with the radiation field $\mathbf{A}^{\mathrm{rad}}$ leads to the perturbative Hamiltonian

$$^{\mathrm{B}}\delta\hat{H} \propto \sum_{i=1}^{N} \begin{pmatrix} 0 & [\mathbf{A}^{\mathrm{rad}}]^{+}\ \pi_i^{\dagger} \\ [\mathbf{A}^{\mathrm{rad}}]^{-}\ \pi_i & 0 \end{pmatrix}$$

with $[\mathbf{A}^{\mathrm{rad}}]^{\pm} = A_x^{\mathrm{rad}} \pm iA_y^{\mathrm{rad}}$, see [1] and [117]. It is straightforward to show that $^{\mathrm{B}}\delta\hat{H}$ maps a state $\Phi^{\mathrm{B}}_{n,q}$ to a linear combination of $\Phi^{\mathrm{B}}_{n+1,q'}$, $\Phi^{\mathrm{B}}_{n-1,q'}$, $\Phi^{\mathrm{B}}_{-n-1,q'}$ and $\Phi^{\mathrm{B}}_{-n+1,q'}$. If

three out of these transitions are Pauli-blocked, we may end up in an eigenstate of the kinetic part of the many-body Hamiltonian, but ${}^{\mathrm{B}}\delta\hat{H}$ is no longer proportional to a linear combination of P_x and P_y. Again, Kohn's theorem is doomed to fail.

Besides examining the validity of Kohn's theorem, another aspect is worth considering prior to further calculations, namely the relative strength of interactions with respect to the LL spacing. Following the ideas in Subsec. 4.2.3, we introduce the fraction r_s of interaction and kinetic energies, however now we assume the presence of a perpendicular magnetic field. In bilayer graphene r_s becomes

$$r_s = \frac{E_{\mathrm{int}}}{E_{\mathrm{kin}}} = \frac{e^2}{4\pi\epsilon_0\epsilon_r l}\frac{1}{\hbar\omega_c} \propto \frac{1}{\epsilon_r\sqrt{B}}. \tag{5.5}$$

Note that here E_{int} is evaluated at the magnetic length l. A similar analysis yields $r_s \propto \frac{1}{\epsilon_r\sqrt{B}}$ in conventional 2DEG. LL mixing is suppressed at high fields because of the $B^{-1/2}$ scaling of the relative strength of interactions. In monolayer graphene both the interaction and the kinetic energy scale with $B^{1/2}$, thus LL mixing is never suppressed, $r_s \approx 2.2/\epsilon_r$, a B independent constant. Note the similarity of bilayer graphene and the 2DEG: $r_s \to 0$ in the $B \to \infty$ limit and it scales with $B^{-1/2}$ in both cases. However, at fixed magnetic field and filling factor, LL mixing is more significant in the former case than in the 2DEG, because of the smaller dielectric constant and effective mass in bilayer graphene, the latter being $m \approx 0.07m_0$.

Determining its exact value for bilayer graphene, r_s is $1 < r_s < 8$ for realistic B and ϵ_r ($10\mathrm{T} \leq B \leq 40\mathrm{T}$, $1 \leq \epsilon_r \leq 4$), thus the extent interactions may mix transitions involving different LL pairs is by no means negligible.

One can also compare the Coulomb energy scale, $e^2/(4\pi\epsilon_0\epsilon_r l)$ to the energy difference between adjacent LLs, $\hbar\omega_c\left(\sqrt{n(n-1)} - \sqrt{(n-1)(n-2)}\right)$. This may give the impression that LL mixing is more important at higher filling factors, but the amplitude of the undulations of the unmixed magnetoexciton dispersions also gets reduced in higher levels; leaving the issue of the generic progress of LL mixing with increasing filling factor open.

5.4 Magnetoexcitons

Consider integer filling factors, where the filled and empty Landau bands are clearly separate.[4] In this case the low-energy excitations are magnetoexcitons, which are bound particle-hole pairs obtained by promoting an electron from a filled Landau band to an empty band. The concept of magnetoexcitons are introduced and discussed in detail in Refs. [23], [24], [72], [89] and [97]. We use the term magnetoexciton comprehensively: we refer to all spin (valley pseudospin) flip and spin (valley pseudospin) conserving modes as magnetoexcitons. We do so even though other expressions may be found in the literature, e.g. in [25] those inter-LL excitons conserving all quantum numbers are called magnetoplasmons, or in [141] Roldán *et al.* use the terms spin-flip, valley-flip and pseudospin-flip excitations. We do not use these terms; magnetoexcitons include all of these varieties.

The hole and the particle are bound by the attractive Coulomb interaction, forming a dipole with a separation of kl^2 at center-of-mass wave vector $\mathbf{k}$, where $k = |\mathbf{k}|$. They approach widely separated particle-hole pairs in the $k \to \infty$ limit. The latter limit determines the transport gap unless skyrmions form, see [46] and [152]. As the pair is neutral, taking appropriate linear combinations one obtains eigenstates of the total momentum.

Magnetoexcitons are created from the ground state by the operator

$$\hat{\Psi}^{\dagger}_{n\xi\sigma,n'\xi'\sigma'}(\mathbf{k}) = \sqrt{\frac{2\pi l^2}{A}} \sum_p e^{ipk_y l^2} \hat{a}^{\dagger}_{n,\xi,\sigma,p} \hat{a}_{n',\xi',\sigma',p-k_x}, \tag{5.6}$$

where A is the area of the sample, $\hat{a}^{\dagger}_{n,\xi,\sigma,p}$ creates a particle with spin index σ, valley index ξ, momentum p in the n LL, while $\hat{a}_{n',\xi',\sigma',p-k_x}$ removes simultaneously a particle with spin σ', valley index ξ' and momentum $p - k_x$ from the n' LL. Note that one may define such magnetoexcitons that the particle and the hole carry symmetric S or antisymmetric A valley indeces. In this case magnetoexciton operators are derived from destruction operators in 5.1 and 5.2 in an obvious manner.

[4] Our analysis below is valid in the IQH regime, and it applies to QHF states as well. Note, however, that we cannot handle orbitally-coherent states (see discussion in Sec. 5.2), therefore we do not consider $\nu = -1$ and 3.

Magnetoexcitons carry various quantum numbers. They have a well-defined center-of-mass momentum $\mathbf{k} = (k_x, k_y)$. These bound particle-hole pairs are eigenstates of the projection of spin and valley pseudospin operators S_z and P_z, as well as the magnitude of the spin and pseudospin S^2 and P^2. While the former two are always good quantum numbers, the latter ones are only well-defined when both spin (pseudospin) states are equally occupied, that is the ground state is spin (pseudospin) singlet. Furthermore, it is common practice to define the so called *angular momentum quantum number* of the exciton as

$$l_z = |n| - |n'|. \tag{5.7}$$

A similar quantity has been defined for graphene in [68], and for 2DEG in [72]; l_z appears in the two-body problem of the negatively charged electron and the positively charged hole. We emphasize that l_z is exactly conserved by the electron-electron interaction only in the $\mathbf{k} \to 0$ limit, where it is indeed related to angular momentum. At any finite wave vector, transitions with different l_z may mix.

In the low magnetoexciton density limit the interaction between magnetoexcitons may be handled within the mean-field approach. To determine the mean-field (Hartree-Fock) Hamiltonian of magnetoexcitons we used spinorial orbitals of Eq. 2.27, similarly to the adaptation found in Refs. [25], [68], [166]. Then the mean-field matrix elements are

$$\begin{aligned} H^{(\tilde{N}\tilde{N}')}_{(NN')}(\mathbf{k}) &= \langle 0|\hat{\Psi}_{\tilde{N},\tilde{N}'}(\mathbf{k})v(\mathbf{k})\hat{\Psi}^{\dagger}_{N,N'}(\mathbf{k})|0\rangle - \delta_{N\tilde{N}}\delta_{N'\tilde{N}'}\langle 0|v(\mathbf{k})|0\rangle \\ &= \delta_{N\tilde{N}}\delta_{N'\tilde{N}'}\left(\epsilon^{\mathrm{B}}_{n,\xi} - \epsilon^{\mathrm{B}}_{n',\xi'}\right) + \delta_{N\tilde{N}}\delta_{N'\tilde{N}'}\Delta(N,N') + E^{(\tilde{N}\tilde{N}')}_{(NN')}(\mathbf{k}) + R^{(\tilde{N}\tilde{N}')}_{(NN')}(\mathbf{k}). \end{aligned} \tag{5.8}$$

For simplicity we have introduced the compound notation $N = (n, \xi, \sigma)$, etc., and $\delta_{NN'} = \delta_{\sigma\sigma'}\delta_{\xi\xi'}\delta_{nn'}$, $\delta_{n,n'}$ being the Kronecker's delta. $v(\mathbf{k})$ is the Coulomb interaction, and $|0\rangle$ is the IQH or QHF ground state. Besides the single-particle energy difference of the n and n' LLs $\epsilon^{\mathrm{B}}_{n,\xi} - \epsilon^{\mathrm{B}}_{n',\xi'}$, where $\epsilon^{\mathrm{B}}_{n,\xi}$ is introduced in Eq. 2.26, three additional terms appear.

(i) The wave vector independent exchange self-energy difference of the two states. While the exchange self-energy itself is infinite for any orbital[5], its difference between

[5]Note that this is only true in our continuum approximation, where the dispersion relation goes to

two states,

$$\Delta(N,N') = \sum_{M \text{ filled}} \left(X_{N'M} - X_{NM}\right), \tag{5.9}$$

$$X_{N'N} = \frac{1}{(2\pi)^2}\int \mathrm{d}\mathbf{p} I^{N'N}_{N'N}(\mathbf{p}), \tag{5.10}$$

is finite. This is a peculiarity of bilayer graphene in the absence of an interlayer bias u. A simple regularization procedure also works for the four-band model, the shift $\Delta(N,N')$ is analogous to the Lamb shift in quantum electrodynamics, as discussed in [147].[6]

(ii) The direct dynamical interaction between the electron and the hole:

$$E^{(\tilde{N}\tilde{N}')}_{(NN')}(\mathbf{k}) = -\frac{1}{(2\pi)^2}\delta_{\tilde{\sigma}\sigma}\delta_{\tilde{\xi}\xi}\delta_{\tilde{\sigma}'\sigma'}\delta_{\tilde{\xi}'\xi'}\int \mathrm{d}\mathbf{q} e^{i\hat{\mathbf{z}}\cdot(\mathbf{q}\times\mathbf{k})l^2} I^{N\tilde{N}}_{N'\tilde{N}'}(\mathbf{q}). \tag{5.11}$$

This term is diagonal both in spin and pseudospin, but not in Landau orbital indices.

(iii) The exchange interaction between the electron and the hole:

$$R^{(\tilde{N}\tilde{N}')}_{(NN')}(\mathbf{k}) = \frac{1}{2\pi l^2}\delta_{\sigma\sigma'}\delta_{\xi\xi'}\delta_{\tilde{\sigma}\tilde{\sigma}'}\delta_{\tilde{\xi}\tilde{\xi}'}\mathrm{Re}I^{NN'}_{\tilde{N}\tilde{N}'}(\mathbf{k}), \tag{5.12}$$

which couples transitions that conserve the spin σ and the valley ξ of the electron and the hole individually. Sometimes we will call it the RPA contribution, as it is related to particle-hole annihilation and recreation processes.[7] Notice $R^{(\tilde{N}\tilde{N}')}_{(NN')}(\mathbf{k})$ vanishes in the $k \to 0$ limit.

We have used the notation

$$\begin{aligned} I^{N_2N_2'}_{N_1N_1'}(\mathbf{p}) = \quad & v(\mathbf{p})A^{(n_2')}_{\xi_2'}A^{(n_1)}_{\xi_1}A^{(n_1')}_{\xi_1'}A^{(n_2)}_{\xi_2}F^*_{|N_2||N_2'|}(\mathbf{p})F_{|N_1||N_1'|}(\mathbf{p}) \\ & +v(\mathbf{p})B^{(n_2')}_{\xi_2'}B^{(n_1)}_{\xi_1}B^{(n_1')}_{\xi_1'}B^{(n_2)}_{\xi_2}F^*_{|N_2|-2,|N_2'|-2,}(\mathbf{p})F_{|N_1|-2,|N_1'|-2}(\mathbf{p}) \\ & +v^D(\mathbf{p})A^{(n_2')}_{\xi_2'}B^{(n_1)}_{\xi_1}B^{(n_1')}_{\xi_1'}A^{(n_2)}_{\xi_2}F^*_{|N_2||N_2'|}(\mathbf{p})F_{|N_1|-2,|N_1'|-2}(\mathbf{p}) \\ & +v^D(\mathbf{p})B^{(n_2')}_{\xi_2'}A^{(n_1)}_{\xi_1}A^{(n_1')}_{\xi_1'}B^{(n_2)}_{\xi_2}F^*_{|N_2|-2,|N_2'|-2,}(\mathbf{p})F_{|N_1||N_1'|}(\mathbf{p}). \end{aligned}$$

infinity at infinitely far away from the Dirac cone.

[6]For monolayer graphene, a proper renormalization procedure is required, see [68], [146].

[7]It is also called the depolarization term in [141].

Here $N-2 \equiv (n-2,\xi,\sigma)$ and $|N| \equiv (|n|,\xi,\sigma)$. $v(\mathbf{p}) = e^2/(2\epsilon_0\epsilon_r p)$ is the Coulomb interaction within the layer, while $v^D(\mathbf{p}) = e^{-pd}v(\mathbf{p})$ is the interaction between the layers, where $d \approx 0.335$ nm is the distance between the layers. Due to the fact that d is much less than the magnetic length l we neglect the difference between the intralayer Coulomb interaction $v(\mathbf{p})$ and the interlayer one $v^D(\mathbf{p})$ in the following, and use $v(\mathbf{p})$ as an approximation. The form factor $F_{N'N}(\mathbf{q})$ is defined as

$$F_{N'N}(\mathbf{q}) = \delta_{\sigma\sigma'}\delta_{\xi\xi'}\sqrt{\frac{n!}{(n')!}}\left(\frac{(-q_y+iq_x)l}{\sqrt{2}}\right)^{n'-n} L_n^{n'-n}\left(\frac{q^2l^2}{2}\right)e^{-q^2l^2/4} \tag{5.13}$$

if $n' \geq n$, else $F_{NN'}(\mathbf{q}) = F^*_{N'N}(-\mathbf{q})$. Finally, notice that $A_\xi^{(n)}$ and $B_\xi^{(n)}$ has been introduced in Eq. 2.27 as the normalization amplitudes of the spinorial wave function of bilayer graphene. In the $u=0$ limit, as has been shown previously, they do not depend on the valley index ξ, only on the LL index n, and their values are $A_\xi^{(1)} = A_\xi^{(0)} = 1$, $B_\xi^{(1)} = B_\xi^{(0)} = 0$, and $A_\xi^{(n)} = \mathrm{sgn}(n)B_\xi^{(n)} = 1/\sqrt{2}$ for $n \geq 2$.

The mean-field Hamiltonian matrix element $H^{(\tilde{N}\tilde{N}')}_{(NN')}(\mathbf{k})$ determines how the bare Coulomb interaction mixes the dispersion relation of a pair of magnetoexcitons (NN') and $(\tilde{N}\tilde{N}')$. By diagonalizing the infinite $H^{(\tilde{N}\tilde{N}')}_{(NN')}(\mathbf{k})$ matrix we determine how the bare Coulomb interaction between, in principle, all magnetoexcitons is screened, in other words LL mixing effectively screens the interaction. Notice that the interaction is only restricted by conservation laws. In the $k \to 0$ limit the dispersion relation determines the many-body contribution to the cyclotron resonance, which may be nonvanishing in graphene systems, as has been discussed in Sec. 5.3 and Refs. [141] and [146]. At finite wave vector the mean-field theory with LL mixing removes spurious level crossings in the excitation spectra and provides insight into the orbital structure of the excitations.

The weakness of our approach that the infinite matrix $H^{(\tilde{N}\tilde{N}')}_{(NN')}(\mathbf{k})$ needs to be truncated. To eliminate this difficulty in Refs. [107] and [146] Misumi and Shizuya applied another method to approximate the strength of interaction: they used screened model interaction instead of the bare Coulomb, not letting LL transitions mix. We believe such an approach is only suitable in the $k=0$ limit, where an additional quantum number l_z also restricts LL mixing, and for intra-LL modes.

In the next section we consider numerous filling factors one after another and we

enumerate all possible magnetoexcitons and group them on the basis of their quantum numbers. We diagonalize a finite matrix $H^{(\tilde{N}\tilde{N}')}_{(NN')}(\mathbf{k})$ by letting only those magnetoexcitons with $l_z \leq L$ and LL index $n, n' \leq M$ mix. The exact values of L and M are determined empirically as discussed in the next section. To simplify the computations, we rely upon identities such as

$$E^{(\tilde{N}\tilde{N}')}_{(NN')}(\mathbf{k}) = E^{(NN')}_{(\tilde{N}\tilde{N}')}(\mathbf{k}) = E^{(\tilde{N}'\tilde{N})}_{(N'N)}(\mathbf{k}), \tag{5.14}$$

$$R^{(\tilde{N}\tilde{N}')}_{(NN')}(\mathbf{k}) = R^{(NN')}_{(\tilde{N}\tilde{N}')}(\mathbf{k}) = (-1)^{n+n'+\tilde{n}+\tilde{n}'} R^{(\tilde{N}'\tilde{N})}_{(N'N)}(\mathbf{k}), \tag{5.15}$$

which follow from the similar properties of $I^{N_2 N_2'}_{N_1 N_1'}(\mathbf{p})$.

5.5 Results and Discussion

5.5.1 Integer Quantum Hall States

We first consider the IQH states, which occur when the highest LL is fully filled. Here we aim to collect all possible excitations and group them using the relevant quantum numbers l_z, P_z, S_z, S^2 and P^2. The latter two are also good quantum numbers, since the possible ground states are spin and pseudospin singlet states.[8] For fixed LL orbitals (n' for the hole and n for the electron) 16 possible transitions exist, which belong to 4 classes:

- a one-member class with a spin singlet, pseudospin singlet state:

$$\hat{\Psi}^{\dagger 00}_{nn'}(\mathbf{k}) = \frac{1}{2} \sum_{\xi} \sum_{\sigma} \hat{\Psi}^{\dagger}_{n\sigma\xi, n'\sigma\xi}(\mathbf{k}). \tag{5.16}$$

- A three-member class with spin singlet, pseudospin triplet states. The $P_z = 0$ member of this multiplet is

$$\hat{\Psi}^{\dagger 01}_{nn'}(\mathbf{k}) = \frac{1}{2} \sum_{\xi} \sum_{\sigma} \mathrm{sgn}(\xi) \hat{\Psi}^{\dagger}_{n\sigma\xi, n'\sigma\xi}(\mathbf{k}). \tag{5.17}$$

[8] In the $\Delta_Z \to 0, u \to 0$ limit an SU(4) classification is also possible.

- A three-member class with spin triplet, pseudospin singlet, which contains the following $S_z = 0$ state:

$$\hat{\Psi}^{\dagger 10}_{nn'}(\mathbf{k}) = \frac{1}{2}\sum_{\xi}\sum_{\sigma}\mathrm{sgn}(\sigma)\hat{\Psi}^{\dagger}_{n\sigma\xi,n'\sigma\xi}(\mathbf{k}). \tag{5.18}$$

- A nine-member multiplet which is triplet in both spin and valley. Its $S_z = P_z = 0$ member is

$$\hat{\Psi}^{\dagger 11}_{nn'}(\mathbf{k}) = \frac{1}{2}\sum_{\xi}\sum_{\sigma}\mathrm{sgn}(\sigma)\mathrm{sgn}(\xi)\hat{\Psi}^{\dagger}_{n\sigma\xi,n'\sigma\xi}(\mathbf{k}). \tag{5.19}$$

Fig. 5.1 depicts the $S_z = P_z = 0$ modes for $\nu = -4$.

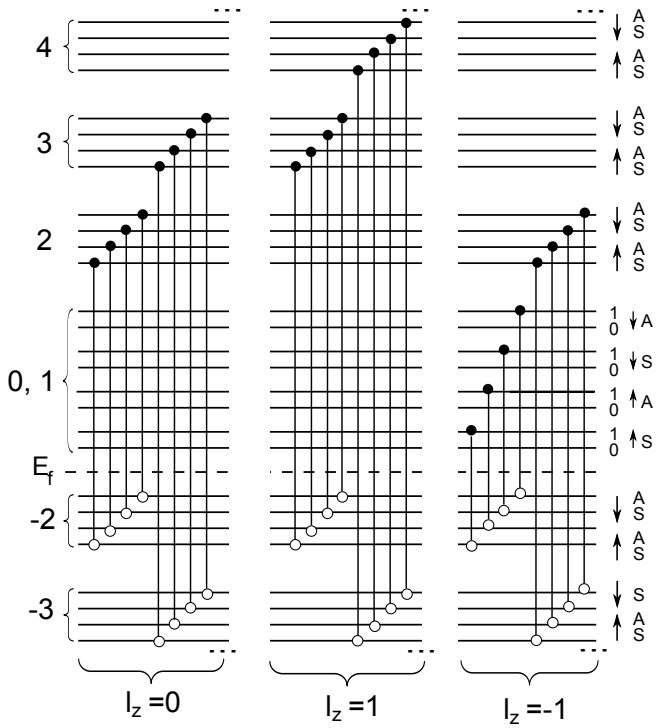

Figure 5.1: Magnetoexciton modes at the $\nu = -4$ IQHE in bilayer graphene. Only the optically relevant spin- and pseudospin-conserving modes are shown. In the $k \to 0$ limit, which is probed by purely optical experiments, the transitions in the infinite sequence at fixed $l_z = |n| - |n'|$ may mix; at $k > 0$, the excitations result from the mixing of all l_z sequences. The modes at $\nu = +4$ are obtained by particle-hole conjugation.

The exchange interaction or RPA term cancels or is prohibited by quantum numbers in all modes except the first class.[9] Thus in the absence of accidental degeneracies, we expect a collection of a nondegenerate excitation and one of 15-fold degenerate excitations; the latter is decomposed as $4, 7, 4$ if $\Delta_Z > 0, u = 0$ and as $1, 2, 1, 2, 3, 2, 1, 2, 1$ if $\Delta_Z, u > 0$ and $\Delta_Z \neq u$.

When truncating the infinite matrix $H^{(\tilde{N}\tilde{N}')}_{(NN')}(\mathbf{k})$ we allow the mixing of transitions restricted by $|l_z| \leq L$ and a maximum number M at each fixed l_z. Fig. 5.2 shows transitions at $|\nu| = 4$ with $L = 1$ and $M = 7$, while Figs. 5.3 and 5.4 show $|\nu| = 8$ and $|\nu| = 12$, with the same truncation in both cases. At $k = 0$ we have attempted an extrapolation of the excitation energies as a function of the cutoff M. The energies show a decreasing tendency, but fitting a power function has proven to be impossible, compare with [95]. We have chosen an ad-hoc cutoff at $M = 7$, with the understanding that small quantitative deviations are possible, especially at low energies. We have checked that using $M = 15$ does not fundamentally change the spectra. We use this truncation in all spectra shown in the rest of this chapter.

Interactions modify the single-body cyclotron resonance considerably both for $k = 0$ and for finite k. LL mixing eliminates level crossing and is especially strong for finite $kl \lesssim 1$, see e.g. Fig. 5.2. Panel (c) shows the projection of the excitations on different l_z subspaces. We emphasize that l_z is a good quantum number in the $k = 0$ limit. There the mean-field Hamiltonian mixes magnetoexcitons with different electron and hole LLs at fixed l_z, and for $k > 0$ it also mixes different l_z subspaces, thus the mixing cannot be restricted on a fixed l_z subspace. Apparently already the lowest excitations in the different l_z sectors mix strongly at finite wave vector, the excitations have a large projection on the l_z subspaces different from their own l_z in the $k \to 0$ limit, and may eventually be contained in one of the other subspaces for large k. This is an unavoidable consequence of the elimination of crossings by LL mixing. The mixing of LLs is especially strong in the nondegenerate excitations, which are strongly affected

[9]The RPA term cancels due sign alternation in modes $\hat{\Psi}^{\dagger 01}_{nn'}$, $\hat{\Psi}^{\dagger 10}_{nn'}$, and $\hat{\Psi}^{\dagger 11}_{nn'}$ One can easily check that the equal sign linear combination of the excitons created by the operators $(S\downarrow, S\uparrow)$ and $(A\downarrow, A\uparrow)$ is a pseudospin singlet, whereas the opposite sign linear combination is a member of a pseudospin triplet: Compare $P_-\hat{\Psi}^\dagger_{n\uparrow S, n'\uparrow S}|\mathrm{gs}\rangle$ with $\left(\Psi^\dagger_{n\uparrow S, n'\downarrow S} \pm \Psi^\dagger_{n\uparrow A, n'\downarrow A}\right)|\mathrm{gs}\rangle$, where P_- is the total pseudospin lowering operator and $|\mathrm{gs}\rangle$ is a ground state that is invariant for pseudospin rotation.

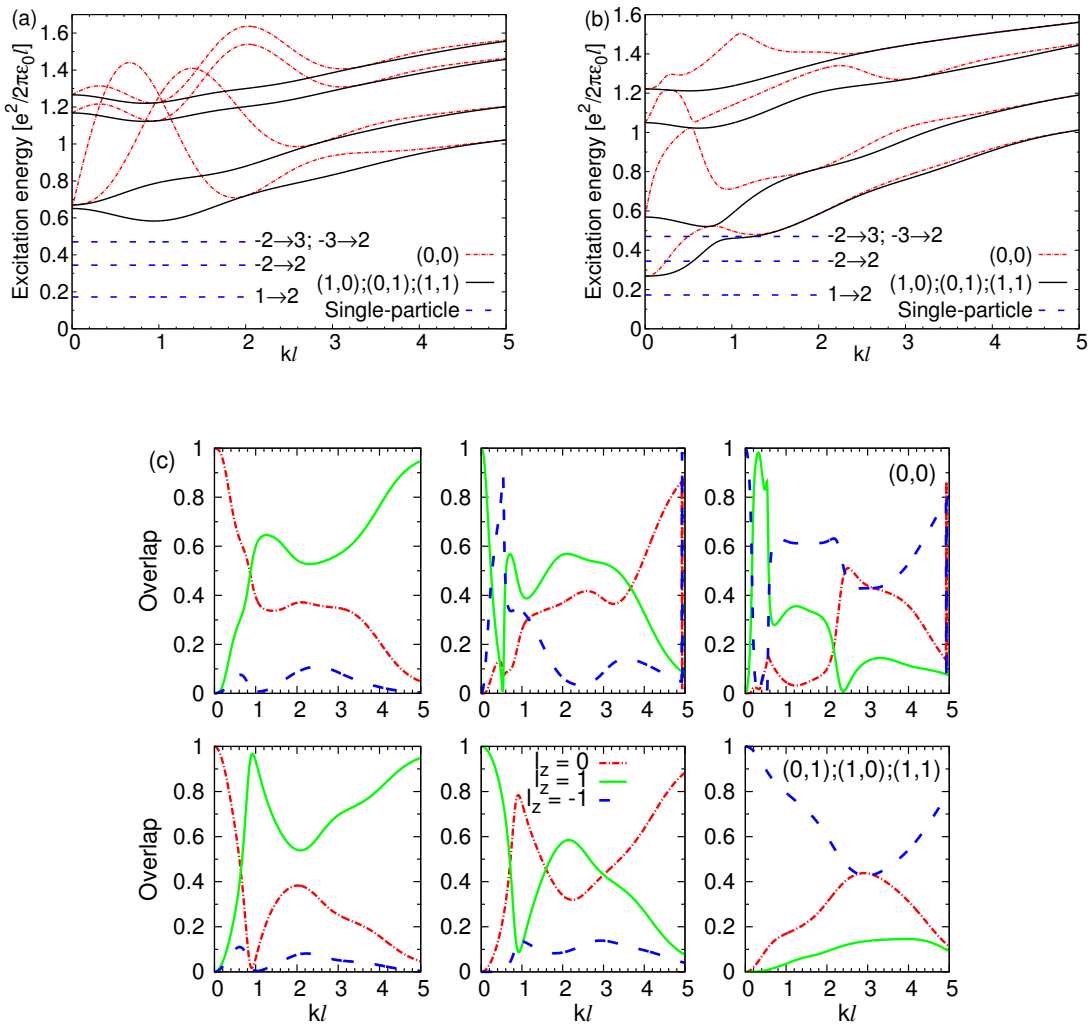

Figure 5.2: The excitations of the IQH state at $|\nu| = 4$ and $B = 10$T. Panel (a): spectra if LL mixing is neglected. Panel (b): The mixing of LLs is truncated at $L = 1$ and $M = 7$. Solid lines show the fifteen-fold degenerate excitations, which include three optically relevant $S_z = P_z = 0$ modes. Dashed-dotted lines show the spin and pseudospin singlets. Dashed lines depicts the single-body cyclotron resonance for the transitions indicated in the figure. Panel (c): the weight of the definite l_z projections in each curve in bottom-up order. The top row shows the spin and pseudospin singlets.

by the exchange interaction between the electron and the hole (the RPA term) in the $kl \sim 1$ region.

We also show the kinetic energy difference between the electron and the hole for comparison. Apparently, our mean-field theory predicts an interaction shift comparable to this energy. Evidently, this prediction shall be revisited with methods beyond mean-field, we delegate this project to future work.

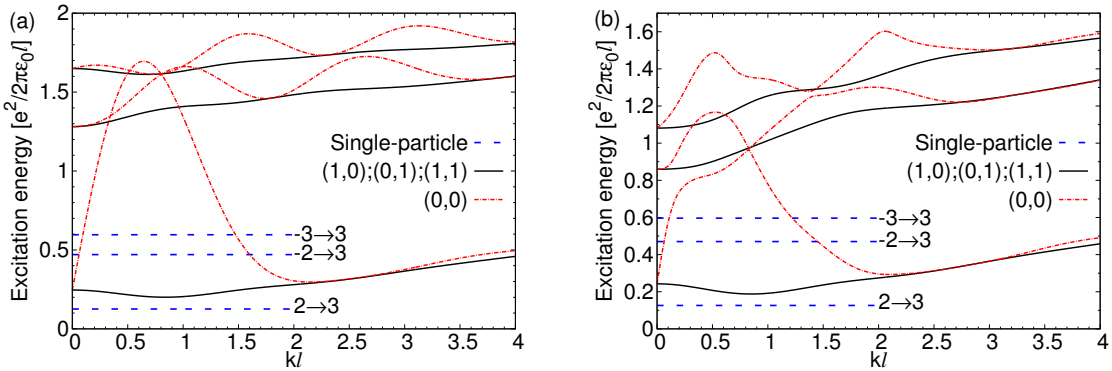

Figure 5.3: The excitations of the IQH state at $|\nu| = 8$ at $B = 10$T. Panel (a): spectra if LL mixing is neglected. Panel (b): spectra with LL mixing.

The $k \to 0$ limit of the magnetoexcitons is commonly probed by optical absorption and electronic Raman scattering. The selection rules discussed in [1] and [117] ensure that only the $\hat{\Psi}^{\dagger 00}_{nn'}$ mode and the $\hat{\Psi}^{\dagger 01}_{nn'}$, $\hat{\Psi}^{\dagger 10}_{nn'}$, and $\hat{\Psi}^{\dagger 11}_{nn'}$ modes of the 15-fold degenerate curve are active, $l_z = \pm 1$ in absorption, and $l_z = 0$ in Raman. In other words, the optically relevant modes are those conserving spin and valley pseudospin respectively.

5.5.2 Quantum Hall Ferromagnetic States

This subsection is devoted to QHF states, we investigate filling factors $\nu = 0, \pm 2, -3, 1$, see discussion in Sec. 5.2. As it was done previously, we collect the possible excitations and group them on the basis of their quantum numbers. S_z and P_z are good quantum numbers in all cases, the magnitude P^2 is only a good quantum number at half-filling $\nu = 0$. l_z is only applicable in the $k \to 0$ case, as previously.

All excitons include transitions between the non-central levels $|n| \geq 2$; the possibility of transitions from, to, or within the central LL octet depends on the ground

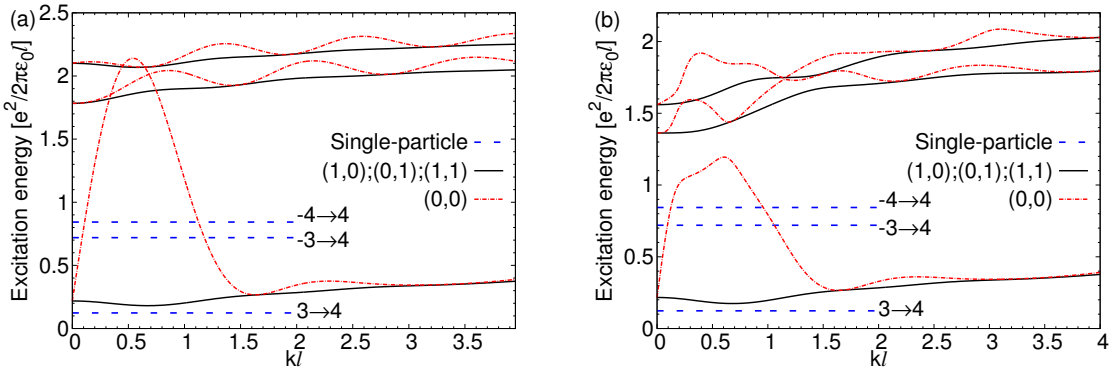

Figure 5.4: The excitations of the IQH state at $|\nu| = 12$, at $B = 10$T. Panel (a): spectra if LL mixing is neglected. Panel (b): spectra with LL mixing.

state. Note that the exchange self-energy differences play a crucial role in distinguishing various transitions.

Interesting to realize that not all excitations are optically active. For instance, valley flipping modes are inactive due to the small momenta of optical photons. In the $k \to 0$ limit l_z becomes a quantum number, and $l_z = \pm 1$ applies for single-photon absorption, and $l_z = 0, \pm 2$ in electronic Raman processes, with the $l_z = 0$ transitions being dominant. The angular momentum due to the helicity of the photons is transferred entirely to the orbital degree of freedom, see [1] and [117]. In this subsection we mostly deal with optically active modes, the inactive ones include Goldstone modes associated with the broken symmetry and generic dark modes. Goldstone modes are outside the scope of the present thesis, as discussed below.

$\nu = 0$

Table 5.2 contains the available excitations with the electron (n) and hole (n') LLs fixed.[10] The $S_z = -1$ transitions consist of a pseudospin triplet and a singlet. This

[10]Looking for the valley pseudospin triplet and singlet states, one can easily check by direct calculation that the triplet contains excitations created by the operators (A, S), and (S, A) and the opposite sign linear combination of (S, S) and (A, A), independently of the spin degree of freedom. The singlet is always the equal sign linear combination of the excitons (S, S) and (A, A). This is so because here the electron-hole pair is not an individual entity created from the vacuum state, but it can only be created from a QHF ground state $|\text{gs}\rangle$. Taking this into account, it is straightforward to deduce that $P_z = \pm 1$ excitations are pseudospin flip excitations and the P_- pseudospin lowering operator creates the opposite sign linear combination of (S, S) and (A, A), see $P_- \hat{\Psi}^\dagger_{S,S} |\text{gs}\rangle = \left(\Psi^\dagger_{S,S} - \Psi^\dagger_{A,A}\right) |\text{gs}\rangle$, where the latter state being the $P_z = 0$ member of the triplet.

	S_z	P^2	States
(i)	-1	1	$\Psi^\dagger_{nA\downarrow,n'S\uparrow}$, $\Psi^\dagger_{nS\downarrow,n'A\uparrow}$, $\frac{1}{\sqrt{2}}\left(\Psi^\dagger_{nS\downarrow,n'S\uparrow} - \Psi^\dagger_{nA\downarrow,n'A\uparrow}\right)$
(ii)	-1	0	$\frac{1}{\sqrt{2}}\left(\Psi^\dagger_{nS\downarrow,S\uparrow} + \Psi^\dagger_{nA\downarrow,A\uparrow}\right)$
(iii)	1	1	$\Psi^\dagger_{nA\uparrow,n'S\downarrow}$, $\Psi^\dagger_{nS\uparrow,n'A\downarrow}$, $\frac{1}{\sqrt{2}}\left(\Psi^\dagger_{nS\uparrow,n'S\downarrow} - \Psi^\dagger_{nA\uparrow,n'A\downarrow}\right)$
(iv)	1	0	$\frac{1}{\sqrt{2}}\left(\Psi^\dagger_{nS\uparrow,n'S\downarrow} + \Psi^\dagger_{A\uparrow,n'A\downarrow}\right)$
(v)	0	1	$\Psi^\dagger_{nA\uparrow,n'S\uparrow}$, $\Psi^\dagger_{nS\uparrow,n'A\uparrow}$, $\frac{1}{\sqrt{2}}\left(\Psi^\dagger_{nA\uparrow,n'A\uparrow} - \Psi^\dagger_{nS\uparrow,n'S\uparrow}\right)$, $\Psi^\dagger_{nA\downarrow,n'S\downarrow}$, $\Psi^\dagger_{nS\downarrow,n'A\downarrow}$, $\frac{1}{\sqrt{2}}\left(\Psi^\dagger_{nS\downarrow,n'S\downarrow} - \Psi^\dagger_{nA\downarrow,n'A\downarrow}\right)$
(vi)	0	0	$\frac{1}{\sqrt{2}}\left(\Psi^\dagger_{nS\uparrow,n'S\uparrow} + \Psi^\dagger_{nA\uparrow,n'A\uparrow}\right)$, $\frac{1}{\sqrt{2}}\left(\Psi^\dagger_{nS\downarrow,n'S\downarrow} + \Psi^\dagger_{nA\downarrow,n'A\downarrow}\right)$

Table 5.2: The available states at $\nu = 0$ with an electron (n) and hole (n') LL fixed.

group contains the intralevel transitions among the $n = 0, 1$ Landau bands; the Goldstone modes associated with the spin rotation symmetry breaking should be in this subspace. The $S_z = 1$ pseudospin triplet and singlet contain inter-LL transitions only. The $S_z = 0$ sector consists of two triplets (v), to which the RPA term does not contribute, and two singlets (vi), which are mixed by the RPA term. Careful inspection

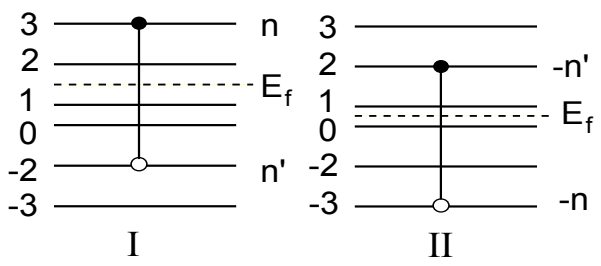

Figure 5.5: Imagine two transitions: (I) a particle in level n' is promoted to level n of a valley-spin component (left) of which the $n = 1$ Landau band is filled, and (II) $-n \to -n'$ of a component (right) of which the $n = 1$ band is empty. Particle-hole conjugation of (I) is the promotion of a hole from LL $-n'$ to $-n$, i.e., (II); the excitation energies must be the same. The consequence is Eq. 5.22; the formal proof is straightforward.

reveals, however, that the two pseudospin singlets (vi) always appear in the mean-field Hamiltonian on equal footing, e.g., the $\frac{1}{\sqrt{2}}\left(\Psi^\dagger_{2S\uparrow,1S\uparrow} + \Psi^\dagger_{2A\uparrow,1A\uparrow}\right)$ transition is indistinguishable on the mean-field level from the $\frac{1}{\sqrt{2}}\left(\Psi^\dagger_{1S\downarrow,-2,S\downarrow} + \Psi^\dagger_{1A\downarrow,-2,A\downarrow}\right)$ transition. This

follows by

$$E^{(2,1)}_{(2,1)} = E^{(1,-2)}_{(1,-2)}, \tag{5.20}$$

$$R^{(2,1)}_{(2,1)} = R^{(1,-2)}_{(1,-2)} = -R^{(1,-2)}_{(2,1)} = -R^{(2,1)}_{(1,-2)}, \tag{5.21}$$

and the following easily provable identity of the exchange self-energy cost:

$$\Delta(n, n') + X_{n'0} + X_{n'1} - X_{n,0} - X_{n,1} = \Delta(-n', -n). \tag{5.22}$$

(For $n = 1$ or $n' = 1$, no sign change is necessary.) Eq. 5.22 simply expresses particle-hole symmetry, i.e., that the exchange self-energy cost of transitions related by particle-hole conjugation in a fixed component must be identical. See Fig. 5.5 for the transitions whose comparison yields Eq. 5.22.

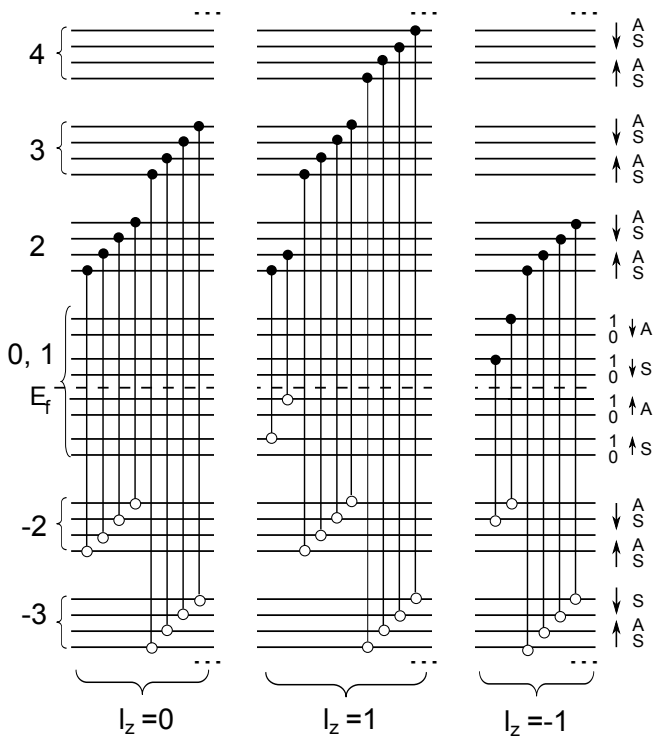

Figure 5.6: Magnetoexciton modes at the $\nu = 0$ QHF state in bilayer graphene. Only the optically relevant spin- and pseudospin-conserving modes are shown. In the $k \to 0$ limit, which is probed by photon absorption or electronic Raman, the transitions in the infinite sequence at fixed $l_z = |n| - |n'|$ may mix; at $k > 0$, the excitations result from the mixing of all l_z sequences.

The RPA terms are the same in each diagonal and off-diagonal position among

equivalent transitions, thus they select the even and the odd linear combinations in group (vi). The even combination, $\hat{\Psi}^{\dagger 00}_{nn'}(\mathbf{k})$ defined in Eq. 5.16, gets an RPA enhancement, while the RPA cancels from the alternating sign combinations, making it energetically equivalent to the $P_z = 0$ element of the triplets (v). Thus, eventually, the $S_z = 0, P_z = 0$ sector contains a threefold degenerate curve and a nondegenerate mode.

Each of the four multiplets in the $S_z = 0$ sector contains a $P_z = 0$ mode, which is active in electronic Raman or IR absorption. Here the mixing of LLs results in more widely separated modes. The optically active excitations are shown in Fig. 5.6, they are excitations (ii), (iv) and (vi).

The dispersion relation is shown in Fig. 5.7 with LL mixing taken into account. Notice that the $l_z = 1$ and $l_z = -1$ transitions have an equal weight in all modes, consistent with the particle-hole symmetry at $\nu = 0$.

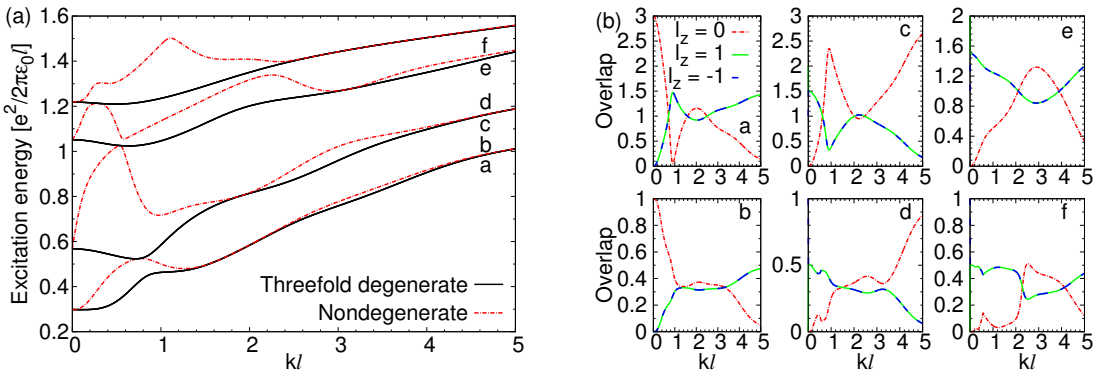

Figure 5.7: (a) Excitation spectra of the quantum Hall ferromagnet at $\nu = 0, \pm 2$ at $B = 10$T. Only the optically relevant $S_z = P_z = 0$ modes are included. (b) The weight of the shown excitations on the definite l_z subspaces for $\nu = 0$ in bottom-up order. For degenerate curves the weight is summed. The quantum numbers of the $k \to 0$ limit are for curve a: $0^3; 1^0; -1^0$, curve b: $0^1; 1^0; -1^0$, curve c: $0^0; 1^2; -1^1$, curve d: $0^0; 1^0; -1^1$, curve e: $0^0; 1^2; -1^1$; and finally curve f: $0^0; 1^0; -1^1$.

In the $S_z = -1$ sector we find spin waves. Neglecting LL mixing, they give rise to a gapless and a gapped intra-LL mode [166], and a sequence of higher inter-LL modes; each of these is raised by the Zeeman energy and split by the valley energy difference in turn. The interaction, however, mixes these excitations, thus a clear-cut classification into intra-LL and inter-LL is no longer possible. Level repulsion unavoidably lowers

the formerly gapless modes. This effect yields apparently negative excitation energies at small wavelength. Goldstone's theorem, however, ensures that a gapless spin-wave mode is associated with the breaking of the spin rotation symmetry. Consequently, the seemingly negative energy of the lowermost excitation with a large intra-LL component is an artifact of the combination of Hartree-Fock mean-field theory and LL mixing. We conclude that our approach is not appropriate for the description of Goldstone modes even at even filling factors. The same anomaly occurs for monolayer graphene in [68] and [95], but it is less apparent when the particle-hole binding energy is plotted.

$\boldsymbol{\nu} = \pm 2$

Fig. 5.8 shows the optically active transitions, which are spin and pseudospin preserving modes. In this subsection we restrict our discussion to these excitations. The $\nu = \pm 2$ states break the spin and pseudospin rotation symmetries as the ground state fills the $n = 0$ and $n = 1$ orbitals of the most favorable spin-pseudospin component, $S \uparrow$. Thus, only S_z and P_z are good quantum numbers.

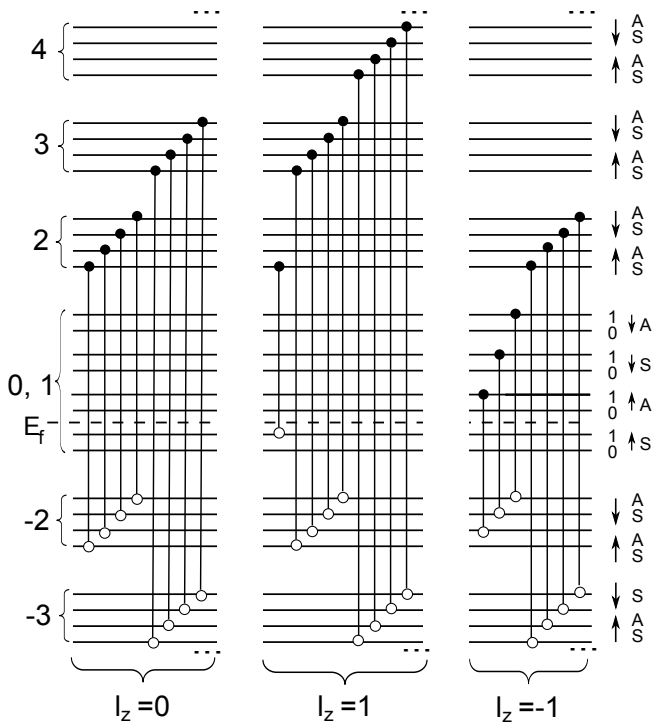

Figure 5.8: The spin- and pseudospin-conserving magnetoexciton modes at the $\nu = -2$ QHF state in bilayer graphene. The modes at $\nu = +2$ are obtained by particle-hole conjugation.

It is easy to check that the mean-field Hamiltonian matrix is identical to the one at $\nu = 0$. For the $-n \to n$ transitions ($n \geq 2$ integer) this holds because the occupancy of the central LL octet is irrelevant as

$$X_{-n,0} + X_{-n,1} - X_{n,0} - X_{n,1} = 0. \tag{5.23}$$

The octet of $-(n+1) \to n$ and $-n \to (n+1)$ transitions gives rise to two quartets of equivalent transitions by Eqs. 5.20-5.22. While at $\nu = 0$ the $S\uparrow$ and $A\uparrow$ transitions of the former group bundle with the $S\downarrow$ and $A\downarrow$ transitions of the second group, now the $S\uparrow$ transition of the first group bundles with the $A\uparrow$, $S\downarrow$, and $A\downarrow$ transitions of the second group. The spectrum is identical with the one in Fig. 5.7(a). The orbital projection of the modes differs and is shown in Fig. 5.9 for $\nu = -2$. At $\nu = +2$ the sign of l_z changes in all projections, which determines the helicity of the absorbed and inelastically scattered photons.

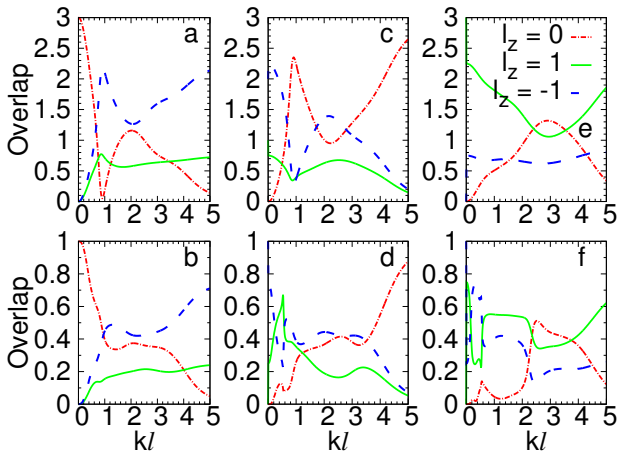

Figure 5.9: The projection of the excitations at $\nu = -2$ on the definite l_z subspaces. For degenerate curves the weight is summed. The spectrum at $\nu = \pm 2$ is identical to the one in the left panel of Fig. 5.7, the letters refer to the same curves. For $\nu = +2$ the sign of the $+l_z$ and $-l_z$ projections are interchanged w.r.t. $\nu = -2$. The quantum numbers of the $k \to 0$ limit are for curve a: $0^3; 1^0; -1^0$, curve b: $0^1; 1^0; -1^0$, curve c: $0^0; 1^1; -1^2$, curve d: $0^0; 1^0; -1^1$, curve e: $0^0; 1^3; -1^0$; and finally curve f: $0^0; 1^0; -1^1$.

$\nu = -3$

Here we only deal with the optically relevant spin and valley pseudospin conserving modes, see Fig. 5.10. At $\nu = 0$, the $n = 0$ orbital is filled with $S \uparrow$ electrons in the

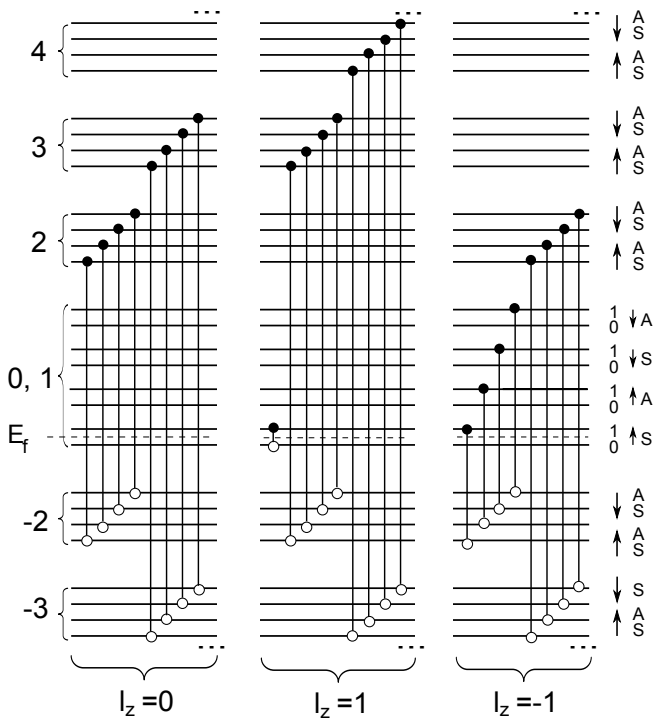

Figure 5.10: The optically spin- and pseudospin-conserving magnetoexciton modes at the $\nu = -3$ QHF state in bilayer graphene. Notice that the $S \downarrow$, $A \uparrow$ and $A \downarrow$ transitions occur symmetrically, i.e., the same electron and hole LLs are allowed and the same self-energy cost is picked up from the exchange with the filled levels.

mean-field ground state, thus for fixed electron (n) and hole (n') LLs the exchange self-energy cost of the $S \uparrow$ transition is higher than those of the other components. Also, in the $S \uparrow$ component an intralevel $0 \to 1$ transition is possible, which mixes with higher $S \uparrow$ transitions. The other three components, on the other hand, occur symmetrically in the mean-field Hamiltonian. One can change basis from the excitons

of type $S\downarrow$, $A\uparrow$ and $A\downarrow$ to

$$\hat{\Psi}^{\dagger d1}_{nn'} = \frac{1}{\sqrt{2}}\left(\Psi^{\dagger}_{nA\uparrow,n'A\uparrow} - \Psi^{\dagger}_{nA\downarrow,n'A\downarrow}\right), \tag{5.24}$$

$$\hat{\Psi}^{\dagger d2}_{nn'} = \frac{1}{\sqrt{6}}\left(\Psi^{\dagger}_{nA\uparrow,n'A\uparrow} + \Psi^{\dagger}_{nA\downarrow,n'A\downarrow} - 2\Psi^{\dagger}_{nS\downarrow,n'S\downarrow}\right), \tag{5.25}$$

$$\hat{\Psi}^{\dagger r}_{nn'} = \frac{1}{\sqrt{3}}\left(\Psi^{\dagger}_{nA\uparrow,n'A\uparrow} + \Psi^{\dagger}_{nA\downarrow,n'A\downarrow} + \Psi^{\dagger}_{nS\downarrow,n'S\downarrow}\right). \tag{5.26}$$

The RPA contribution cancels from $\hat{\Psi}^{\dagger d1}_{nn'}(\mathbf{q})$ and $\hat{\Psi}^{\dagger d2}_{nn'}(\mathbf{q})$, which gives rise to doubly degenerate excitations. $\hat{\Psi}^{\dagger r}_{nn'}(\mathbf{q})$ has an RPA contribution. Its mixture with the distinguished $S\uparrow$ excitations produces nondegenerate curves. It is evident from Fig. 5.11(a), where we show the dispersion of the active excitations. In higher-energy excitations, on the other hand, the weight of the $0 \to 1$ transition of the $S\uparrow$ component becomes extremely small, thus the equivalence of the four components will be approximately restored, yielding threefold quasi-degenerate and nondegenerate curves, see also Fig. 5.11(a).

Fig. 5.11(b) shows that the projection to definite l_z subspaces changes abruptly at non-zero wave vector. Notice that at higher energies $\gtrsim e^2/(4\pi\epsilon_0\epsilon_r l)$ the doubly degenerate curves occur in the vicinity of a nondegenerate one, indicating the approximate restoration of the equivalence of components in this limit.

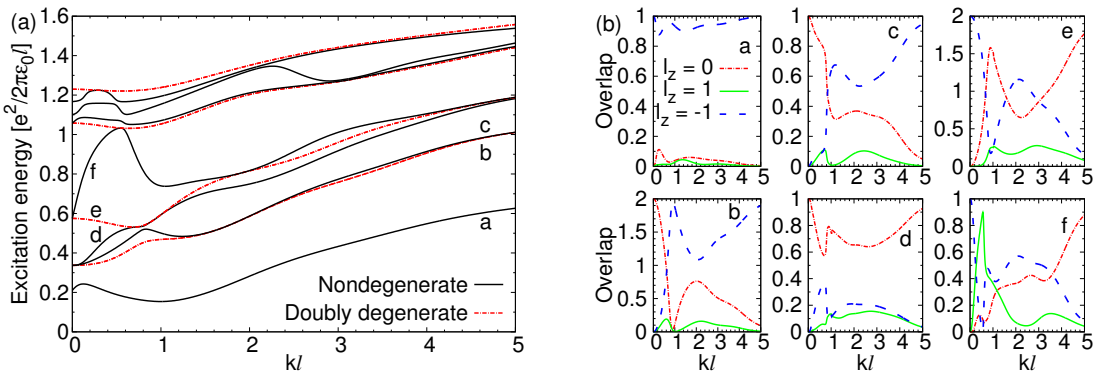

Figure 5.11: (a) Excitation spectrum of the quantum Hall ferromagnet in the $\nu = -3$ at $B = 10$T. Only the optically relevant $S_z = P_z = 0$ modes are included. (b) The weight of the shown excitations on the definite l_z subspaces in bottom-up order. For degenerate curves, the weight is summed.

Because of the degeneracy of $n = 0, 1$ orbitals, states in central LL octet at odd

integer fillings involve fluctuations with in-plane electric dipole character [9]. The consequent collective modes have been studied in detail by Barlas *et al.* in [10] and Côté *et al.* in [31]. As we do not handle such dipolar interactions, we have omitted the predominantly intra-LL lowest curve from the spectra, and we have checked that the inter-LL excitation modes we keep contain the $0 \to 1$ magnetoexcitons with a negligible weight. Reassuringly, we always got a weight less than 0.1%.

$\nu = 1$

As previously we only deal with optically active modes, the possible transitions in the mean-field Hamiltonian are obtained trivially by raising the Fermi level by four levels in Fig. 5.10.

The ground state at $\nu = 1$ is the particle-hole conjugate pair of the ground state at $\nu = -3$ discussed in the previous subsection. Now the $S \downarrow$ electrons are distinguished by the possibility of an intralevel $0 \to 1$ transition, and their higher self-energy. The other three components occur symmetrically in the mean-field Hamiltonian. The argument is similar to the case of $\nu = -3$; for the two $1 \to 2$ transitions of spin $\uparrow$ electrons and the $-2 \to 1$ transitions of the spin $\downarrow$ electrons, one uses $R^{(2,1)}_{(1,0)} = -R^{(1,-2)}_{(1,0)}$ and Eq. 5.22. When subsequent $l_z = \pm 1$ transitions are included, the $-n \to (n+1)$ transition of $A \downarrow$ is equivalent to the $-(n+1) \to n$ transition of $S \uparrow$ and $A \uparrow$, while the $-n \to (n+1)$ transition of $A \uparrow$ and $S \uparrow$ is equivalent to the $-(n+1) \to n$ transition of $A \downarrow$. The convenient basis change is similar to Eqs. 5.24 to 5.26, with $S \uparrow$ replaced by $A \downarrow$.

There is only a slight difference between the inter-LL excitation spectra at $\nu = -3$ and $\nu = 1$: the exchange self-energy cost of the distinguished transition ($S \uparrow$ at $\nu = -3$ and $S \downarrow$ at $\nu = 1$) relative to the three equivalent ones is $X_{n'0} - X_{n0}$ at $\nu = -3$ and $X_{n'1} - X_{n1}$ at $\nu = 1$. As this difference is already small for the lowest transitions and then decreases, we omit the $\nu = 1$ spectrum; its difference from Fig. 5.11(a) is comparable to the line width.

5.6 Conclusion

We have calculated the inter-LL magnetoexcitons in the IQH states as well as the quantum Hall ferromagnets at filling factors $\nu = -3, \pm 2, 0, 1$ of bilayer graphene. We have found that the spinorial structure of the orbitals together with the enhanced electron-hole exchange interaction effects in this multicomponent system gives rise to rather complex dispersions; these are related both to the shape of the Fourier transform of Landau orbitals and to the elimination of crossings by the mixing of LLs, which is significant because the scale of the Coulomb energy is comparable to the cyclotron energies.

On the theory side, we have found that the classification of magnetoexciton modes at finite wave vectors by the *angular momentum quantum number* is problematic, and that the screening effects, which we have handled via LL mixing, are significant. We have proven that the inclusion of screening is necessary to the proper understanding of the collective modes in bilayer graphene.

Our theoretical predictions may be probed by various optical experiments. On the one hand, optical absorption and electronic Raman experiments are readily available to probe the $k \to 0$ limit of the excitation, see [1], [43] and [117]. Unlike for the 2DEG with a quadratic dispersion, where Kohn's theorem applies, in the case of bilayer graphene the excitations in a quantizing magnetic field do acquire an interaction shift; the magnitude of such a shift is one of our experimental predictions. On the other hand, the wave vector dependence of the magnetoexcitons can be probed in resonant inelastic light scattering experiments of Ref. [134], where momentum conservation breaks down mainly because of ineffectively screened charged impurities. In semiconducting samples this technique has been successfully applied to the study of, for instance, spin-conserving and spin-flipping excitations at integer filling factors, the long wavelength behavior of the low-lying and higher excitations of fractional quantum Hall states and the magnetoroton minima both at integer and fractional fillings, see Refs. [40], [73], [132], [133], [134], [139]. In graphene, the magnetophonon resonance was observed by this method [175]. The mixing of transitions that involve different LLs is strong in the experimentally accessible range. This mixing smoothens the dis-

persion relations via level repulsion, and at finite wavelength causes a strong mixing of the modes that have different angular momenta in the zero-wave vector limit. In particular, we have found that the anticrossings due to LL mixing result in a number of undulations in the magnetoexciton dispersions, whose van Hove singularities must give a strong signal, see [134].

Nonetheless, it is unavoidable to extend our calculations (i) to include the finite u range, note that in Ref. [17] this issue is partially discussed, and (ii) to properly include orbitally-coherent ground states. Recently, Lambert *et al.* in Ref. [88] have determined the collective excitations for intra-LL transitions using generalized random phase approximation for $\nu \in [-3, 3]$ in the finite u range. We believe that after the proper reconsideration of their results (see our comments below) merging them with ours readily gives a comprehensive picture of the collective excitations of bilayer graphene.

As a final remark, we emphasize that our calculations presented in this chapter are based on the ground states determined by Barlas *et al.* in Refs. [9] and [10] and explained in Sec. 5.2 in detail. On the basis of the Hund's rule presented in Table 5.1 particle-hole symmetry connects QHF states at $\nu = \pm 3$ and ∓ 1, which is rather counterintuitive, as the particle-hole symmetry of the unerlying Hamiltonian is broken. Recently, Shizuya in Ref. [147] has shown that in order to correctly identify the QHF ground states the exchange interaction with all filled LLs should be properly taken into account, the projection of the exchange field on the central Landau octet, commonly used previously in Refs. [9] and [10], is insufficient. Extending Shizuya's calculations Tőke in Ref. [167] determined the QHF ground states for filling factors $\nu = \pm 3, \pm 2, \pm 1, 0$ using standard mean-field decomposition of the interaction, showing the crucial role played by the exchange (Fock) term. In the case of even filling factors, Hund's rule is proven to be correct, however for odd fillings the exchange field favours orbitally-coherent states. In has been also revealed that above a certain interaction strength, a pair of ground state manifolds (called bifurcation) appears, which is an orbitally- coherent state, but not layer-coherent any more, charges are distributed on the sublattices differently.[11] Reassuringly, the particle-hole symmetry of the underlying

[11] We note that similar considerations are valid for trilayer and multilayer graphene, as detailed in

Hamiltonian is preserved in all cases. Apparently, the reconsideration of the excitations at odd filling factors using the orbitally-coherent ground states is inevitable and is delegated to future work.

Refs. [148] and [167].

New Scientific Results

1. I have solved the eigenvalue problem of α-(BEDT-TTF)$_2$I$_3$ in a perpendicular magnetic field making use of the relativistic covariant nature of the underlying Dirac equation, assuming the material is under high hydrostatic pressure or uniaxial strain, that is, the zero-gap state phase is realized. I have drawn a parallel between the zero-gap state phase of α-(BEDT-TTF)$_2$I$_3$ and graphene in a crossed magnetic and in-plane electric fields and I have pointed out that the electric field in the latter system and the tilt in the former one play essentially the same role, leading to identical Landau states in both systems [III].

2. Handling graphene in a crossed magnetic and electric fields and α-(BEDT-TTF)$_2$I$_3$ in a magnetic field together I have calculated the frequency dependence of the absorption coefficient. Considering circularly polarized light, I have determined the matrix elements and I have found that besides the dipolar optical transitions $\propto \delta_{|n|,|n|\pm 1}$, a plethora of other optical transitions are possible due to rotational symmetry breaking. I have analyzed the internal structure of the emerging novel transitions and I have demonstrated using Fourier transformation that it leads to an oscillatory behaviour of the high-frequency tail of the absorption coefficient, which might be measurable in both systems. I have proposed a procedure to deduce experimental value for the tilt parameter β and the tilt direction θ_{tilt} in α-(BEDT-TTF)$_2$I$_3$ [III].

3. I have determined the collective excitations of α-(BEDT-TTF)$_2$I$_3$ in its zero-gap state phase in a perpendicular magnetic field within the random phase approximation. I have calculated the frequency-dependent dielectric function and the density-density response function assuming the presence of both massive and massless carriers in the low-energy band structure. I have identified the linear magnetoplasmons

of the linear and the upper-hybrid modes of both types of valleys and discussed their angular dependence. I have demonstrated that by magnetic field and doping one can tune the system between a case where only the linear valleys contribute to the density-density response and a case where all three valleys contribute. I have discovered that in an electron-doped case the angular dependence leads to a unique, anisotropic damping between the valleys: the particle-hole excitations of one valley damp the plasmonic mode of the other valley, even though the latter is in its proper forbidden region. I have pointed out that in a hole-doped case the massive band dominates the collective excitations of the system, and it also participates in the damping processes among the valleys. I have analyzed how doping can effectively tune the system between isotropic and anisotropic screening regimes [II].

4. I have calculated the magnetoexciton dispersion relation of bilayer graphene in a perpendicular magnetic field in a mean-field picture. I have identified three terms that appear besides the single-body energy difference: first, the exchange self-energy difference of the two states involved, second, the direct dynamical interaction between the electron and the hole and, finally, the exchange interaction between the electron and the hole. I have enumerated the possible magnetoexcitons both in the integer quantum Hall regime, where the highest Landau level is fully filled, and in cases with other integer filling factors that correspond to symmetry-breaking quantum Hall ferromagnetic states. I have demonstrated that the cyclotron resonance is modified considerably by the inclusion of the Coulomb interaction both in the $k \to 0$ limit, as Kohn's theorem does not apply in the case of bilayer graphene, and at finite wave vector. I have also pointed out that Landau level mixing leads to the elimination of level crossings, and that the mixing of transitions is especially strong in the intermediate k range, which is accessible experimentally by inelastic light scattering [I].

List of Publications

[I] J. Sári and C. Tőke, Phys. Rev. B **87**, 085432 (2013).

[II] J. Sári, C. Tőke, and M. O. Goerbig, Phys. Rev. B **90**, 155446 (2014).

[III] J. Sári, M. O. Goerbig, and C. Tőke, Phys. Rev. B **92**, 035306 (2015).

Összefoglalás

Bevezetés

Az elmúlt évtizedben soha nem látott fejlődés játszódott le a kétdimenziós és kvázi-kétdimenziós anyagi rendszerek kutatásának területén, elsősorban az egyrétegű grafén 2005-beni felfedezésének köszönhetően, [122], [183]. A grafén újszerűsége kétdimenziós természetében gyökerezik, és számos különleges tulajdonsághoz vezet, mint például a lineáris völgyek megjelenése az alacsony energiás sávszerkezetben, vagy az anomális kvantum Hall effektus. A grafén elektronjai kielégítik a tömeggel nem rendelkező részecskékre vonatkozó Dirac egyenletet, habár a fénysebességnél nagyságrenddel alacsonyabb Fermi sebességgel, mégis, ez a tény adhat alapot a Dirac elektronok elnevezésre, valamint ebben a kontextusban nyer értelmet a Dirac-kúpok elnevezés is.

A grafén első izolációja utat nyitott számos más kétdimenziós anyag felfedezésének, így hamarosan azonosításra került a kétrétegű grafén, [123], amelynek alacsony energiás sávszerkezete a grafénnel ellentétben parabolikus, illetve más réteges szerkezetű kétdimenziós anyagok, [38], [106], [138], [165], [171], [170] és [177]. Mindezek mellett, épp a grafén kapcsán erősödött meg olyan anyagi rendszerek iránt az érdeklődés, legyenek akár háromdimenziós kristályok, amelyeknek alacsony energiás sávszerkezetében Dirac-kúpok alakulnak ki. Ezen kristályok csoportjába tartozik a kvázi-kétdimenziós modellel leírható szerves kristály, az α-(BEDT-TTF)$_2$I$_3$ is, melyben a Dirac-kúpok nagy nyomáson vagy mechanikai feszültség hatására jelennek meg [118], [160], [161].

Ugyan lenyűgöző a fejlődés a kétdimenziós anyagok vizsgálatának területén, észre kell vennünk, hogy számos kérdés mind a mai napig megválaszolatlan. Így például, az α-(BEDT-TTF)$_2$I$_3$ esetén, amelynek Dirac-kúpjai a grafénnel ellentétben dőltek és anizotropok [81], [82], [112], egyes elméleti és kísérleti eredmények szerint a lineáris

völgyek mellett parabolikus völgy is található az első Brillouin zónában [3], [111], ez utóbbi állítás azonban rendkívül vitatott, s más kísérletekben nem nyert megerősítést [163]. A grafén vagy kétrétegű grafén esetén a kölcsönhatási effektusok vizsgálata tartogathat még új felfedezéseket, hasznos áttekintést ad a témáról [11], [86] és [54]. Mindezen megfontolások alapján hisszük, hogy a kvázi-kétdimenziós anyagi rendszerek vizsgálata időszerű, és számos új eredménnyel kecsegtet.

Áttekintés, az értekezés felépítése

Jelen értekezés kvázi-kétdimenziós elektronrendszerek egyrészecskés és kollektív gerjesztéseit vizsgálja merőleges mágneses térben, az egész számú kvantum Hall tartományban, illetve olyan mágneses tereknél, ahol kvantum Hall ferromágneses állapotok jelennek meg. Kutatásunk kiterjed egyrétegű, kétrétegű grafénre, valamint az α-(BEDT-TTF)$_2$I$_3$-re.

Az 1. fejezetben rövid áttekintést adunk a kétdimenziós, illetve kvázi-kétdimenziós anyagi rendszerekre vonatkozó legfrissebb kutatási eredményekről, rávilágítva azokra az újszerűségekre, amelyek a terület intenzív fejlődését motiválják.

A 2. fejezetben bővebben tárgyaljuk a dolgozat további részében vizsgált anyagok legfőbb, a dolgozat szempontjából releváns tulajdonságait, így levezetjük az egyrétegű és kétrétegű grafén, valamint egy szerves kristály, az α-(BEDT-TTF)$_2$I$_3$ Landau spektrumát, illetve a kapcsolódó hullámfüggvényeket. A fejezet azonban nem csak az irodalomból ismeretes eredmények gyűjteménye. Megmutatjuk, hogy a grafénhez hasonlóan [96] a szerves félvezető α-(BEDT-TTF)$_2$I$_3$ esetén is a Dirac egyenlet kovarianciája kihasználható a Landau spektrum és a hullámfüggvények meghatározására, s a mágneses térbe helyezett α-(BEDT-TTF)$_2$I$_3$ és a merőleges mágneses és síkban fekvő elektromos térbe helyezett grafén között párhuzam vonható.

A 3. fejezetben az előbbi két anyagi rendszert vizsgáljuk tovább, meghatározva magneto-optikai tulajdonságaikat. A köztük lévő analógiát használva közös formalizmus építhető ki az abszorpciós együtthatóra. A rotációs szimmetria sérülése, amit a dőlés és az elektromos tér okoz az egyik és a másik rendszerben, mindkét esetben dőlt Dirac-kúpokhoz vezet. Ha merőleges mágneses teret kapcsolunk be, akkor a rotációs

szimmetria sérülése új optikai átmenetek egész sorának megjelenését eredményezi. A fejezet jelentős részét ezen megjelenő átmenetek szerkezetének vizsgálata teszi ki, s annak megmutatása, hogy mindez hogyan tükröződik az abszorpciós együtthatóban.

A 4. fejezetben szintén a mágneses térbe helyezett α-(BEDT-TTF)$_2$I$_3$ áll a középpontban, a fejezet az alacsony energiás kollektív gerjesztések meghatározását tűzi ki célul. A közelmúltbeli *ab initio* számolásokra, Ref. [3], és kísérleti eredményekre, Ref. [111], építve olyan sávszerkezet modellt vizsgálunk, amelyben az egymás irányába dőlő Dirac-kúpok mellett egy tömeggel rendelkező völgy is megjelenik. Célunk tehát egyrészt kiterjeszteni a két Dirac-kúpra vonatkozó, mágneses tér nélküli számolásokat, [120], [121], mágneses tér jelenlétére, másrészt megvizsgálni, hogy az alacsony energiás sávszerkezetben megjelenő, tömeggel rendelkező elektronok hogyan módosítják a pusztán Dirac-kúpokat feltételező modellel kapott sűrűség-sűrűség válaszfüggvényt és a frekvenciafüggő dielektromos függvényt.

Az utolsó fejezetben kétrétegű grafént vizsgálunk, a korábbiakhoz hasonlóan merőleges mágneses térben, egész betöltési számok esetén. Külön tárgyaljuk a $\nu = \pm 4, \pm 8, \pm 12, ...$ betöltési számok esetét, amikor a legfelső Landau szint teljesen betöltött, valamint az egyéb egész betöltési számokat, amikor szimmetriasértő kvantum Hall ferromágneses alapállapotok alakulnak ki, kölcsönhatási effektusok következtében. A különbségek ellenére mindkét eset elemi gerjesztései magnetoexcitonok, amelyeket egy betöltetlen állapotba gerjesztett elektron és a betöltött szinten maga után hagyott lyuk alkot. Átlagtér közelítésben meghatározzuk a magnetoexcitonok diszperziós relációját árnyékolatlan Coulomb kölcsönhatással, majd a magnetoexcitonok keveredését is megengedve keressük az alapállapotot; ahol a magnetoexcitonok keveredésével az excitonok egymás közötti árnyékolását vesszük figyelembe. A fejezet megvizsgálja, hogy egyrészt $k \to 0$ határesetben, másrészt véges hullámszám vektorok esetén hogyan módosul a magnetexcitonok diszperziós relációja.

Tézispontok

1. Megoldottam az α-(BEDT-TTF)$_2$I$_3$ sajátérték, sajátvektor problémáját merőleges mágneses térben az anyag azon nagy nyomású fázisában, amelyben Dirac-kúpok

jelennek meg az alacsony energiás sávszerkezetben. A levezetésnél kihasználtam a kapcsolódó Dirac egyenlet relativisztikusan kovariáns alakját, s párhuzamot vontam ezen szerves félvezető és a grafén között, ha utóbbit az anyag síkjára merőleges mágneses térbe és síkban fekvő elektromos térbe tesszük. Rámutattam, hogy az elektromos tér grafénben és a Dirac-kúpok dőlése a szerves félvezető sávszerkezetében ugyanazt a szerepet játsza, s mind a két anyag esetén azonos Landau állapotok kialakulásához vezet [III].

2. Az előbbi párhuzamot kihasználva meghatároztam az abszorpciós együtthatót egyazon formalizmussal mind az α-(BEDT-TTF)$_2$I$_3$ magas nyomású fázisára mágneses térben, mind grafénre merőleges mágneses és síkbeli elektromos terekben. Meghatároztam a perturbatív mátrixelemeket cirkulárisan poláros beeső fény esetén. Megmutattam, hogy a forgási szimmetria sérülése miatt a grafénben mágneses tér jelenlétében lehetséges $\propto \delta_{|n|,|n|\pm 1}$ átmeneteken kívül új átmenetek sora válik megengedetté. Megvizsgáltam az újonnan megjelenő átmenetek szerkezetét, s Fourier transzformáció segítségével megmutattam, hogy az átmenetek speciális mintázata az abszorpciós együttható oszcilláló viselkedéséhez vezet magas frekvenciákon. Ezen oszcillációk mind grafén, mind α-(BEDT-TTF)$_2$I$_3$ esetén mérhetőek, javaslatot tettem arra, hogy az utóbbi anyagnál ez az oszcilláló viselkedés hogyan használható ki a dőlést jellemző β paraméter és a dőlés szögét megadó θ_{tilt} meghatározására [III].

3. Meghatároztam az α-(BEDT-TTF)$_2$I$_3$ kollektív gerjesztéseit az anyag magas nyomású fázisában mágneses térben véletlen fázis közelítésben. Kiszámoltam a frekvenciafüggő dielektromos függvényt és a sűrűség-sűrűség válaszfüggvényt egy olyan sávszerkezet modellt feltételezve, amelyben a Dirac-kúpok mellett egy parabolikus völgy is található a Brillouin zónában. Beazonosítottam a lineáris magnetoplazmonokat a lineáris völgyekben és a plazmon módusokat mind a lineáris, mind a parabolikus völgyekben; megvizsgáltam a lineáris völgyek anizotrópiájának hatását a kialakuló kollektív módusokra. Megmutattam, hogy mágneses tér vagy a Fermi energia hangolásával a rendszer válasza változtatható: ha a Fermi energia a Dirac pont feletti értékre hangolt, akkor csak a lineáris völgyek, ha a Dirac pont alá hangolt, akkor mind a három völgy hozzájárul a rendszer válaszához. Megvizsgáltam,

hogy az előbbi esetben miként vezet a lineáris völgyek anizotrópiája a kollektív gerjesztések egy sajátos, a völgyek között létrejövő csillapodásához: az egyik völgy részecske-lyuk gerjesztései akkor is leárnyékolják a másik völgy plazmon-módusát, ha az a saját tiltott tartományába esik. Megmutattam továbbá, hogy az utóbbi esetben a völgyek közötti csillapodásban a parabolikus völgy is részt vesz, s ez adja a rendszer teljes válaszának jelentős részét. Kitértem arra is, hogy a Fermi energia hangolása hogyan befolyásolja az árnyékolást: a parabolikus völgy által dominált, izotrop árnyékolás a Fermi energia növelésével a lineáris völgyek által meghatározott, anizotrop módon árnyékolt tartományba vihető [II].

4. Kiszámoltam a magnetoexcitonok diszperziós relációját kétrétegű grafén esetén átlagtér közelítésben. Beazonosítottam az energiában az egyrészecskés energiakülönbségen kívül megjelenő három tagot, ezek egyrészt, a részecskének és a lyuknak a betöltött állapotokkal vett kicserélődési energiájának különbsége, másrészt a direkt dinamikai kölcsönhatás a két részecske között, végül a két részecske közötti kicserélődési kölcsönhatás. Számba vettem a lehetséges magnetoexcitonokat egész betöltési számok esetén: egyrészt kvantum Hall tartományban, amikor a legfelső Landau szint teljesen betöltött, másrészt egyéb, egész betöltési számok esetén, amikor szimmetriasértő kvantum Hall ferromágneses állapotok alakulnak ki. Megmutattam, hogy a Coulomb kölcsönhatás figyelembe vétele jelentősen módosítja a Landau szintek energiáját mind a $k \to 0$ határesetben, mivel kétrétegű grafén esetén Kohn tétele nem alkalmazható, mind véges hullámszám vektornál is. Megmutattam továbbá, hogy a Landau szintek keveredése eltűnteti a szintek kereszteződését. Demonstráltam, hogy a szintek keveredése elsősorban közepes k hullámszám vektor tartományban jelentős. Ez a tartomány rugalmatlan fényszórással érhető el [I].

List of Symbols, Abbreviations and Conventions

a_0	Bohr radius
aI3	α-(BEDT-TTF)$_2$I$_3$
c	speed of light
$\delta(x)$	Dirac delta function
$\delta_{n,n'}$	Kronecker's delta
$e > 0$	elementary charge
ϵ_0	vacuum dielectric constant
ϵ_r	relative dielectric constant
$\hbar$	reduced Planck constant
$h.c.$	Hermitian conjugate
$H_n(x)$	Hermite polynomial
IQHE / IQH	integer quantum Hall effect / integer quantum Hall
$l = \sqrt{\hbar/eB}$	magnetic length
$L_n(x)$	Laguerre polynomial
$L_n^m(x)$	associated Laguerre polynomial
LL	Landau level
m_0	electron rest mass
μ_0	vacuum permeability
μ_B	Bohr magneton
PHES	particle-hole excitation spectrum
QHE	quantum Hall effect

QHF	quantum Hall ferromagnetic or quantum Hall ferromagnetism
RPA	random phase approximation
$\mathrm{sgn}(x)$	signum function
SdH oscillations	Shubnikov-de Haas oscillations
$\Theta(x)$	Heaviside step function
2D	two-dimensional
2DEG	two-dimensional electron gas
3D	three-dimensional
Tr	trace
UHM	upper-hybrid mode
v_F	Fermi velocity

The identity matrix and the Pauli matrices are

$$\sigma_0 = \begin{pmatrix} 1 & 0 \\ 0 & 1 \end{pmatrix}, \qquad \sigma_x = \begin{pmatrix} 0 & 1 \\ 1 & 0 \end{pmatrix}, \qquad \sigma_y = \begin{pmatrix} 0 & -i \\ i & 0 \end{pmatrix}, \qquad \sigma_z = \begin{pmatrix} 1 & 0 \\ 0 & -1 \end{pmatrix}.$$

Acknowledgements

First and foremost, I thank my supervisor, Csaba Tőke, for directing my work throughout the years, I feel exceptionally privileged to have been his PhD student. His thoroughness and patience helped me through the first years when I had undoubtedly little experience with conducting my own research. His enthusiasm, his remarkable knowledge and intuitions about physics were all indispensable for me to complete this thesis. My debt to him is beyond measure.

I am deeply indebted to György Papp, the solid-state physics teacher of mine, for his belief in my abilities, his encouragements and the time he devoted to discuss my future perspectives and possibilities as a newly graduated physics teacher. He suggested initially that I should continue my studies as a PhD student, for which I am more than grateful.

I express my deep gratitude to my professors at the Institute of Physics, University of Pécs, especially to József Janszky and János Hebling, for providing me help and advice whenever I needed. They have both supported me every step of the way. Besides, I thank the administrative staff, primarily Andrea Lóki and Kornélia Kurucz, for being precise, swift, up-to-date and incessantly smiling. I also thank my fellow student Ferenc Pittler for the memorable time we spent together on working out calculations or on discussing physics in general.

I am indebted to all members of the Exotic Quantum Phases *Momentum* Research Group and the Department of Theoretical Physics, Budapest University of Technology and Economics, in particular, to Gergely Zaránd. I highly appreciate their hospitality and the financial support they provided me during the last period of my studies. I have greatly enjoyed the lively group meetings, illuminating discussions and friendly atmosphere of the research group. I have benefited tremendously from the weekly

seminars, they have helped me in deepening my understanding of various fields of solid-state physics not strongly related to my research field. I also acknowledge the numerous presentation opportunities the group offered me, they have contributed much to perfecting my presentation skills.

Furthermore, I have been fortunate to collaborate with Mark Oliver Goerbig, Université Paris-Sud. I thank him for his openness of building up our fruitful research collaboration, for our stimulating discussions, his guidance and also for sharing his remarkable knowledge and expertise of physics with me. I acknowledge the scholarship provided by Campus France and the hospitality of all members, including professors and fellow students, of the Laboratoire de Physique des Solides, which made my stay in Orsay one of the most memorable period of my life.

In addition, I thank András Pályi, József Cserti, Katalin Kamarás, Sándor Bordács, Miguel Monteverde for fruitful discussions. Supercomputer facilities necessary for two of our projects presented in this thesis were provided by the National Information Infrastructure Development Institute, Hungary. I thank Győző Harka for his technical support.

Last, but not least, I thank my parents, my brother and my friends for their unyielding support, selflessness and their constant love. My gratitude to them knows no boundaries.

Appendix A

Monolayer Graphene in a Perpendicular Magnetic Field

Here we briefly reproduce the derivation of the eigenvalues and eigenstates of Eq. 2.9 for cone K ($\xi = 1$) following [27]. The corresponding time-independent Schrödinger equation is $\hat{H}_{\mathrm{G}}^{\xi=1}\Phi(x,y) = \epsilon\Phi(x,y)$. Due to our gauge choice $\mathbf{A} = (A_x, A_y, A_z) = (-yB, 0, 0)$ we make the ansatz for the spinorial wave function $\Phi(x,y) = e^{ikx}(\varphi(y)\ \upsilon(y))^{\mathrm{T}}$, where T denotes the transpose. Then

$$\hat{H}_{\mathrm{G}}^{\xi=1}\Phi(x,y) = \hbar v_F[p_x\sigma_x + p_y\sigma_y]\Phi(x,y) = \hbar v_F[(k - \frac{y}{l^2})\sigma_x + q_y\sigma_y]e^{ikx}\begin{pmatrix}\varphi(y)\\ \upsilon(y)\end{pmatrix}.$$

To proceed, we introduce the variable $\tilde{y} = y - kl^2$. After simplifying with the exponential and introducing the bosonic ladder operators $a = \frac{1}{\sqrt{2}l}(\tilde{y} + il^2 q_{\tilde{y}})$ and $a^\dagger = \frac{1}{\sqrt{2}l}(\tilde{y} - il^2 q_{\tilde{y}})$, which satisfy $[a, a^\dagger] = 1$, the Schrödinger equation becomes

$$\begin{pmatrix}0 & a\\ a^\dagger & 0\end{pmatrix}\begin{pmatrix}\varphi(\tilde{y})\\ \upsilon(\tilde{y})\end{pmatrix} = -\frac{\epsilon}{v_F\sqrt{2\hbar eB}}\begin{pmatrix}\varphi(\tilde{y})\\ \upsilon(\tilde{y})\end{pmatrix} \equiv \epsilon'\begin{pmatrix}\varphi(\tilde{y})\\ \upsilon(\tilde{y})\end{pmatrix}. \tag{A.1}$$

We are diagonalizing the Hamiltonian by taking the square of both sides of Eq. A.1. After some algebra, we get two decoupled equations as follows:

$$(1 + a^\dagger a)\varphi(\tilde{y}) = \epsilon'^2 \varphi(\tilde{y}), \tag{A.2}$$

$$a^\dagger a \upsilon(\tilde{y}) = \epsilon'^2 \upsilon(\tilde{y}). \tag{A.3}$$

In Eq. A.3 one recognizes the standard equation of the harmonic oscillator with $m = eB\hbar$ and $\omega = 1/\hbar$.[1] From this analogy the eigenvalues of the Hamiltonian in Eq. 2.9 are

$$\epsilon_n^{\mathrm{G}} = \mathrm{sgn}(n)\sqrt{2|n|}\frac{v_F\hbar}{l}, \tag{A.6}$$

where n is an integer. The eigenfunctions are given in terms of the harmonic oscillator eigenfunctions

$$\upsilon(\tilde{y}) \equiv \phi_{|n|}(\tilde{y}) = \phi_{|n|}(y - kl^2). \tag{A.7}$$

Similarly, Eq. A.2 leads to a harmonic oscillator equation with the same eigenvalue, but with eigenfunction $\varphi(\tilde{y}) \equiv \phi_{|n-1|}(y - kl^2)$. The spinorial wave function $\Phi(x, y)$ should be looked for in the form

$$\Phi_{|n|,k}^{\mathrm{G},\xi=1}(x, y) = \frac{1}{\sqrt{2}}\frac{e^{ikx}}{\sqrt{2\pi}}\begin{pmatrix} \alpha\phi_{|n-1|}(y - kl^2) \\ \beta\phi_{|n|}(y - kl^2) \end{pmatrix} \tag{A.8}$$

with parameters α and β to be determined. Substituting the wave function into the Hamiltonian Eq. A.1, one deduces $\alpha = -\mathrm{sgn}(n)\beta$, and from the normalization condi-

[1] The harmonic oscillator equation reads as

$$\frac{\hbar^2 q_y^2}{2m}\phi_n(y) + \frac{1}{2}m\omega^2 y^2 \phi_n(y) = \epsilon_n \phi_n(y), \tag{A.4}$$

where y and $q_y = -i\partial_y$ are the usual position and momentum operators. The corresponding eigenenergies and eigenstates in terms of the non-negative integer n quantum number:

$$\epsilon_n = \hbar\omega\left(n + \frac{1}{2}\right),$$
$$\phi_n(y) = \left(\frac{m\omega}{\hbar}\right)^{1/4}\frac{1}{\sqrt{\sqrt{\pi}2^n n!}}H_n\left(\sqrt{\frac{m\omega}{\hbar}}y\right)e^{-m\omega y^2/2\hbar}, \tag{A.5}$$

see [151].

tion we find $\beta = -1$. The final result is

$$\Phi^{\mathrm{G},\xi=1}_{|n|,k}(x,y) = \frac{1}{\sqrt{2}}\frac{e^{ikx}}{\sqrt{2\pi}}\begin{pmatrix}\mathrm{sgn}(n)\phi_{|n-1|}(y-kl^2)\\ -\phi_{|n|}(y-kl^2)\end{pmatrix}. \tag{A.9}$$

Appendix B

Eigenfunctions of α-(BEDT-TTF)$_2$I$_3$

For $n \neq 0$ in cone R the Landau orbitals are

$$\Phi_{n,k}^{\xi=1}(\tilde{\mathbf{r}}) = \frac{1}{\sqrt{4(1+\lambda)}} \left[\begin{pmatrix} -\beta \\ 1+\lambda \end{pmatrix} \phi_{n,k}^{\xi=1}(\tilde{\mathbf{r}}) + \begin{pmatrix} -1-\lambda \\ \beta \end{pmatrix} \mathrm{sgn}(n) \phi_{n-1,k}^{\xi=1}(\tilde{\mathbf{r}}) \right], \tag{B.1}$$

while for the $n = 0$ Landau level

$$\Phi_{0,k}^{\xi=1}(\tilde{\mathbf{r}}) = \frac{1}{\sqrt{2(1+\lambda)}} \begin{pmatrix} -\beta \\ 1+\lambda \end{pmatrix} \phi_{0,k}^{\xi=1}(\tilde{\mathbf{r}}). \tag{B.2}$$

For $n \neq 0$ in cone L, the orbitals are

$$\Phi_{n,k}^{\xi=-1}(\tilde{\mathbf{r}}) = \frac{1}{\sqrt{4(1+\lambda)}} \left[\begin{pmatrix} 1+\lambda \\ -\beta \end{pmatrix} \phi_{n,k}^{\xi=-1}(\tilde{\mathbf{r}}) + \begin{pmatrix} -\beta \\ 1+\lambda \end{pmatrix} \mathrm{sgn}(n) \phi_{n-1,k}^{\xi=-1}(\tilde{\mathbf{r}}) \right], \tag{B.3}$$

while for the $n = 0$

$$\Phi_{0,k}^{\xi=-1}(\tilde{\mathbf{r}}) = \frac{1}{\sqrt{2(1+\lambda)}} \begin{pmatrix} -1-\lambda \\ \beta \end{pmatrix} \phi_{0,k}^{\xi=-1}(\tilde{\mathbf{r}}). \tag{B.4}$$

We have used the subformulas ($\xi = \pm 1$)

$$\phi^{\xi}_{n,k}(\tilde{\mathbf{r}}) = \frac{e^{ik\tilde{x}}}{\sqrt{2\pi}} \frac{\lambda^{1/4}}{(2^{|n|}|n|!\sqrt{\pi}\alpha l)^{1/2}} e^{-\Upsilon^2_{n,\xi}/2} H_{|n|}(\Upsilon_{n,\xi}) \tag{B.5}$$

and

$$\phi^{\xi}_{n-1,k}(\tilde{\mathbf{r}}) = \frac{e^{ik\tilde{x}}}{\sqrt{2\pi}} \frac{\lambda^{1/4}}{(2^{|n-1|}|n-1|!\sqrt{\pi}\alpha l)^{1/2}} e^{-\Upsilon^2_{n,\xi}/2} H_{|n-1|}(\Upsilon_{n,\xi}),$$

with the argument

$$\Upsilon_{n,\xi} = \sqrt{\lambda}\tilde{y}/\alpha l - \sqrt{\lambda}\alpha l k - \xi\beta\sqrt{2|n|}\mathrm{sgn}(n). \tag{B.6}$$

Notice that $\Upsilon_{n,\xi}$ depends on both the LL index (including its sign) and the cone index ξ. Note also that Eqs. B.5 and B.6 use the same argument $\Upsilon_{n,\xi}$.

Appendix C

Dimensionless Matrix Elements

The evaluation of Eq. 3.4 amounts to, besides the standard matrix multiplication, the evaluation of the following integral:

$$\int \mathrm{d}\mathbf{r}\phi^*_{n,k}(\mathbf{r})\phi_{n',k'}(\mathbf{r}) = \int \mathrm{d}\mathbf{r}\frac{\sqrt{\lambda}}{2\pi l}\frac{e^{-ix(k-k')}}{\sqrt{2^{|n|+|n'|}|n'|!|n|!\pi}}e^{-\Upsilon_n^2/2}e^{-\Upsilon_{n'}^2/2}H_{|n|}(\Upsilon_n)H_{|n'|}(\Upsilon_{n'}),$$

where the $\phi_{n,k}(\mathbf{r})$ functions are defined in Eqs. 2.19 and 2.21. The integral with respect to x is straightforwardly evaluated leading to $\delta(k-k')$. To proceed, it is convenient to introduce a new variable $y' = \sqrt{\lambda}y/l - \sqrt{\lambda}lk$. With some algebra

$$\int \mathrm{d}\mathbf{r}\phi^*_{n,k}(\mathbf{r})\phi_{n',k'}(\mathbf{r}) = \frac{\delta(k-k')}{\sqrt{2^{|n|+|n'|}|n'|!|n|!\pi}}e^{-\beta^2(|n|+|n'|)/2}e^{\beta^2\sqrt{|n||n'|}\mathrm{sgn}(n)\mathrm{sgn}(n')}\times$$
$$\times\int \mathrm{d}y' e^{-\left(y'-\beta(\mathrm{sgn}(n)\sqrt{|n|}+\mathrm{sgn}(n')\sqrt{|n'|})/\sqrt{2}\right)^2}H_{|n'|}(y'-\beta\mathrm{sgn}(n')\sqrt{2|n'|})H_{|n|}(y'-\beta\mathrm{sgn}(n)\sqrt{2|n|}).$$

After another change of variable $y'' = y'-\beta(\mathrm{sgn}(n)\sqrt{|n|}+\mathrm{sgn}(n')\sqrt{|n'|})/\sqrt{2}$ the integral may readily be evaluated using the identity 7.377 of Ref. [58] with Laguerre-Hermite polynomials:

$$\int_{-\infty}^{\infty}\mathrm{d}x e^{-x^2}H_m(x+y)H_n(x+z) = \begin{cases} 2^n\sqrt{\pi}m!z^{n-m}L_m^{n-m}(-2yz) & m \leq n, \\ 2^m\sqrt{\pi}n!y^{m-n}L_n^{m-n}(-2yz) & m > n. \end{cases} \tag{C.1}$$

Then the final result reads

$$\int \mathrm{d}\mathbf{r}\phi^*_{n,k}(\mathbf{r})\phi_{n',k'}(\mathbf{r}) = \begin{cases} \delta(k-k')F^{n,n'}_{|n|,|n'|} & |n| \geq |n'|, \\ \delta(k-k')F^{n',n}_{|n'|,|n|} & |n| < |n'|. \end{cases}$$

Here we find it convenient to define the function $F^{s,p}_{q,r}$ with integers s, p, q, and r as follows

$$F^{s,p}_{q,r} = \sqrt{\frac{r!}{q!}} e^{-\left(z^p_s\right)^2/2} \left(z^p_s\right)^{q-r} \; L^{q-r}_r\left(\left(z^p_s\right)^2\right), \quad z^p_s = \beta(\mathrm{sgn}(p)\sqrt{p} - \mathrm{sgn}(s)\sqrt{s}) \tag{C.2}$$

for $q \geq r$, otherwise $F^{s,p}_{q,r} = F^{p,s}_{r,q}$.

Appendix D

Derivation of the Bare Polarization Function for Massive Carriers

D.1 Derivation of the Time-Ordered Green's Function

The field operators are given in terms of the wave functions Eq. 2.3 as

$$\Psi_\sigma(\mathbf{r},t) = \sum_n \int \mathrm{d}q \phi_{n,q}(\mathbf{r}) e^{-it\epsilon_n^{\mathrm{Q}}} c_{\sigma,n,q}. \tag{D.1}$$

Here $c_{\sigma,n,q}$ is the annihilation operator of a particle with spin σ, momentum q and LL index n. We suppress spin to avoid clutter, the time-ordered Green's function is given as

$$\begin{aligned}\mathcal{G}^{(0)}(\mathbf{r},\mathbf{r}',t) &= -i\langle \mathcal{T}\Psi(\mathbf{r},t)\otimes\Psi^\dagger(\mathbf{r}',0)\rangle \\ &= -i\Theta(t)\sum_{n',n}\int \mathrm{d}q \int \mathrm{d}q' \phi_{n,q}(\mathbf{r})\phi^*_{n',q'}(\mathbf{r}')e^{-it\epsilon_n^{\mathrm{Q}}}\langle c_{n,q}c^\dagger_{n',q'}\rangle \\ &\quad +i\Theta(-t)\sum_{n',n}\int \mathrm{d}q \int \mathrm{d}q' \phi_{n,q}(\mathbf{r})\phi^*_{n',q'}(\mathbf{r}')e^{-it\epsilon_n^{\mathrm{Q}}}\langle c^\dagger_{n',q'}c_{n,q}\rangle,\end{aligned} \tag{D.2}$$

where $\otimes$ denotes the outer product, $\mathcal{T}$ is the time-ordering operator, see [47]. Due to the simple scalar form of the wave function, $\mathcal{G}^{(0)}$ is also a scalar function. Using that $\langle c_{n,q}c^\dagger_{n',q'}\rangle = \delta_{n,n'}\delta(q-q')\Theta(\epsilon_n^{\mathrm{Q}}-\epsilon_F)$ and $\langle c^\dagger_{n',q'}c_{n,q}\rangle = \delta_{n,n'}\delta(q-q')(1-\Theta(\epsilon_n^{\mathrm{Q}}-\epsilon_F))$

with ϵ_F Fermi energy,

$$\mathcal{G}^{(0)}(\mathbf{r},\mathbf{r}',t) = -i\sum_n \int \mathrm{d}q \phi_{n,q}(\mathbf{r})\phi^*_{n,q}(\mathbf{r}')e^{-it\epsilon_n^{\mathrm{Q}}}\left[\Theta(t)\Theta(\epsilon_n^{\mathrm{Q}}-\epsilon_F)-\Theta(-t)(1-\Theta(\epsilon_n^{\mathrm{Q}}-\epsilon_F))\right].$$

Then using the definition $\Theta(t) = -\frac{1}{2\pi i}\int \mathrm{d}E e^{-iEt}/(E+i\delta)$ and making the possible simplifications

$$\begin{aligned}\mathcal{G}^{(0)}(\mathbf{r},\mathbf{r}',t) &= \frac{1}{2\pi}\sum_n \int \mathrm{d}q \int \mathrm{d}E \phi_{n,q}(\mathbf{r})\phi^*_{n,q}(\mathbf{r}')e^{-it(\epsilon_n^{\mathrm{Q}}+E)}\left[\frac{\Theta(\epsilon_n^{\mathrm{Q}}-\epsilon_F)}{E+i\delta}+\frac{1-\Theta(\epsilon_n^{\mathrm{Q}}-\epsilon_F)}{E-i\delta}\right]\\ &= \frac{1}{2\pi}\sum_n \int \mathrm{d}q \int \mathrm{d}E \phi_{n,q}(\mathbf{r})\phi^*_{n,q}(\mathbf{r}')e^{-it(\epsilon_n^{\mathrm{Q}}+E)}\frac{1}{E+i\delta\mathrm{sgn}(\epsilon_n^{\mathrm{Q}}-\epsilon_F)}.\end{aligned}$$

In the last equation we have explicitly evaluated the Heaviside functions. Introducing a new variable $E' = E+\epsilon_n^{\mathrm{Q}}$ and omitting the prime in the next step we can easily reorganize the equation. We get

$$\mathcal{G}^{(0)}(\mathbf{r},\mathbf{r}',t) = \frac{1}{2\pi}\int \mathrm{d}E e^{-itE}\sum_n \int \mathrm{d}q \frac{\phi_{n,q}(\mathbf{r})\phi^*_{n,q}(\mathbf{r}')}{E-\epsilon_n^{\mathrm{Q}}+i\delta\mathrm{sgn}(\epsilon_n^{\mathrm{Q}}-\epsilon_F)}. \tag{D.3}$$

Here we recognize the Fourier transformed $\mathcal{G}^{(0)}(\mathbf{r},\mathbf{r}',E)$. In the following it is convenient to use this form of the Green's function, in which we introduce the center of mass and relative coordinates as $\mathbf{R} = (\mathbf{r}+\mathbf{r}')/2$ and $\Delta\mathbf{r} = \mathbf{r}-\mathbf{r}'$. Then

$$\mathcal{G}^{(0)}(\mathbf{R},\Delta\mathbf{r},E) = \sum_n \int \mathrm{d}q \frac{\phi_{n,q}(\mathbf{R}+\frac{\Delta\mathbf{r}}{2})\phi^*_{n,q}(\mathbf{R}-\frac{\Delta\mathbf{r}}{2})}{E-\epsilon_n^{\mathrm{Q}}+i\delta\mathrm{sgn}(\epsilon_n^{\mathrm{Q}}-\epsilon_F)}. \tag{D.4}$$

After a Fourier transform according to $\Delta\mathbf{r}$ we arrive at

$$\mathcal{G}^{(0)}(\mathbf{R},\mathbf{p},E) = \sum_n \int \mathrm{d}q \int \mathrm{d}\Delta\mathbf{r} e^{i\mathbf{p}\Delta\mathbf{r}} \frac{\phi_{n,q}(\mathbf{R}+\frac{\Delta\mathbf{r}}{2})\phi^*_{n,q}(\mathbf{R}-\frac{\Delta\mathbf{r}}{2})}{E-\epsilon_n^{\mathrm{Q}}+i\delta\mathrm{sgn}(\epsilon_n^{\mathrm{Q}}-\epsilon_F)}. \tag{D.5}$$

D.2 Bare Polarization Function for the Two-Dimensional Electron Gas

In terms of the previously defined time-ordered Green's function the time-ordered response function is

$$\chi^{\mathrm{T}}(\mathbf{k},\omega) = -i\mathrm{Tr}\int\frac{\mathrm{d}E}{2\pi}\int\frac{\mathrm{d}\mathbf{p}}{(2\pi)^2}\mathcal{G}^{(0)}(\mathbf{R},\mathbf{p}-\frac{\mathbf{k}}{2},E)\mathcal{G}^{(0)}(\mathbf{R},\mathbf{p}+\frac{\mathbf{k}}{2},E+\omega) \tag{D.6}$$

$$\begin{aligned}
&= -i\int\frac{\mathrm{d}\mathbf{p}}{(2\pi)^2}\sum_{n,n'}\int\mathrm{d}q\int\mathrm{d}q'\int\mathrm{d}\Delta\mathbf{r}\int\mathrm{d}\Delta\mathbf{r}' e^{i(\mathbf{p}-\frac{\mathbf{k}}{2})\Delta\mathbf{r}}e^{i(\mathbf{p}+\frac{\mathbf{k}}{2})\Delta\mathbf{r}'}\times \\
&\quad\times\phi_{n,q}(\mathbf{R}+\frac{\Delta\mathbf{r}}{2})\phi^*_{n,q}(\mathbf{R}-\frac{\Delta\mathbf{r}}{2})\phi_{n',q'}(\mathbf{R}+\frac{\Delta\mathbf{r}'}{2})\phi^*_{n',q'}(\mathbf{R}-\frac{\Delta\mathbf{r}'}{2})\times \qquad \text{(D.7)}\\
&\quad\times\int\frac{\mathrm{d}E}{2\pi}\frac{1}{E-\epsilon^{\mathrm{Q}}_n+i\delta\mathrm{sgn}(\epsilon^{\mathrm{Q}}_n-\epsilon_F)}\cdot\frac{1}{E+\omega-\epsilon^{\mathrm{Q}}_{n'}+i\delta\mathrm{sgn}(\epsilon^{\mathrm{Q}}_{n'}-\epsilon_F)}.
\end{aligned}$$

First, we evaluate the integral with respect to E. We use the residue theorem after extending the integral to the complex plane and by closing the contour in the upper half plane anticlockwise. We recognize that the integrand has simple poles at $E_1 = \epsilon^{\mathrm{Q}}_n - i\delta\mathrm{sgn}(\epsilon^{\mathrm{Q}}_n-\epsilon_F)$ and $E_2 = -\omega+\epsilon^{\mathrm{Q}}_{n'} - i\delta\mathrm{sgn}(\epsilon^{\mathrm{Q}}_{n'}-\epsilon_F)$. Notice that the poles are either in the upper or the lower half plane depending on the value of the Landau level energy with respect to the Fermi energy. Then

$$\begin{aligned}
\int_E &\equiv \int\mathrm{d}E\frac{1}{E-\epsilon^{\mathrm{Q}}_n+i\delta\mathrm{sgn}(\epsilon^{\mathrm{Q}}_n-\epsilon_F)}\cdot\frac{1}{E+\omega-\epsilon^{\mathrm{Q}}_{n'}+i\delta\mathrm{sgn}(\epsilon^{\mathrm{Q}}_{n'}-\epsilon_F)}\\
&= 2\pi i\left[\frac{1-\Theta(\epsilon^{\mathrm{Q}}_n-\epsilon_F)}{\epsilon^{\mathrm{Q}}_n-\epsilon^{\mathrm{Q}}_{n'}+\omega+i\delta(1+\mathrm{sgn}(\epsilon^{\mathrm{Q}}_{n'}-\epsilon_F))}+\frac{1-\Theta(\epsilon^{\mathrm{Q}}_{n'}-\epsilon_F)}{-\omega-\epsilon^{\mathrm{Q}}_n+\epsilon^{\mathrm{Q}}_{n'}+i\delta(1+\mathrm{sgn}(\epsilon^{\mathrm{Q}}_n-\epsilon_F))}\right]\\
&= 2\pi i\left[\frac{(1-\Theta(\epsilon^{\mathrm{Q}}_n-\epsilon_F))\Theta(\epsilon^{\mathrm{Q}}_{n'}-\epsilon_F)}{\epsilon^{\mathrm{Q}}_n-\epsilon^{\mathrm{Q}}_{n'}+\omega+i2\delta}+\frac{(1-\Theta(\epsilon^{\mathrm{Q}}_{n'}-\epsilon_F))\Theta(\epsilon^{\mathrm{Q}}_n-\epsilon_F)}{-\omega-\epsilon^{\mathrm{Q}}_n+\epsilon^{\mathrm{Q}}_{n'}+i2\delta}\right].
\end{aligned}$$

We have got this expression by rewriting the signums in the denominator of the first line in terms of Heaviside functions. After some algebra, one can recover the last line. To proceed, we apply the Sokhotski - Plemelj theorem:

$$\lim_{\delta\to 0^+}\frac{1}{x\pm i\delta} = \mathcal{P}\frac{1}{x}\mp i\pi\delta(x), \tag{D.8}$$

here $\mathcal{P}$ denotes the Cauchy principal value. With these

$$\begin{aligned}
\int_E &= 2\pi i \left[\mathcal{P}\frac{(1-\Theta(\epsilon_n^{\mathrm{Q}}-\epsilon_F))\Theta(\epsilon_{n'}^{\mathrm{Q}}-\epsilon_F)}{\epsilon_n^{\mathrm{Q}}-\epsilon_{n'}^{\mathrm{Q}}+\omega} - i\pi\delta(\epsilon_n^{\mathrm{Q}}-\epsilon_{n'}^{\mathrm{Q}}+\omega)(1-\Theta(\epsilon_n^{\mathrm{Q}}-\epsilon_F))\Theta(\epsilon_{n'}^{\mathrm{Q}}-\epsilon_F) \right. \\
&\quad \left. +\mathcal{P}\frac{(1-\Theta(\epsilon_{n'}^{\mathrm{Q}}-\epsilon_F))\Theta(\epsilon_n^{\mathrm{Q}}-\epsilon_F)}{-\omega-\epsilon_n^{\mathrm{Q}}+\epsilon_{n'}^{\mathrm{Q}}} - i\pi\delta(-\omega-\epsilon_n^{\mathrm{Q}}+\epsilon_{n'}^{\mathrm{Q}})(1-\Theta(\epsilon_{n'}^{\mathrm{Q}}-\epsilon_F))\Theta(\epsilon_n^{\mathrm{Q}}-\epsilon_F) \right] \\
&= 2\pi i \left[\mathcal{P}\frac{1}{\epsilon_n^{\mathrm{Q}}-\epsilon_{n'}^{\mathrm{Q}}+\omega}(\Theta(\epsilon_{n'}^{\mathrm{Q}}-\epsilon_F)-\Theta(\epsilon_n^{\mathrm{Q}}-\epsilon_F)) \right. \\
&\quad \left. -i\pi\delta(\epsilon_n^{\mathrm{Q}}-\epsilon_{n'}^{\mathrm{Q}}+\omega)(\Theta(\epsilon_{n'}^{\mathrm{Q}}-\epsilon_F)+\Theta(\epsilon_n^{\mathrm{Q}}-\epsilon_F)-2\Theta(\epsilon_{n'}^{\mathrm{Q}}-\epsilon_F)\Theta(\epsilon_n^{\mathrm{Q}}-\epsilon_F)) \right] \\
&= 2\pi i(\Theta(\epsilon_{n'}^{\mathrm{Q}}-\epsilon_F)-\Theta(\epsilon_n^{\mathrm{Q}}-\epsilon_F)) \left[\mathcal{P}\frac{1}{\epsilon_n^{\mathrm{Q}}-\epsilon_{n'}^{\mathrm{Q}}+\omega} - i\pi\delta(\epsilon_n^{\mathrm{Q}}-\epsilon_{n'}^{\mathrm{Q}}+\omega)\mathrm{sgn}(\omega) \right] \\
&= 2\pi i\frac{\Theta(\epsilon_{n'}^{\mathrm{Q}}-\epsilon_F)-\Theta(\epsilon_n^{\mathrm{Q}}-\epsilon_F)}{\epsilon_n^{\mathrm{Q}}-\epsilon_{n'}^{\mathrm{Q}}+\omega+i\delta\mathrm{sgn}(\omega)}.
\end{aligned}$$

We have arrived at the final expression for the integral $\int_E$. Now we implement this result in χ^{T}, we regroup the elements, and use the fact that $\Delta\mathbf{r} = -\Delta\mathbf{r}'$. Then we arrive at

$$\chi^{\mathrm{T}}(\mathbf{k},\omega) = \int \frac{\mathrm{d}\mathbf{p}}{(2\pi)^2}\sum_{n,n'}\int \mathrm{d}q \int \mathrm{d}q' \frac{\Theta(\epsilon_{n'}^{\mathrm{Q}}-\epsilon_F)-\Theta(\epsilon_n^{\mathrm{Q}}-\epsilon_F)}{\omega+\epsilon_n^{\mathrm{Q}}-\epsilon_{n'}^{\mathrm{Q}}+i\delta\mathrm{sgn}(\omega)}\times \tag{D.9a}$$

$$\times \int \mathrm{d}\Delta\mathbf{r}\phi^*_{n',q'}(\mathbf{R}+\frac{\Delta\mathbf{r}}{2})e^{i(\mathbf{p}-\frac{\mathbf{k}}{2})\Delta\mathbf{r}}\phi_{n,q}(\mathbf{R}+\frac{\Delta\mathbf{r}}{2})\times \tag{D.9b}$$

$$\times \int \mathrm{d}\Delta\mathbf{r}'\phi^*_{n,q}(\mathbf{R}+\frac{\Delta\mathbf{r}'}{2})e^{i(\mathbf{p}+\frac{\mathbf{k}}{2})\Delta\mathbf{r}'}\phi_{n',q'}(\mathbf{R}+\frac{\Delta\mathbf{r}'}{2}). \tag{D.9c}$$

The first integral can be executed after the appropriate change of variables: $\mathbf{z} = \mathbf{R}+\frac{\Delta\mathbf{r}}{2}$. Now we are in the position to apply Eq. E.4. Then

$$\begin{aligned}
&\int \mathrm{d}\Delta\mathbf{r}\phi^*_{n',q'}(\mathbf{R}+\frac{\Delta\mathbf{r}}{2})e^{i(\mathbf{p}-\frac{\mathbf{k}}{2})\Delta\mathbf{r}}\phi_{n,q}(\mathbf{R}+\frac{\Delta\mathbf{r}}{2}) \\
&\qquad = 4e^{-i(2\mathbf{p}-\mathbf{k})\mathbf{R}}\delta(q-q'+2p_y-k_y)F_{n',n}(-2\mathbf{p}+\mathbf{k})e^{-i(-2p_x+k_x)l^2\frac{q+q'}{2}}.
\end{aligned}$$

Similarly with the second integral:

$$\int \mathrm{d}\Delta\mathbf{r}'\phi^*_{n,q}(\mathbf{R}+\frac{\Delta\mathbf{r}'}{2})e^{i(\mathbf{p}+\frac{\mathbf{k}}{2})\Delta\mathbf{r}'}\phi_{n',q'}(\mathbf{R}+\frac{\Delta\mathbf{r}'}{2})$$
$$= 4e^{-i(2\mathbf{p}+\mathbf{k})\mathbf{R}}\delta(q'-q+2p_y+k_y)F_{n,n'}(-2\mathbf{p}-\mathbf{k})e^{i(2p_x+k_x)l^2\frac{q+q'}{2}}.$$

The time-ordered response function becomes:

$$\begin{aligned}\chi^{\mathrm{T}}(\mathbf{k},\omega) &= 16\int\frac{\mathrm{d}\mathbf{p}}{(2\pi)^2}\sum_{n,n'}\int\mathrm{d}q\int\mathrm{d}q'\frac{\Theta(\epsilon^{\mathrm{Q}}_{n'}-\epsilon_F)-\Theta(\epsilon^{\mathrm{Q}}_{n}-\epsilon_F)}{\omega+\epsilon^{\mathrm{Q}}_n-\epsilon^{\mathrm{Q}}_{n'}+i\delta\mathrm{sgn}(\omega)}F_{n',n}(-2\mathbf{p}+\mathbf{k})\times\\ &\times F_{n,n'}(-2\mathbf{p}-\mathbf{k})\delta(q-q'+2p_y-k_y)\delta(q'-q+2p_y+k_y)e^{i4p_xl^2\frac{q+q'}{2}}e^{-i4\mathbf{pR}}\\ &= 4\int\frac{\mathrm{d}\mathbf{p}}{(2\pi)^2}\sum_{n,n'}\int\mathrm{d}\Delta q\int\mathrm{d}Q\frac{\Theta(\epsilon^{\mathrm{Q}}_{n'}-\epsilon_F)-\Theta(\epsilon^{\mathrm{Q}}_{n}-\epsilon_F)}{\omega+\epsilon^{\mathrm{Q}}_n-\epsilon^{\mathrm{Q}}_{n'}+i\delta\mathrm{sgn}(\omega)}F_{n',n}(-2\mathbf{p}+\mathbf{k})\times\\ &\times F_{n,n'}(-2\mathbf{p}-\mathbf{k})\delta(\frac{\Delta q}{2}+p_y-\frac{k_y}{2})\delta(-\frac{\Delta q}{2}+p_y+\frac{k_y}{2})e^{i4p_xl^2Q}e^{-i4\mathbf{pR}}.\end{aligned}$$

Here we have applied the identity $\delta(ax)=\frac{1}{|a|}\delta(x)$, and in the last line we have introduced *centre of mass* coordinates: $\frac{q+q'}{2}=Q$ and $q-q'=\Delta q$. One can evaluate the integral with respect to Q, leading to $p_x=0$, while the rearrangement and the evaluation of the delta functions combined with the integral with respect to Δq leads to $p_y=0$. By denoting the highest-filled Landau level n^F_Q

$$\begin{aligned}\chi^{\mathrm{T}}(\mathbf{k},\omega) &= \frac{1}{2\pi l^2}\sum_{n,n'}\frac{\Theta(\epsilon^{\mathrm{Q}}_{n'}-\epsilon_F)-\Theta(\epsilon^{\mathrm{Q}}_{n}-\epsilon_F)}{\omega+\epsilon^{\mathrm{Q}}_n-\epsilon^{\mathrm{Q}}_{n'}+i\delta\mathrm{sgn}(\omega)}F_{n',n}(\mathbf{k})F_{n,n'}(-\mathbf{k})\\ &= \frac{1}{2\pi l^2}\sum_{n,n'}\frac{\Theta(\epsilon^{\mathrm{Q}}_{n'}-\epsilon_F)-\Theta(\epsilon^{\mathrm{Q}}_{n}-\epsilon_F)}{\omega+\epsilon^{\mathrm{Q}}_n-\epsilon^{\mathrm{Q}}_{n'}+i\delta\mathrm{sgn}(\omega)}|F_{n',n}(\mathbf{k})|^2\\ &= \frac{1}{2\pi l^2}\sum_{n\le n^F_Q}\sum_{n'>n^F_Q}\frac{|F_{n',n}(\mathbf{k})|^2}{\omega+\epsilon^{\mathrm{Q}}_n-\epsilon^{\mathrm{Q}}_{n'}+i\delta\mathrm{sgn}(\omega)}-\sum_{n'\le n^F_Q}\sum_{n>n^F_Q}\frac{|F_{n',n}(\mathbf{k})|^2}{\omega+\epsilon^{\mathrm{Q}}_n-\epsilon^{\mathrm{Q}}_{n'}+i\delta\mathrm{sgn}(\omega)}.\end{aligned}$$

With the application of Eq. D.8 one eliminates the signum, finally we get:

$$\begin{aligned}\chi^{\mathrm{T}}(\mathbf{k},\omega) &= \frac{1}{2\pi l^2}\sum_{n\le n^F_Q}\sum_{n'>n^F_Q}\frac{|F_{n',n}(\mathbf{k})|^2}{\omega+\epsilon^{\mathrm{Q}}_n-\epsilon^{\mathrm{Q}}_{n'}+i\delta}-\sum_{n'\le n^F_Q}\sum_{n>n^F_Q}\frac{|F_{n',n}(\mathbf{k})|^2}{\omega+\epsilon^{\mathrm{Q}}_n-\epsilon^{\mathrm{Q}}_{n'}-i\delta}\\ &= \frac{1}{2\pi l^2}\sum_{n'\le n^F_Q}\sum_{n>n^F_Q}(\frac{|F_{n,n'}(\mathbf{k})|^2}{\omega-\epsilon^{\mathrm{Q}}_n+\epsilon^{\mathrm{Q}}_{n'}+i\delta}+\frac{|F_{n',n}(\mathbf{k})|^2}{-\omega-\epsilon^{\mathrm{Q}}_n+\epsilon^{\mathrm{Q}}_{n'}+i\delta}).\end{aligned}\tag{D.10}$$

To get the retarded response function we shall use the identities of Eq. 4.4, which amounts to the replacement of $i\delta$ to $-i\delta$ in the second term:

$$\chi_Q^{(0)}(\mathbf{k},\omega) = \frac{1}{2\pi l^2} \sum_{n' \leq n_Q^F} \sum_{n > n_Q^F} \left(\frac{|F_{n,n'}(\mathbf{k})|^2}{\omega - \epsilon_n^{\mathrm{Q}} + \epsilon_{n'}^{\mathrm{Q}} + i\delta} + \frac{|F_{n',n}(\mathbf{k})|^2}{-\omega - \epsilon_n^{\mathrm{Q}} + \epsilon_{n'}^{\mathrm{Q}} - i\delta} \right). \quad \text{(D.11)}$$

Appendix E

The Computation of Form Factors

E.1 Form Factor for Conventional Two-Dimensional Electron Gas

We use here the definition of the LL wave functions given in Eq. 2.3 and $\mathbf{q} = (q_x, q_y)$. Then the integral to be evaluated is

$$\int \mathrm{d}\mathbf{r}\ \phi^*_{n',k'}(\mathbf{r}) e^{-i\mathbf{q}\cdot\mathbf{r}} \phi_{n,k}(\mathbf{r}) = \frac{1}{2\pi l\sqrt{\pi 2^{n+n'} n'! n!}} \int \mathrm{d}x e^{i(-q_x - k' + k)x} \times$$
$$\times \int \mathrm{d}y e^{-iq_y y} e^{-\frac{(y-kl^2)^2 + (y-k'l^2)^2}{2l^2}} H_n(\frac{y}{l} - kl) H_{n'}(\frac{y}{l} - k'l). \quad \text{(E.1)}$$

The integral with respect to x leads to a Dirac delta function, whereas the integral with respect to y can be simplified by introducing a new variable $y' = y - \frac{k+k'}{2} l^2$, and making use of the Dirac delta function. Then the expression becomes:

$$\int \mathrm{d}\mathbf{r}\ \phi^*_{n',k'}(\mathbf{r}) e^{-i\mathbf{q}\cdot\mathbf{r}} \phi_{n,k}(\mathbf{r}) =$$
$$\frac{\delta(-q_x - k' + k)}{2^{\frac{n+n'}{2}} l\sqrt{\pi n'! n!}} e^{-iq_y \frac{k+k'}{2} l^2} e^{-\frac{q_x^2 l^2}{4}} \int \mathrm{d}y' e^{-iq_y y' - \frac{y'^2}{l^2}} H_n(\frac{y'}{l} - \frac{q_x l}{2}) H_{n'}(\frac{y'}{l} + \frac{q_x l}{2}).$$

With the view to apply identity Eq. C.1 we introduce another new variable: $y'' = \frac{y'}{l} + \frac{iq_y l}{2}$, and we omit the tildes, then the integral becomes:

$$\frac{\delta(-q_x - k' + k)}{2^{\frac{n+n'}{2}}\sqrt{\pi n'! n!}} e^{-iq_y \frac{k+k'}{2} l^2 - \frac{q_x^2 l^2}{4}} \int \mathrm{d}y e^{-y^2 - \frac{q_y^2 l^2}{4}} H_n(y - \frac{iq_y l}{2} - \frac{q_x l}{2}) H_{n'}(y - \frac{iq_y l}{2} + \frac{q_x l}{2})$$
$$= \begin{cases} \delta(-q_x - k' + k) 2^{\frac{n'-n}{2}} \sqrt{\frac{n!}{n'!}} (\frac{q_x - iq_y}{2} l)^{n'-n} L_n^{n'-n}(\frac{|q|^2 l^2}{2}) e^{-iq_y \frac{k+k'}{2} l^2 - \frac{|q|^2 l^2}{4}} & n' \geq n, \\ \delta(-q_x - k' + k) 2^{\frac{n-n'}{2}} \sqrt{\frac{n'!}{n!}} (\frac{-q_x - iq_y}{2} l)^{n-n'} L_{n'}^{n-n'}(\frac{|q|^2 l^2}{2}) e^{-iq_y \frac{k+k'}{2} l^2 - \frac{|q|^2 l^2}{4}} & n' < n. \end{cases}$$

We define the form factor $F_{n',n}$ with the following properties: if $n' \geq n$

$$F_{n',n}(\mathbf{q}) = \sqrt{\frac{n!}{n'!}} (\frac{q_x - iq_y}{\sqrt{2}} l)^{n'-n} L_n^{n'-n}(\frac{|q|^2 l^2}{2}) e^{-\frac{|q|^2 l^2}{4}}, \tag{E.2}$$

and if $n' < n$

$$F_{n,n'}(\mathbf{q}) = F^*_{n',n}(-\mathbf{q}). \tag{E.3}$$

With this notation the original integral may be given in a compact form:

$$\int \mathrm{d}\mathbf{r}\ \phi^*_{n',k'}(\mathbf{r}) e^{-i\mathbf{q}\cdot\mathbf{r}} \phi_{n,k}(\mathbf{r}) = \delta(-q_x - k' + k) F_{n',n}(\mathbf{q}) e^{-iq_y \frac{k+k'}{2} l^2}. \tag{E.4}$$

E.2 Form Factor for the Weyl System

Here we sketch the main steps of the derivation of the form factor for the Weyl materials in Eq. E.8, which is an important ingredient of the calculation of the time-ordered response function $\chi^{\mathrm{T}}_{\xi}(\tilde{\mathbf{k}}, \omega)$ in Eq. 4.18.

We start with the wave function of Eq. B.5 with the argument given in Eq. B.6. One shall evaluate the following integral

$$\int_{\mathbf{r}} \equiv \int \mathrm{d}\mathbf{r} [\phi^{\xi}_{n',k'}(\mathbf{r})]^* e^{-i\mathbf{q}\cdot\mathbf{r}} \phi^{\xi}_{n,k}(\mathbf{r}) \tag{E.5}$$
$$= \int \mathrm{d}\mathbf{r} \frac{e^{-i(k'-k)x}}{2\pi\alpha l} \frac{\lambda^{1/2}}{(2^{|n'|+|n|}|n'|!|n|!\pi)^{1/2}} e^{-(\Upsilon^2_{n',\xi} + \Upsilon^2_{n,\xi})/2} e^{-i\mathbf{q}\cdot\mathbf{r}} H_{|n'|}(\Upsilon_{n',\xi}) H_{|n|}(\Upsilon_{n,\xi}).$$

We introduce new variables: $y' = y\sqrt{\lambda}/\alpha l$ and also $k_3 = \sqrt{\lambda}\alpha l k + \xi\beta\sqrt{2|n|}\mathrm{sgn}(n)$ along

with $k_4 = \sqrt{\lambda}\alpha l k' + \xi\beta\sqrt{2|n'|}\mathrm{sgn}(n')$. Then

$$\int_{\mathbf{r}} = \frac{1}{2\pi}\frac{1}{(2^{|n'|+|n|}|n'|!|n|!\pi)^{1/2}}\int \mathrm{d}x \int \mathrm{d}y' e^{-(y'-k_3)^2/2} e^{-(y'-k_4)^2/2} e^{-i(q_x x + q_y l\alpha y'/\sqrt{\lambda})} \times$$
$$\times\, e^{-ix(k_4-k_3)/\sqrt{\lambda}l\alpha} e^{-ix\xi\beta(\sqrt{2|n|}\mathrm{sgn}(n)-\sqrt{2|n'|}\mathrm{sgn}(n'))/\sqrt{\lambda}l\alpha} H_{|n'|}(y'-k_4)H_{|n|}(y'-k_3).$$

For simplicity we omit the prime in the following. We are in the position to execute the integral with respect to x, leading to

$$\int \mathrm{d}x e^{-ix(k_4-k_3)/\sqrt{\lambda}l\alpha} e^{-ix\xi\beta(\sqrt{2|n|}\mathrm{sgn}(n)-\sqrt{2|n'|}\mathrm{sgn}(n'))/\sqrt{\lambda}l\alpha} e^{-iq_x x}$$
$$= 2\pi\delta\left((k_4 - k_3 - \xi\beta\mathrm{sgn}(n')\sqrt{2|n'|} + \xi\beta\mathrm{sgn}(n)\sqrt{2|n|}\ )/\sqrt{\lambda}l\alpha + q_x\right). \quad \text{(E.6)}$$

We aim to apply the identity of Eq. C.1, therefore we introduce a new variable $y' = y - (k_4+k_3)/2 + il\alpha q_y/2\sqrt{\lambda}$, and we omit the prime at the same time. With these changes and some algebra we arrive at a final form of the integral with respect to y:

$$\int \mathrm{d}y e^{-y^2} H_{|n'|}(y - iP + Q_{n',n,\xi})H_{|n|}(y - iP - Q_{n',n,\xi})$$
$$= \begin{cases} 2^{|n'|}\sqrt{\pi}|n|!(-iP + Q_{n',n,\xi})^{|n'|-|n|}L_{|n|}^{|n'|-|n|}(2(Q_{n',n,\xi}^2 + P^2)) & |n'| \geq |n|, \\ 2^{|n|}\sqrt{\pi}|n'|!(-iP - Q_{n',n,\xi})^{|n|-|n'|}L_{|n'|}^{|n|-|n'|}(2(Q_{n',n,\xi}^2 + P^2)) & |n'| < |n|. \end{cases}$$

We used the shorthand notations in the above definitions

$$Q_{n',n,\xi} = \frac{q_x\sqrt{\lambda}\alpha l - \xi\beta\sqrt{2|n'|}\mathrm{sgn}(n') + \xi\beta\sqrt{2|n|}\mathrm{sgn}(n)}{2}, \quad \text{and} \quad P = \frac{\alpha l}{2\sqrt{\lambda}}q_y. \quad \text{(E.7)}$$

The form factor for $|n'| \geq |n|$ is defined as

$$F_{|n'|,|n|}^{n',n,\xi}(\mathbf{q}) = \sqrt{\frac{|n|!}{|n'|!}}\sqrt{2}^{|n'|-|n|}\,(-iP + Q_{n',n,\xi})^{|n'|-|n|}L_{|n|}^{|n'|-|n|}(2(Q_{n',n,\xi}^2 + P^2))e^{-(Q_{n',n,\xi}^2+P^2)}. \quad \text{(E.8)}$$

Similarly, for $|n| > |n'|$ the definition is

$$F_{|n'|,|n|}^{n',n,\xi}(\mathbf{q}) = \sqrt{\frac{|n'|!}{|n|!}}\sqrt{2}^{|n|-|n'|}\,(-iP - Q_{n',n,\xi})^{|n|-|n'|}\,L_{|n'|}^{|n|-|n'|}\left(2(Q_{n',n,\xi}^2 + P^2)\right)e^{-(Q_{n',n,\xi}^2+P^2)}. \quad \text{(E.9)}$$

The final result for the integral in Eq. E.5 is

$$\int \mathrm{d}\mathbf{r}[\phi^{\xi}_{n',k'}(\mathbf{r})]^{*} e^{-i\mathbf{q}\cdot\mathbf{r}} \phi^{\xi}_{n,k}(\mathbf{r}) = \\ \delta\left(k' - k + q_x\right) F^{n',n,\xi}_{|n'|,|n|}(\mathbf{q}) e^{-iq_y l\alpha\xi\beta(\mathrm{sgn}(n')\sqrt{2|n'|}+\mathrm{sgn}(n)\sqrt{2|n|})/2\sqrt{\lambda}} e^{-iq_y l^2\alpha^2(k'+k)/2}.$$

Bibliography

[1] D. S. L. Abergel and V. I. Falko, Phys. Rev. B **75**, 155430 (2007).

[2] D. S. L. Abergel, A. Russell, and V. I. Falko, Appl. Phys. Lett. **91**, 063125 (2007).

[3] P. Alemany, J. P. Pouget, and E. Canadell, Phys. Rev. B **85**, 195118 (2012).

[4] T. Ando, A. B. Fowler, and F. Stern, Rev. Mod. Phys. **54**, 437 (1982).

[5] T. Ando, J. Phys. Soc. Jpn. **75**, 074716 (2006).

[6] M. Assili, S. Haddad, and W. Kang, Phys. Rev. B **91**, 115422 (2015).

[7] S. Bae, H. K. Kim, Y. Lee, X. Xu, J.-S. Park, Y. Zheng, J. Balakrishnan, D. Im, T. Lei, Y. Il Song, Y. J. Kim, K. S. Kim, B. Özyilmaz, J.-H. Ahn, B. H. Hong, and S. Iijima, Nat. Nanotechnol. **5**, 574 (2010).

[8] W. Bao, Z. Zhao, H. Zhang, G. Liu, P. Kratz, L. Jing, J. Velasco, Jr., D. Smirnov, and C. N. Lau, Phys. Rev. Lett. **105**, 246601 (2010).

[9] Y. Barlas, R. Côté, K. Nomura, and A. H. MacDonald, Phys. Rev. Lett. **101**, 097601 (2008).

[10] Y. Barlas, R. Côté, J. Lambert, and A. H. MacDonald, Phys. Rev. Lett. **104**, 096802 (2010).

[11] D. N. Basov, M. M. Fogler, A. Lanzara, F. Wang, and Y. Zhang, Rev. Mod. Phys. **86**, 959 (2014).

[12] C. Bena and G. Montambaux, New J. Phys. **11**, 095003 (2009).

[13] K. Bender, I. Hennig, D. Schweitzer, K. Dietz, H. Endres, and H. J. Keller, Mol. Cryst. Liq. Cryst. **108**, 359 (1984).

[14] J. D. Bernal, Proc. Roy. Soc. A **106**, 749 (1924).

[15] I. B. Bernstein, Phys. Rev. **109**, 10 (1958).

[16] V. E. Bisti and N. N. Kirova, Phys. Rev. B **84**, 155434 (2011).

[17] V. E. Bisti, Pis'ma Zh. Eksp. Teor. Fiz. **98**, 57 (2013) [JETP Lett. **98**, 52 (2013)].

[18] P. Blake, E. W. Hill, A. H. Castro Neto, K. S. Novoselov, D. Jiang, R. Yang, T. J. Booth, and A. K. Geim, Appl. Phys. Lett. **91**, 063124 (2007).

[19] D. Bohm and D. Pines, Phys. Rev. **82**, 625 (1951).

[20] D. Bohm and D. Pines, Phys. Rev. **92**, 609 (1953).

[21] L. G. Booshehri, C. H. Mielke, D. G. Rickel, S. A. Crooker, Q. Zhang, L. Ren, E. H. Hároz, A. Rustagi, C. J. Stanton, Z. Jin, Z. Sun, Z. Yan, J. M. Tour, and J. Kono, Phys. Rev. B **85**, 205407 (2012).

[22] A. Bostwick, T. Ohta, T. Seyller, K. Horn, and E. Rotenberg, Nat. Phys. **3**, 36 (2007).

[23] Yu. A. Bychkov, S. V. Iordanskii, and G. M. Eliashberg, Pis'ma Zh. Eksp. Teor. Fiz. **33**, 152 (1981) [Sov. Phys. JETP Lett. **33**, 143 (1981)].

[24] Yu. A. Bychkov and E. I. Rashba, Zh. Eksp. Teor. Fiz. **85**, 1826 (1983) [Sov. Phys. JETP **58**, 1062 (1983)].

[25] Yu. A. Bychkov and G. Martinez, Phys. Rev. B **77**, 125417 (2008).

[26] E. V. Castro, K. S. Novoselov, S. V. Morozov, N. M. R. Peres, J. M. B. Lopes dos Santos, J. Nilsson, F. Guinea, A. K. Geim, and A. H. Castro Neto, Phys. Rev. Lett. **99**, 216802 (2007).

[27] A. H. Castro Neto, F. Guinea, N. M. R. Peres, K. S. Novoselov, and A. K. Geim, Rev. Mod. Phys. **81**, 109 (2009).

[28] K. W. Chiu and J. J. Quinn, Phys. Rev. B **9**, 4724 (1974).

[29] D. B. Chklovskii, B. I. Shklovskii, and L. I. Glazman, Phys. Rev. B **46**, 4026 (1992).

[30] T. Choji, A. Kobayashi, and Y. Suzumura, J. Phys. Soc. Jpn. **80**, 074712 (2011).

[31] R. Côté, J. Lambert, Y. Barlas, and A. H. MacDonald, Phys. Rev. B **82**, 035445 (2010).

[32] J. Cserti and G. Dávid, Phys. Rev. B **74**, 172305 (2006).

[33] J. Cserti, A. Csordás, and G. Dávid, Phys. Rev. Lett. **99**, 066802 (2007).

[34] H. P. Dahal, Y. N. Joglekar, K. S. Bedell, and A. V. Balatsky, Phys. Rev. B **74**, 233405 (2006).

[35] S. Das Sarma, S. Adam, E. H. Hwang, and E. Rossi, Rev. Mod. Phys. **83**, 407 (2011).

[36] G. Dávid and J. Cserti, Phys. Rev. B **81**, 121417 (2010).

[37] R. S. Deacon, K.-C. Chuang, R. J. Nicholas, K. S. Novoselov, and A. K. Geim, Phys. Rev. B **76**, 081406(R) (2007).

[38] H. Duan, N. Yan, R. Yu, C.-R. Chang, G. Zhou, H.-S. Hu, H. Rong, Z. Niu, J. Mao, H. Asakura, T. Tanaka, P. J. Dyson, J. Li, and Y. Li, Nat. Commun. **5**, 3093 (2014).

[39] H. J. van Elferen, A. Veligura, E. V. Kurganova, U. Zeitler, J. C. Maan, N. Tombros, I. J. Vera-Marun, and B. J. van Wees, Phys. Rev. B **85**, 115408 (2012).

[40] M. A. Eriksson, A. Pinczuk, B. S. Dennis, S. H. Simon, L. N. Pfeiffer, and K. W. West, Phys. Rev. Lett. **82**, 2163 (1999).

[41] V. I. Fal'ko, Philos. Trans. R. Soc. A **366**, 205 (2008).

[42] G. Fasol, N. Mestres, H. P. Hughes, A. Fischer, and K. Ploog, Phys. Rev. Lett. **56**, 2517 (1986).

[43] C. Faugeras, M. Amado, P. Kossacki, M. Orlita, M. Kühne, A. A. L. Nicolet, Y. I. Latyshev, and M. Potemski, Phys. Rev. Lett. **107**, 036807 (2011).

[44] Z. Fei, A. S. Rodin, G. O. Andreev, W. Bao, A. S. McLeod, M. Wagner, L. M. Zhang, Z. Zhao, M. Thiemens, G. Dominguez, M. M. Fogler, A. H. Castro Neto, C. N. Lau, F. Keilmann, and D. N. Basov, Nature **487**, 82 (2012).

[45] B. E. Feldman, J. Martin, and A. Yacoby, Nat. Phys. **5**, 889 (2009).

[46] H. A. Fertig, L. Brey, R. Côté, A. H. MacDonald, A. Karlhede, and S. L. Sondhi, Phys. Rev. B **55**, 10671 (1997).

[47] A. L. Fetter and J. D. Walecka, *Quantum theory of many-particle systems* (McGraw-Hill Book Company, New York, 1971).

[48] R. de Gail, M. O. Goerbig, and G. Montambaux, Phys. Rev. B **86**, 045407 (2012).

[49] S. Gangadharaiah, A. M. Farid, and E. G. Mishchenko, Phys. Rev. Lett. **100**, 166802 (2008).

[50] A. K. Geim and K. S. Novoselov, Nat. Mater. **6**, 183 (2007).

[51] S. M. Girvin, *The Quantum Hall Effect: Novel Excitations and Broken Symmetries*, in *Topological Aspects of Low Dimensional Systems*, edited by A. Comtet, T. Jolicoeur, S. Ouvry, and F. David (Springer-Verlag, Berlin and Les Editions de Physique, Les Ulis, 2000).

[52] G. F. Giuliani and G. Vignale, *Quantum Theory of the Electron Liquid* (Cambridge University Press, Cambridge, 2005).

[53] M. O. Goerbig, J.-N. Fuchs, G. Montambaux, and F. Piéchon, Phys. Rev. B **78**, 045415 (2008).

[54] M. O. Goerbig, Rev. Mod. Phys. **83**, 1193 (2011).

[55] E. V. Gorbar, V. P. Gusynin, and V. A. Miransky, Pis'ma Zh. Eksp. Teor. Fiz. **91**, 334 (2010) [JETP Lett. **91**, 314 (2010)].

[56] E. V. Gorbar, V. P. Gusynin, and V. A. Miransky, Phys. Rev. B **81**, 155451 (2010).

[57] E. V. Gorbar, V. P. Gusynin, V. A. Miransky, and I. A. Shovkovy, Phys. Rev. B **85**, 235460 (2012).

[58] I. S. Gradshteyn and I. M. Ryzhik, *Table of Integrals, Series, and Products*, edited by A. Jeffrey and D. Zwillinger (Elsevier/Academic Press, Amsterdam, 2007).

[59] W. Greiner, *Relativistic quantum mechanics: wave equations* (Springer, Berlin, 2000).

[60] F. Guinea, A. H. Castro Neto, and N. M. R. Peres, Phys. Rev. B **73**, 245426 (2006).

[61] M. Z. Hasan and C. L. Kane, Rev. Mod. Phys. **82**, 3045 (2010).

[62] E. A. Henriksen, Z. Jiang, L.-C. Tung, M. E. Schwartz, M. Takita, Y.-J. Wang, P. Kim, and H. L. Stormer, Phys. Rev. Lett. **100**, 087403 (2008).

[63] E. A. Henriksen, P. Cadden-Zimansky, Z. Jiang, Z. Q. Li, L.-C. Tung, M. E. Schwartz, M. Takita, Y.-J. Wang, P. Kim, and H. L. Stormer, Phys. Rev. Lett. **104**, 067404 (2010).

[64] E. A. Henriksen and J. P. Eisenstein, Phys. Rev. B **82**, 041412(R) (2010).

[65] T. Himura, T. Morinari, and T. Tohyama, J. Phys.: Condens. Matter **23**, 464202 (2011).

[66] E. H. Hwang and S. Das Sarma, Phys. Rev. B **75**, 205418 (2007).

[67] S. Ishibashi, T. Tamura, M. Kohyama, and K. Terakura, J. Phys. Soc. Jpn. **75**, 015005 (2006).

[68] A. Iyengar, J. Wang, H. A. Fertig, and L. Brey, Phys. Rev. B **75**, 125430 (2007).

[69] J. K. Jain and P. B. Allen, Phys. Rev. Lett. **54**, 2437 (1985).

[70] Z. Jiang, E. A. Henriksen, L. C. Tung, Y.-J. Wang, M. E. Schwartz, M. Y. Han, P. Kim, and H. L. Stormer, Phys. Rev. Lett. **98**, 197403 (2007).

[71] K. Kajita, T. Ojiro, H. Fujii, Y. Nishio, H. Kobayashi, A. Kobayashi, and R. Kato, J. Phys. Soc. Jpn. **61**, 23 (1992).

[72] C. Kallin and B. I. Halperin, Phys. Rev. B **30**, 5655 (1984).

[73] M. Kang, A. Pinczuk, B. S. Dennis, L. N. Pfeiffer, and K. W. West, Phys. Rev. Lett. **86**, 2637 (2001).

[74] S. Katayama, A. Kobayashi, and Y. Suzumura, J. Phys. Soc. Jpn. **75**, 054705 (2006).

[75] S. Katayama, A. Kobayashi, and Y. Suzumura, J. Phys.: Conf. Series **132**, 012003 (2008).

[76] S. Katayama, A. Kobayashi, and Y. Suzumura, Eur. Phys. J. B **67**, 139 (2009).

[77] M. I. Katsnelson, Eur. Phys. J. B **51**, 157 (2006).

[78] M. I. Katsnelson, K. S. Novoselov, and A. K. Geim, Nat. Phys. **2**, 620 (2006).

[79] M. Kharitonov, Phys. Rev. Lett. **109**, 046803 (2012).

[80] S. Kim, K. Lee, and E. Tutuc, Phys. Rev. Lett. **107**, 016803 (2011).

[81] H. Kino and T. Miyazaki, J. Phys. Soc. Jpn. **75**, 034704 (2006).

[82] A. Kobayashi, S. Katayama, Y. Suzumura, and H. Fukuyama, J. Phys. Soc. Jpn. **76**, 034711 (2007).

[83] W. Kohn, Phys. Rev. **123**, 1242 (1961).

[84] R. Kondo, S. Kagoshima, N. Tajima, and R. Kato, J. Phys. Soc. Jpn. **78**, 114714 (2009).

[85] A. Kormányos, V. Zólyomi, N. D. Drummond, P. Rakyta, G. Burkard, and V. I. Falko, Phys. Rev. B **88**, 045416 (2013); A. Kormányos, P. Rakyta, and G. Burkard, New J. Phys. **17**, 103006 (2015).

[86] V. N. Kotov, B. Uchoa, V. M. Pereira, F. Guinea, and A. H. Castro Neto, Rev. Mod. Phys. **84**, 1067 (2012).

[87] E. V. Kurganova, A. J. M. Giesbers, R. V. Gorbachev, A. K. Geim, K. S. Novoselov, J. C. Maan, and U. Zeitler, Solid State Commun. **150**, 2209 (2010).

[88] J. Lambert and R. Côté, Phys. Rev. B **87**, 115415 (2013).

[89] I. V. Lerner and Yu. E. Lozovik, Zh. Eksp. Teor. Fiz. **78**, 1167 (1978) [Sov. Phys. JETP **51**, 588 (1980)].

[90] G. Li, A. Luican, and E. Y. Andrei, Phys. Rev. Lett. **102**, 176804 (2009).

[91] Z. Q. Li, E. A. Henriksen, Z. Jiang, Z. Hao, M. C. Martin, P. Kim, H. L. Stormer, and D. N. Basov, Nat. Phys. **4**, 532 (2008).

[92] Z. Q. Li, E. A. Henriksen, Z. Jiang, Z. Hao, M. C. Martin, P. Kim, H. L. Stormer, and D. N. Basov, Phys. Rev. Lett. **102**, 037403 (2009).

[93] K. Lier and R. R. Gerhardts, Phys. Rev. B **50**, 7757 (1994).

[94] M. Lotya, P. J. King, U. Khan, S. De, and J. N. Coleman, ACS Nano **4**, 3155 (2010).

[95] Yu. E. Lozovik and A. A. Sokolik, Nanoscale Res. Lett. **7**, 134 (2012).

[96] V. Lukose, R. Shankar, and G. Baskaran, Phys. Rev. Lett. **98**, 116802 (2007).

[97] A. H. MacDonald, J. Phys. C: Solid State Phys. **18**, 1003 (1985).

[98] K. F. Mak, M. Y. Sfeir, Y. Wu, C. H. Lui, J. A. Misewich, and T. F. Heinz, Phys. Rev. Lett. **101**, 196405 (2008).

[99] K. F. Mak, C. H. Lui, J. Shan, and T. F. Heinz, Phys. Rev. Lett. **102**, 256405 (2009).

[100] J. Martin, B. E. Feldman, R. T. Weitz, M. T. Allen, and A. Yacoby, Phys. Rev. Lett. **105**, 256806 (2010).

[101] E. McCann, Phys. Rev B **74**, 161403 (2006).

[102] E. McCann and V. I. Falko, Phys. Rev. Lett. **96**, 086805 (2006).

[103] J. W. McClure, Phys. Rev. **104**, 666 (1956).

[104] J. W. McClure, Phys. Rev. **108**, 612 (1957).

[105] M. Mecklenburg and B. C. Regan, Phys. Rev. Lett. **106**, 116803 (2011); P. Kosiński, P. Maślanka, J. Sławińska, and I. Zasada, Prog. Theor. Phys. **128**, 727 (2012).

[106] P. Miró, M. Audiffred, and T. Heine, Chem. Soc. Rev. **43**, 6537 (2014).

[107] T. Misumi and K. Shizuya, Phys. Rev. B **77**, 195423 (2008).

[108] K. Miyagawa, M. Hirayama, M. Tamura, and K. Kanoda, J. Phys. Soc. Jpn. **79**, 063703 (2010).

[109] G. Montambaux, F. Piéchon, J.-N. Fuchs, and M. O. Goerbig, Eur. Phys. J. B **72**, 509 (2009).

[110] G. Montambaux, F. Piéchon, J.-N. Fuchs, and M. O. Goerbig, Phys. Rev. B **80**, 153412 (2009).

[111] M. Monteverde, M. O. Goerbig, P. Auban-Senzier, F. Navarin, H. Henck, C. R. Pasquier, C. Mézière, and P. Batail, Phys. Rev. B **87**, 245110 (2013).

[112] T. Mori, A. Kobayashi, Y. Sasaki, H. Kobayashi, G. Saito, and H. Inokuchi, Chem. Lett. **13**, 957 (1984).

[113] T. Mori, J. Phys. Soc. Jpn. **79**, 014703 (2010).

[114] T. Mori, J. Phys. Soc. Jpn. **82**, 034712 (2013).

[115] T. Morinari, T. Himura, and T. Tohyama, J. Phys. Soc. Jpn. **78**, 023704 (2009).

[116] M. Mucha-Kruczyński, E. McCann, and V. I. Fal'ko, Solid State Commun. **149**, 1111 (2009).

[117] M. Mucha-Kruczyński, O. Kashuba, and V. I. Fal'ko, Phys. Rev. B **82**, 045405 (2010).

[118] K. Murata, S. Kagoshima, S. Yasuzuka, H. Yoshino, and R. Kondo, J. Phys. Soc. Jpn. **75**, 051015 (2006).

[119] R. R. Nair, P. Blake, A. N. Grigorenko, K. S. Novoselov, T. J. Booth, T. Stauber, N. M. R. Peres, and A. K. Geim, Science **320**, 1308 (2008).

[120] T. Nishine, A. Kobayashi, and Y. Suzumura, J. Phys. Soc. Jpn. **79**, 114715 (2010).

[121] T. Nishine, A. Kobayashi, and Y. Suzumura, J. Phys. Soc. Jpn. **80**, 114713 (2011).

[122] K.S. Novoselov, A. K. Geim, S. V. Morozov, D. Jiang, M. I. Katsnelson, I. V. Grigorieva, S. V. Dubonos, and A. A. Firsov, Nature **438**, 197 (2005).

[123] K. S. Novoselov, E. McCann, S. V. Morozov, V. I. Falko, M. I. Katsnelson, U. Zeitler, D. Jiang, F. Schedin, and A. K. Geim, Nat. Phys. **2**, 177 (2006).

[124] T. Ohta, A. Bostwick, T. Seyller, K. Horn, and E. Rotenberg, Science **313**, 951 (2006).

[125] D. Olego, A. Pinczuk, A. C. Gossard, and W. Wiegmann, Phys. Rev. B **26**, 7867 (1982).

[126] T. Osada, J. Phys. Soc. Jpn. **77**, 084711 (2008).

[127] T. Osada, J. Phys. Soc. Jpn. **80**, 033708 (2011).

[128] S. Park and R. S. Ruoff, Nat. Nanotechnol. **4**, 217 (2009).

[129] J. M. Pereira, Jr., F. M. Peeters, and P. Vasilopoulos, Phys. Rev. B **76**, 115419 (2007).

[130] N. M. R. Peres and E. V. Castro, J. Phys.: Condens. Matter **19**, 406231 (2007).

[131] N. M. R. Peres, Rev. Mod. Phys. **82**, 2673 (2010).

[132] A. Pinczuk, S. Schmitt-Rink, G. Danan, J. P. Valladares, L. N. Pfeiffer, and K. W. West, Phys. Rev. Lett. **63**, 1633 (1989).

[133] A. Pinczuk, B. S. Dennis, L. N. Pfeiffer, and K. West, Phys. Rev. Lett. **70**, 3983 (1993).

[134] A. Pinczuk, B. S. Dennis, L. N. Pfeiffer, and K. W. West, Semicond. Sci. Technol. **9**, 1865 (1994).

[135] D. Pines and D. Bohm, Phys. Rev. **85**, 338 (1952).

[136] J. M. Poumirol, W. Yu, X. Chen, C. Berger, W. A. de Heer, M. L. Smith, T. Ohta, W. Pan, M. O. Goerbig, D. Smirnov, and Z. Jiang, Phys. Rev. Lett. **110**, 246803 (2013).

[137] I. Proskurin, M. Ogata, and Y. Suzumura, Phys. Rev. B **91**, 195413 (2015).

[138] P. Rakyta, M. Vigh, A. Csordás, and J. Cserti, Phys. Rev. B **91**, 125412 (2015).

[139] T. D. Rhone, D. Majumder, B. S. Dennis, C. Hirjibehedin, I. Dujovne, J. G. Groshaus, Y. Gallais, J. K. Jain, S. S. Mandal, Aron Pinczuk, L. Pfeiffer, and K. West, Phys. Rev. Lett. **106**, 096803 (2011).

[140] R. Roldán, J.-N. Fuchs, and M. O. Goerbig, Phys. Rev. B **80**, 085408 (2009); R. Roldán, M. O. Goerbig and J.-N. Fuchs, Semicond. Sci. Technol. **25**, 034005 (2010).

[141] R. Roldán, J.-N. Fuchs, and M. O. Goerbig, Phys. Rev. B **82**, 205418 (2010).

[142] R. Roldán, M. O. Goerbig, and J.-N. Fuchs, Phys. Rev. B **83**, 205406 (2011).

[143] M. L. Sadowski, G. Martinez, M. Potemski, C. Berger, and W. A. de Heer, Phys. Rev. Lett. **97**, 266405 (2006).

[144] M. Sato, K. Miura, S. Endo, S. Sugawara, N. Tajuma, K. Murata, Y. Nishio, and K. Kajita J. Phys. Soc. Jpn **80**, 023706 (2011).

[145] G. W. Semenoff, Phys. Rev. Lett. **53**, 2449 (1984).

[146] K. Shizuya, Phys. Rev. B **81**, 075407 (2010).

[147] K. Shizuya, Phys. Rev. B **86**, 045431 (2012).

[148] K. Shizuya, Phys. Rev. B **87**, 085413 (2013).

[149] K. W. K. Shung, Phys. Rev. B **34**, 979 (1986).

[150] J. C. Slonczewski and P. R. Weiss, Phys. Rev. **109**, 272 (1958).

[151] J. Sólyom, *Fundamentals of the Physics of Solids, Volume I-III* (Springer, Berlin, 2010).

[152] S. L. Sondhi, A. Karlhede, S. A. Kivelson, and E. H. Rezayi, Phys. Rev. B **47**, 16419 (1993).

[153] R. Sooryakumar, A. Pinczuk, A. Gossard, and W. Wiegmann, Phys. Rev. B **31**, 2578 (1985).

[154] F. Stern, Phys. Rev. Lett. **18**, 546 (1967).

[155] C.-Y. Su, A.-Y. Lu, Y. Xu, F.-R. Chen, A. N. Khlobystov, and L.-J. Li, ACS Nano **5**, 2332 (2011).

[156] S. Sugawara, M. Tamura, N. Tajima, R. Kato, M. Sato, Y. Nishio, and K. Kajita, J. Phys. Soc. Jpn. **79**, 113704 (2010).

[157] N. Tajima, M. Tamura, Y. Nishio, K. Kajita, and Y. Iye, J. Phys. Soc. Jpn. **69**, 543 (2000).

[158] N. Tajima, A. Ebina-Tajima, M. Tamura, Y. Nishio, and K. Kajita, J. Phys. Soc. Jpn. **71**, 1832 (2002).

[159] N. Tajima, A. Tajima, M. Tamura, R. Kato, Y. Nishio, and K. Kajita, J. Phys. IV (Paris) **114**, 263 (2004).

[160] N. Tajima, S. Sugawara, M. Tamura, Y. Nishio, and K. Kajita, J. Phys. Soc. Jpn. **75**, 051010 (2006).

[161] N. Tajima and K. Kajita, Sci. Technol. Adv. Mater. **10**, 024308 (2009).

[162] N. Tajima, S. Sugawara, R. Kato, Y. Nishio, and K. Kajita, Phys. Rev. Lett. **102**, 176403 (2009).

[163] N. Tajima, T. Yamauchi, T. Yamaguchi, M. Suda, Y. Kawasugi, H. M. Yamamoto, R. Kato, Y. Nishio, and K. Kajita, Phys. Rev. B **88**, 075315 (2013).

[164] B. Tanatar and D. M. Ceperley, Phys. Rev. B **39**, 5005 (1989).

[165] R. Y. Tay, M. H. Griep, G. Mallick, S. H. Tsang, R. S. Singh, T. Tumlin, E. H. Tong Teo, and S. P. Karna, Nano Lett. **14**, 839 (2014).

[166] C. Tőke and V. I. Fal'ko, Phys. Rev. B **83**, 115455 (2011).

[167] C. Tőke, Phys. Rev. B **88**, 241411(R) (2013).

[168] P. R. Wallace, Phys. Rev. **71**, 622 (1947).

[169] D. Wang and G. Jin, Europhys. Lett. **92**, 57008 (2010).

[170] J. Wang, S. Deng, Z. Liu, and Z. Liu, Nat. Sci. Rev. **2**, 22 (2015).

[171] Q. H. Wang, K. Kalantar-Zadeh, A. Kis, J. N. Coleman, and M. S. Strano, Nat. Nanotechnol. **7**, 699 (2012).

[172] H. Wei, S.-P. Chao, and V. Aji, Phys. Rev. B **86**, 041403(R) (2012).

[173] R. T. Weitz, M. T. Allen, B. E. Feldman, J. Martin, and A. Yacoby, Science **330**, 812 (2010).

[174] B. Wunsch, T. Stauber, F. Sols, and F. Guinea, New J. Phys. **8**, 318 (2006).

[175] J. Yan, S. Goler, T. D. Rhone, M. Han, R. He, P. Kim, V. Pellegrini, and A. Pinczuk, Phys. Rev. Lett. **105**, 227401 (2010).

[176] K. Yang, S. Das Sarma, and A. H. MacDonald, Phys. Rev. B **74**, 075423 (2006).

[177] X. Yin, X. Liu, Y.-T. Pan, K. A. Walsh, and H. Yang, Nano Lett. **14**, 7188 (2014).

[178] A. F. Young and P. Kim, Nat. Phys. **5**, 222 (2009).

[179] J. Xue, arXiv:1309.6714 (2013).

[180] N. Zettili, *Quantum Mechanics: Concepts and Applications* (John Wiley & Sons, Chichester, 2009).

[181] L. M. Zhang, Z. Q. Li, D. N. Basov, M. M. Fogler, Z. Hao, and M. C. Martin, Phys. Rev. B **78**, 235408 (2008).

[182] L. M. Zhang, M. M. Fogler, and D. P. Arovas, Phys. Rev. B **84**, 075451 (2011).

[183] Y. Zhang, Y.-W. Tan, H. L. Stormer, and P. Kim, Nature **438**, 201 (2005).

[184] Y. Zhang, T.-T. Tang, C. Girit, Z. Hao, M. C. Martin, A. Zettl, M. F. Crommie, Y. R. Shen, and F. Wang, Nature, **459**, 820 (2009).

[185] Y. Zhao, P. Cadden-Zimansky, Z. Jiang, and P. Kim, Phys. Rev. Lett. **104**, 066801 (2010).

[186] K. Zou, X. Hong, J. Zhu, Phys. Rev. B **84**, 085408 (2011).